

AD 607742

ASD-TDR-62-719,
PART II

**THERMAL RADIATION CHARACTERISTICS OF TRANSPARENT
SEMI-TRANSPARENT AND TRANSLUCENT MATERIALS
UNDER NON-ISOTHERMAL CONDITIONS**

TECHNICAL DOCUMENTARY REPORT NO. ASD-TDR-62-719 Part II

June 1964

COPY	OF	Sign
HARD COPY	\$.50	
MICROFICHE	\$.50	

Air Force Materials Laboratory
Research and Technology Division
Air Force Systems Command
Wright-Patterson Air Force Base, Ohio

Project No. 7360, Task No. 736001

(Prepared under Contract No. AF 33(657)-11200
Lexington Laboratories, Inc., Cambridge Massachusetts;
Robert C. Folweiler and William J. Mallio, authors)

NOTICES

When Government drawings, specifications, or other data are used for any purpose other than in connection with a definitely related Government procurement operation, the United States Government thereby incurs no responsibility nor any obligation whatsoever; and the fact that the Government may have formulated, furnished, or in any way supplied the said drawings, specifications, or other data, is not to be regarded by implication or otherwise as in any manner licensing the holder or any other person or corporation, or conveying any rights or permission to manufacture, use or sell any patented invention that may in any way be related thereto.

Qualified requesters may obtain copies of this report from the Defense Documentation Center (DDC), (formerly ASTIA), Cameron Station, Bldg. 5, 5010 Duke Street, Alexandria, Virginia, 22314.

This report has been released to the Office of Technical Services, U. S. Department of Commerce, Washington 25, D.C., for sale to the general public.

Copies of this report should not be returned to the Research and Technology Division, Wright-Patterson Air Force Base, Ohio, unless return is required by security considerations, contractual obligations, or notice on a specific document.

THERMAL RADIATION CHARACTERISTICS OF TRANSPARENT SEMI-
TRANSPARENT AND TRANSLUCENT MATERIALS UNDER NON-
ISOTHERMAL CONDITIONS



A GOVERNMENT RESEARCH REPORT

U.S. DEPARTMENT OF COMMERCE

OFFICE OF TECHNICAL SERVICES

distributes this and thousands of similar reports in the interest of science, industry, and the public—for which research and new products mean better health, better living, and a stronger economy.

HOW TO GET OTHER REPORTS

The Office of Technical Services is the Nation's clearinghouse for reports of research supported by the Army, Navy, Air Force, Atomic Energy Commission, and other Government agencies.

Abstracts of new reports available are published twice a month in U. S. GOVERNMENT RESEARCH REPORTS (\$15 a year domestic).

Selected Reports of particular interest to small business are described monthly in TECHNICAL REPORTS NEWSLETTER (\$1 a year domestic).

Translations of foreign technical material are also available from the Office of Technical Services and other sources. These are listed or abstracted semi-monthly in TECHNICAL TRANSLATIONS (\$12 a year domestic).

The above periodicals may be ordered from Superintendent of Documents, U. S. Government Printing Office, Washington, D. C., 20402, or through a U. S. Department of Commerce Field Office.

Inquiries about the availability of reports and translations on any particular subject may be directed to Office of Technical Services, U. S. Department of Commerce, Washington, D.C., 20230, or to any Commerce field office.

Reports and translations are published by the Office of Technical Services for use by the public. Thus, you may use the know-how or reprint the information therein except that where patent questions appear to be involved the usual preliminary search is advised, and where copyrighted material is used permission should be obtained for its further publication.

These documents are reprinted by OTS from the best available copy.

**CLEARINGHOUSE FOR FEDERAL SCIENTIFIC AND TECHNICAL INFORMATION CFSTI
DOCUMENT MANAGEMENT BRANCH 410.11**

LIMITATIONS IN REPRODUCTION QUALITY

ACCESSION # **AD 607742**

- ☒ 1. WE REGRET THAT LEGIBILITY OF THIS DOCUMENT IS IN PART UNSATISFACTORY. REPRODUCTION HAS BEEN MADE FROM BEST AVAILABLE COPY.
- ☐ 2. A PORTION OF THE ORIGINAL DOCUMENT CONTAINS FINE DETAIL WHICH MAY MAKE READING OF PHOTOCOPY DIFFICULT.
- ☐ 3. THE ORIGINAL DOCUMENT CONTAINS COLOR, BUT DISTRIBUTION COPIES ARE AVAILABLE IN BLACK-AND-WHITE REPRODUCTION ONLY.
- ☐ 4. THE INITIAL DISTRIBUTION COPIES CONTAIN COLOR WHICH WILL BE SHOWN IN BLACK-AND-WHITE WHEN IT IS NECESSARY TO REPRINT.
- ☐ 5. LIMITED SUPPLY ON HAND: WHEN EXHAUSTED, DOCUMENT WILL BE AVAILABLE IN MICROFICHE ONLY.
- ☐ 6. LIMITED SUPPLY ON HAND: WHEN EXHAUSTED DOCUMENT WILL NOT BE AVAILABLE.
- ☐ 7. DOCUMENT IS AVAILABLE IN MICROFICHE ONLY.
- ☐ 8. DOCUMENT AVAILABLE ON LOAN FROM CFSTI (TT DOCUMENTS ONLY).
- ☐ 9.

PROCESSOR: **9/23**

FOREWORD

This report was prepared by Lexington Laboratories, Inc., Cambridge, Massachusetts under USAF Contract AF33(657)-11280. This contract was initiated under Project No. 7360, "The Chemistry and Physics of Materials", Task No. 736001, "Thermodynamics and Heat Transfer". The work was administered under the direction of the Air Force Materials Laboratory, Research and Technology Division, Wright-Patterson Air Force Base, Ohio, with Mr. R. J. Prezecki acting as project engineer.

Robert C. Folweiler is Project Engineer on the contract for Lexington Laboratories, Inc. Contributors to the project include W. B. Fraser, D. A. Hill, W. D. Kingery, W. J. Mallio, and D. W. Moore.

ABSTRACT

Thermal radiation from refractory oxides is a volume, rather than a surface phenomenon in the wavelength range 0.5-6 microns. Emissivity values have been calculated for specially prepared Al_2O_3 , MgO , SiO_2 and SrTiO_3 samples from appropriate reflectivities, absorption coefficients and scattering coefficients derived from material characteristics (index of refraction, single crystal transmissivity, pore size and concentration).

Experimental measurements of emissivity for these samples have been made at temperature up to 1200°C and at wavelengths from one to fifteen microns. Calculated and measured values are in good agreement for Al_2O_3 and SiO_2 . Absorption coefficients of the MgO and SrTiO_3 samples were greater than the single crystal values, leading to higher measured (than calculated) emissivities. Samples of commercial alumina had higher emissivities than the specially prepared high purity samples.

The Hamaker equations for non-isothermal emissivity, which linearize the temperature gradient, have been compared with the exact solution by numerical integration. Results are in good agreement for all cases of practical interest for application to ceramic oxides. Solutions to the Hamaker equations have been derived for new boundary conditions.

Evaluation of the rotating blackbody slot system indicates it gives results in good agreement with an external blackbody. An apparatus for measuring the effective emissivity of a non-isothermal sample has been constructed and tested.

This technical documentary report has been reviewed and
is approved.



ROBERT E. BROCKLEHURST
Assistant Chief
Materials Physics Division
AF Materials Laboratory

TABLE OF CONTENTS

1.0	INTRODUCTION	1
2.0	CALCULATION OF ISOTHERMAL EMISSIVITY FROM MATERIAL CHARACTERIZATION	3
2.1	Reflectivity	4
2.2	The Absorption Coefficient, a	5
2.3	The Scattering Coefficient, s	14
2.4	The Material Constant, β_0	18
2.5	Calculation of Emissivity in the Wavelength Range 0.5 - 8 Microns	18
2.6	Calculation of Emissivity in the Wavelength Range 8 - 15 Microns	18
2.7	Normal vs. Hemispherical Emissivity	20
2.8	Reflectivity for Parallel Radiant Flux at Normal Incidence	29
3.0	THE HAMAKER APPROXIMATION FOR CONDUCTIVE HEAT FLOW	32
3.1	Direct Numerical Integration	33
3.2	The Hamaker Approximation	35
3.3	Numerical Evaluations of the Hamaker Solutions	35
3.4	Comparison of Exact and Hamaker Solutions	36
4.0	EXTENSION OF THE HAMAKER EQUATIONS	43
5.0	SAMPLE PREPARATION AND CHARACTERIZATION	47
5.1	Al_2O_3	48

TABLE OF CONTENTS (CONT'D.)

5.1.1	Preparation	48
5.1.2	Characterization	48
5.2	MgO	49
5.2.1	Preparation	49
5.2.2	Characterization	49
5.3	SrTiO ₃	50
5.3.1	Preparation	50
5.3.2	Characterization	50
5.4	SiO ₂	50
5.4.1	Preparation	50
5.4.2	Characterization	51
5.5	CaF ₂	51
5.5.1	Preparation	51
6.0	SINGLE CRYSTAL ABSORPTIVITY	58
6.1	Experimental Technique	58
6.2	Samples	58
6.3	Results	59
7.0	ISOTHERMAL EMISSIVITY AND CALIBRATION MEASUREMENTS	65
7.1	Isothermal Emissivity	65
7.1.1	Measurements	65
7.1.2	Results of isothermal measurements	65

TABLE OF CONTENTS (CONT'D.)

7.2	Blackbody Calibration	65
7.2.1	Apparatus	66
7.2.2	Calculations	66
7.2.3	Results and discussion	68
8.0	COMPARISON OF MEASURED AND CALCULATED EMISSIVITIES	110
8.1	Aluminum Oxide	110
8.2	Silica Glass	110
8.3	Magnesia	111
8.4	Strontium Titanate	111
8.5	Commercial Alumina	111
9.0	APPARATUS AND METHOD FOR MEASURING NON-ISOTHERMAL EMISSIVITY	113
9.1	Production of Radial Thermal Gradient	115
9.2	Internal Heating Element	115
9.3	Measurement of the Temperature Gradient	116
9.4	Operation	116
9.5	Non-Isothermal Measurements	116
10.0	DISCUSSION	119
11.0	REFERENCES	125
APPENDIXES		
I	Values for Indices of Refraction Used in Emissivity Calculations	126
II	Sample Calculations of Emissivity	127

ILLUSTRATIONS

Figure 2.1	Diagram of Geometry of Radiation in a Thin Slice of Absorbing Material.	9
Figure 2.2	Relative Fraction of Back Scattering for Pores of Large Size in a Solid Matrix.	17
Figure 2.3	Values of the Scattering Factor K for Various Values of the Relative Index, m, When $m < 1$.	19
Figure 2.4	Diagram of Geometry of Diffuse Radiation Leaving a Material of Index n (where $n > 1$).	22
Figure 2.5	Distribution of Intensity of Reflected and Transmitted Energy of Isotropic Radiation Incident on an Al_2O_3 - Air Interface.	25
Figure 3.1	Heat Flow by Combined Radiation and Conduction.	34
Figure 3.2	Computer Results (Solid Lines) and Hand Calculated Results (Points) for the Exact Solution of Radiant Energy Heat Transfer.	37
Figure 3.3	Typical Results between Exact and Hamaker Equations for Small Values of a and s. $I_o = 0$; $J_o = J$; $k = 0.01$; $T_o = 1000$; $(\frac{dT}{dx})_o = 10$; $a = 0.1$; $s = 0.1$; $n^2 = 3$.	38
Figure 3.4	Typical Results of Comparison between Exact and Hamaker Equations in Large Values of a, s and $k(\frac{dT}{dx})_o$. $I_o = 0$; $J_o = 50$; $k = .01$; $T_o = 2000$; $(\frac{dT}{dx})_o = 1000$; $a = 1$; $s = 100$; $n^2 = 3$.	39

ILLUSTRATIONS (CONT'D.)

Figure 5.1	Al-1 532X. Point Count Density = 88.1% of Theoretical Density.	52
Figure 5.2	Al-2 532X. Point Count Density = 77.4% of Theoretical Density.	52
Figure 5.3	Al-3 532X. Point Count Density = 96.4% of Theoretical Density.	53
Figure 5.4	Al-4 532X. Point Count Density = 85.5% of Theoretical Density.	53
Figure 5.5	Al-6 532X. Point Count Density = 77.0% of Theoretical Density.	54
Figure 5.6	Mg-3 532X. Point Count Density = 88.0% of Theoretical Density.	54
Figure 5.7	Mg-5 532X. Point Count Density = 90.0% of Theoretical Density.	55
Figure 5.8	Sr-1 1064X. Point Count Density = 92.9% of Theoretical Density.	55
Figure 5.9	Sr-2 1064X. Immersion Density = 63% of Theoretical Density	56
Figure 5.10	FS-3 532X. Point Count Density = 65.9% of Theoretical Density.	56
Figure 5.11	FS-5 532X. Point Count Density = 71.7% of Theoretical Density.	57
Figure 5.12	FS-7 532X. Polarized Incident Light Shows Crystalline Phase. Immersion Density = 99.5% of Theoretical Density.	57
Figure 6.1	Absorptivity of Single Crystal Al_2O_3 .	60
Figure 6.2	Absorptivity of Single Crystal MgO .	61
Figure 6.3	Absorptivity of Single Crystal SrTiO_3 .	62

ILLUSTRATIONS (CONT'D.)

Figure 6.4	Absorptivity of Single Crystal CaF_2 .	63
Figure 6.5	Absorptivity of SiO_2 Glass.	64
Figure 7.1	Measured vs. Calculated Emissivity of Al_2O_3 (Al-1) 600°C .	70
Figure 7.2	Measured vs. Calculated Emissivity of Al_2O_3 (Al-1) 900°C .	71
Figure 7.3	Measured vs. Calculated Emissivity of Al_2O_3 (Al-1) 1150°C .	72
Figure 7.4	Measured vs. Calculated Emissivity of Al_2O_3 (Al-2) 590°C .	73
Figure 7.5	Measured vs. Calculated Emissivity of Al_2O_3 (Al-2) 895°C .	74
Figure 7.6	Measured vs. Calculated Emissivity of Al_2O_3 (Al-2) 1108°C .	75
Figure 7.7	Measured vs. Calculated Emissivity of Al_2O_3 (Al-3) 590°C .	76
Figure 7.8	Measured vs. Calculated Emissivity of Al_2O_3 (Al-3) 895°C .	77
Figure 7.9	Measured vs. Calculated Emissivity of Al_2O_3 (Al-3) 1108°C .	78
Figure 7.10	Measured vs. Calculated Emissivity of Al_2O_3 (Al-4) 590°C .	79
Figure 7.11	Measured vs. Calculated Emissivity of Al_2O_3 (Al-4) 900°C .	80
Figure 7.12	Measured vs. Calculated Emissivity of Al_2O_3 (Al-4) 1115°C .	81
Figure 7.13	Measured vs. Calculated Emissivity of Al_2O_3 (Al-6) 598°C .	82

ILLUSTRATIONS (CONT'D.)

Figure 7.14	Measured vs. Calculated Emissivity of Al_2O_3 (Al-6) 900°C.	83
Figure 7.15	Measured vs. Calculated Emissivity of Al_2O_3 (Al-6) 1150°C.	84
Figure 7.16	Measured vs. Calculated Emissivity of Silica Glass (FS-3) 610°C.	85
Figure 7.17	Measured vs. Calculated Emissivity of Silica Glass (FS-3) 905°C.	86
Figure 7.18	Measured vs. Calculated Emissivity of Silica Glass (FS-5) 590°C.	87
Figure 7.19	Measured vs. Calculated Emissivity of Silica Glass (FS-5) 885°C.	88
Figure 7.20	Measured vs. Calculated Emissivity of MgO (Mg-3) 595°C.	89
Figure 7.21	Measured vs. Calculated Emissivity of MgO (Mg-3) 908°C.	90
Figure 7.22	Measured vs. Calculated Emissivity of MgO (Mg-3) 1168°C.	91
Figure 7.23	Measured vs. Calculated Emissivity of MgO (Mg-5) 595°C.	92
Figure 7.24	Measured vs. Calculated Emissivity of MgO (Mg-5) 908°C.	93
Figure 7.25	Measured vs. Calculated Emissivity of MgO (Mg-5) 1168°C.	94
Figure 7.26	Measured vs. Calculated Emissivity of SrTiO_3 (Sr-1) 605°C.	95
Figure 7.27	Measured vs. Calculated Emissivity of SrTiO_3 (Sr-1) 897°C.	96

ILLUSTRATIONS (CONT'D.)

Figure 7.28	Measured vs. Calculated Emissivity of SrTiO_3 (Sr-2) 573°C .	97
Figure 7.29	Measured vs. Calculated Emissivity of SrTiO_3 (Sr-2) 892°C .	98
Figure 7.30	Measured vs. Calculated Emissivity of Commercial Al_2O_3 (AD-85) 935°C .	99
Figure 7.31	Measured vs. Calculated Emissivity of Commercial Al_2O_3 (AD-96) 910°C .	100
Figure 7.32	Measured vs. Calculated Emissivity of Commercial Al_2O_3 (AD-99) 915°C .	101
Figure 7.33	Measured vs. Calculated Emissivity of Commercial Al_2O_3 (AD-995) 954°C .	102
Figure 7.34	Measured vs. Calculated Emissivity of Commercial Al_2O_3 (AD-94) 947°C .	103
Figure 7.35	Measured vs. Calculated Emissivity of Commercial Al_2O_3 (AV-30) 952°C .	104
Figure 7.36	Measured vs. Calculated Emissivity of Commercial Al_2O_3 (AP-35) 910°C .	105
Figure 7.37	Blackbody Furnace.	106
Figure 7.38	Calibration Optical System.	107
Figure 7.39	Ratio of Energy Emitted by Blackbody Furnace to that Emitted by Rotating Slot Using Known Temperature Difference.	108
Figure 7.40	Ratio of Energy Emitted by Blackbody Furnace to that Emitted by Rotating Slot with Slight Misalignment.	109

ILLUSTRATIONS (CONT'D.)

Figure 9.1	Non-Isothermal Emissivity Apparatus.	114
Figure 9.2	Comparison of Isothermal and Non-Isothermal Emissivity of an Al_2O_3 Body (Western Gold and Platinum Company, Al-300-96%, SiO_2 -4%). Non-Isothermal Radiating Surface at 898°C - Thermal Gradient $60^\circ\text{C}/\text{cm}$. Isothermal Radiating Surface at 895°C .	117

TABLES

Table 2.1	Total Reflectivity for Diffuse Radiation and for Radiation at Normal Incidence (After Ryde and Cooper ⁴).	4
Table 2.2	Expected Normal and Hemispherical Emissivity for Smooth Surfaces Having Given Values of the Refractive Index (for Samples with $a \gg s$).	21
Table 2.3	Ratio of the Normal to Hemispherical Emissivities for Varying Index of Refraction.	28
Table 3.1	Input Constants and Comparison of Results of Exact and Hamaker Equations for 20 Conditions.	40

SYMBOLS

a	Absorption coefficient for diffuse radiation in a material containing scattering centers
A	Hamaker constant see Eq. 3.18
b	Radiation constant see Eq. 3.10
B	Hamaker constant see Eq. 3.19
C	Hamaker constant see Eq. 3.20
C_1	Constant in Wien's equation
C_2	Constant in Wien's equation
d	Thickness of sample
D	Hamaker constant see Eq. 3.21
E_n	Exponential integral of order n . Ref. 5, Appendix I, p. 373
f	Forward scattering coefficient for diffuse radiation
f'	Forward scattering coefficient for parallel radiation
F	Net radiative flux defined by $\pi F = I - J$
F_n	Special function defined in Ref. 5, Appendix I
g'	Absorptive coefficient used by Ryde
$G'_{2,2}$	Special function defined in Ref. 5, Appendix I
H	Net heat flux
I	Radiant energy flux in the direction of the positive x -axis
I_0	Radiant energy flux in the direction of the positive x -axis at $x = 0$
I'	Specific intensity of radiation
I'_0	Specific intensity of forward radiation at $x = 0$
I_p	Parallel forward flux
I_{p_i}	Parallel flux incident on surface of slab
$\overline{I'}$	Average specific energy
$I'_{e'}$	Specific intensity of refracted radiation
I'_s	Specific intensity of radiation scattered once
I'_{ns}	Specific intensity of radiation not scattered

SYMBOLS (CONT'D.)

j^1	Emission coefficient for once scattered radiation
J	Radiant energy flux in the direction of the negative x-axis
J_0	Radiant energy flux in the direction of the negative x-axis at $x = 0$
k	Lattice thermal conductivity
K	Scattering factor (non-dimensional)
l	Path length in direction θ
m	Reciprocal index of refraction; $m = 1/n$
n	Index of refraction
N	Number of pores per unit volume
p	Dimensionless parameter $p = 4\pi r m-1 /\lambda m$
P	Volume fraction porosity
r	Pore radius
s	Backward scattering coefficient for diffuse radiation (scattering factor in Hamaker equations)
s'	Backward scattering coefficient for parallel radiation
S	Scattering coefficient for parallel radiation
S_{diffuse}	Scattering coefficient for diffuse radiation
t	Dimensionless parameter $t = (\alpha + S)x$
t'	Dimensionless parameter $t' = (\alpha + S)x'$
T	Absolute temperature
U	Material constant defined by Eq. 2.69
V	Material constant defined by Eq. 2.70
x	Distance along x-axis
α	Absorption coefficient
β	Material constant; $\beta = \sigma/(a + 2s)$
β_0	Material constant; $\beta_0 = \sigma_0/(a + 2s)$
γ	Euler's constant; $\gamma = 0.5772156\dots$

SYMBOLS (CONT'D.)

Δ	Constant denominator defined in Eq. 4.23
ϵ	Emissivity
ϵ_n	Normal emissivity
ϵ_h	Hemispherical emissivity
θ	Angle measured from x-axis within the sample
θ'	Angle measured from x-axis outside the sample
κ	Material constant defined by Hamaker
	$\kappa = \frac{2b\beta}{k\sigma}$
λ	Wavelength of radiation in free space
ρ	Reflectivity
ρ_i	Reflectivity of diffuse energy emerging from the sample
ρ_o	Reflectivity of diffuse energy incident on the sample
ρ_n	Reflectivity for normal incidence
σ	Material constant for non-isothermal case
	$\sigma = \sigma_o \sqrt{1 + \kappa}$
σ_o	Material constant $\sigma_o = \sqrt{a(a+2s)}$
σ'	Stefan-Boltzmann constant
ϕ	Azimuthal angle
ψ	Spectral radiant energy
ω	Solid angle

1.0 INTRODUCTION

The evaluation of ceramic oxides for high-temperature applications and the design of high-temperature structures require a precise knowledge of the thermal gradients in and radiant heat transfer to and from solid bodies. Energy transfer through these systems is by two modes: radiation and lattice conduction. Interactions between these heat transfer modes can cause large deviations from linear temperature gradients near surfaces.

Emissivity has been widely used as a material constant characterizing what is often considered as a surface phenomena. However, for oxide materials which are partially transparent in the important 0.5-8 micron wavelength range, radiant energy emission is a volume process. As a result there is no simple "emissivity" for a material like alumina, but the radiant energy emitted depends on temperature gradients and also on material characteristics such as absorption and scattering coefficients. Thus, the nomenclature often used for opaque solids with "emittance" taken as a sample characteristic, while "emissivity" is a material constant is not applicable. We will use the term "emissivity" for the ratio of energy emitted from an isothermal sample to the energy emitted from an ideal black body at the same temperature, fully recognizing that this is a sample characteristic rather than a material constant.

In the present investigation we have been mainly concerned with evaluating the material characteristics for well defined systems, developing a method for calculating the

Manuscript released by the author, July 1964, for publication as an RTD Technical Documentary Report.

isothermal emissivity from these characteristics, and comparing the calculated results with direct experimental measurements. This is an ambitious approach, but if successful, it allows us (a) to estimate the thermal emissivity from material characterization rather than having to make expensive and difficult measurements on every sample, and (b) to evaluate the effect of changing material characteristics on thermal emissivity behavior and thus provide a rational basis for new material development.

In addition we have evaluated the basic Ryde¹-Hamaker² equations for calculating and applying isothermal and non-isothermal emissivities, extended the Hamaker relation to new boundary conditions, and developed a technique and apparatus for carrying out controlled measurements of non-isothermal emissivity.

2.0 CALCULATION OF ISOTHERMAL EMISSIVITY FROM MATERIAL CHARACTERIZATION

The material factors which enter the expression for isothermal emissivity are the reflectivities for entering and leaving radiation and the material constant,

$$\beta_o = \sqrt{a/(a + 2s)}$$

where a and s are the absorption and scattering coefficients discussed subsequently. The emissivity for a thick sample is given by:

$$(1 - \epsilon) = \frac{(1 - \rho_i)^2 + 2\beta_o(1 - \rho_i)(\rho_o + \rho_i) - \beta_o^2(1 + \rho_i)(1 - \rho_i - 2\rho_o)}{(1 - \rho_i)^2 + 2\beta_o(1 - \rho_i)^2 + \beta_o^2(1 + \rho_i)^2} \quad (2.1)$$

where ρ_i is the reflectance of diffuse radiant energy emergent from the solid and ρ_o is the reflectance of diffuse radiant energy incident on the solid. Thus calculation of emissivity requires evaluation of ρ_i , ρ_o , and β_o .

As discussed by Folweiler³ the ratio a/s can be measured independently of the emissivity by measuring diffuse transmissivity of thin samples. Unfortunately, the measurements are not very precise. For example, two measurements of transmissivity for beryllia gave values within $\pm 3\%$. However, calculations of $\sigma_o = \sqrt{a(a + 2s)}$ gave values different by a factor of two and the a/s ratios varied by a factor of five; this leads to a difference in calculated emissivity of a little less than a factor of two. The magnitude of these errors results from the fact that the calculations depend on a rela-

tively small difference between large measured values, and is inherent in the form of the mathematical relationships between variables.

2.1 Reflectivity

The total reflectivity for diffuse radiation incident on a surface depends on the index of refraction of the solid as discussed by Ryde¹ and Ryde and Cooper.⁴ Values for a range of refractive indices are listed in Table 2.1.

Table 2.1
Total Reflectivity for Diffuse Radiation and for Radiation at Normal Incidence (After Ryde and Cooper⁴).

<u>Index of Refraction</u>	<u>Total Reflectivity</u>	
	<u>normal incidence</u>	<u>diffuse radiation</u>
1.00	0	0
1.1	0.0023	0.026
1.15	0.0049	0.035
1.2	0.0083	0.045
1.25	0.012	0.053
1.3	0.017	0.061
1.35	0.022	0.069
1.4	0.028	0.077
1.45	0.033	0.085
1.5	0.040	0.092
1.55	0.047	0.100
1.6	0.053	0.107
1.65	0.060	0.114
1.7	0.067	0.121
1.8	0.082	0.134
1.9	0.096	0.146

From the values of ρ_o given in 2.1, we can obtain the reflectivity of emergent radiation, ρ_i , from the relation:

$$\rho_i = 1 - \frac{(1-\rho_o)}{n^2} \quad (2.2)$$

2.2 The Absorption Coefficient, a

The absorption coefficient, a , in the Hamaker relation refers to the absorption of energy from diffuse radiation as it passes through a body containing scattering centers. In contrast, the intrinsic absorption coefficient, α , is measured by and refers to the absorption of energy from parallel radiation in a body without scattering centers.

Thus, application of measured values of α to calculation of β_o must take into account the larger path length for diffuse radiation as it passes through a thin layer of thickness dx . Let us consider the specific intensity of radiation, I' , where θ measures the angle from the x direction (see Fig. 2.1). We consider situations in which I' varies with angle θ from the x direction, but is independent of the azimuthal angle (i.e., symmetrical about the x axis); that is, $I' = I'(x, \theta)$. Consider first an intensity field in free space specified by

$$I'(x, \theta) = I'_o \quad \text{for } 0 \leq \theta \leq \pi/2, \quad (2.3)$$

$$\text{and } I'(x, \theta) = 0 \quad \text{for } \pi/2 < \theta \leq \pi.$$

This field is isotropic over the left and right hemispheres separately, and the flux associated with this field is

$$\pi F = \int_{\omega} I' \cos \theta \, d\omega \quad (2.4)$$

where the integration is over all solid angles.

Then,

$$\begin{aligned} \pi F &= \int_{\phi=0}^{2\pi} \int_{\theta=0}^{\pi} I'(x, \theta) \cos \theta \sin \theta d\theta d\phi = \\ &= 2\pi \int_{\theta=0}^{\pi/2} I'_0 \cos \theta \sin \theta d\theta = \pi I'_0. \end{aligned} \quad (2.5)$$

So, $F = I'_0$.

Now suppose that instead of free space we specify this radiation field for $0 \leq \theta \leq \pi/2$ on the plane $x = 0$ in a material with absorption coefficient α per unit length. At $x = d$ we specify that no radiation is incident on the material from the right. Then, the intensity I' must satisfy

$$\frac{d I'(x, \theta)}{d l} = - \alpha I'(x, \theta) \quad (2.6)$$

where l measures path length in the direction θ . Clearly, $l = x \sec \theta$. So,

$$\frac{d I'}{d x} = -\alpha \sec \theta I',$$

$$I'(x, \theta) = I'(0, \theta) \exp [-\alpha x \sec \theta] \quad 0 \leq \theta \leq \frac{\pi}{2},$$

$$\text{and } I'(x, \theta) = I'(d, \theta) \exp [-\alpha (x-d) \sec \theta] \quad \frac{\pi}{2} < \theta \leq \pi, \quad (2.7)$$

But we specify $I'(0, \theta) = I'_0$ for $0 \leq \theta \leq \pi/2$,

and $I'(d, \theta) = 0$ for $\pi/2 < \theta \leq \pi$.

So,

$$I'(x, \theta) = I'_0 \exp[-\alpha x \sec \theta] \text{ for } 0 \leq \theta \leq \pi/2, \quad (2.8)$$

$$\text{and } I'(x, \theta) = 0 \text{ for } \pi/2 < \theta \leq \pi. \quad (2.9)$$

The flux is given by

$$\pi F(x) = \int_{\omega} I'(x, \theta) \cos \theta \, d\omega. \quad (2.10)$$

$$\pi F(x) = 2\pi \int_0^{\pi/2} I'_0 \exp(-\alpha x \sec \theta) \cos \theta \sin \theta \, d\theta. \quad (2.11)$$

Since $\cos \theta = (\sec \theta)^{-1}$; $\frac{d \sec \theta}{(\sec \theta)^2} = \sin \theta \, d\theta$, and

$$F(x) = 2 I'_0 \int_1^{\infty} \exp(-\alpha x \sec \theta) \frac{d \sec \theta}{(\sec \theta)^3} = 2 I'_0 E_3(\alpha x) \quad (2.12)$$

where E_3 is the exponential integral of order 3 given by Chandrasekhar,⁵ Appendix I, (p. 373).

For a small argument, E_3 has the power series expansion

$$E_3(z) = 1/2 - z + 1/2 (-\gamma - \ln z + 3/2) z^2 + \frac{1}{6} z^3 + \dots \quad (2.13)$$

where γ is Euler's constant (see Van de Hulst,⁶ p. 244). Thus,

$$F(x) = I'_0 (1 - 2\alpha x + O(\alpha^2 x^2)). \quad (2.14)$$

So for optically thin slabs, we have

$$\frac{F(x) - F(0)}{F(0)} = -2\alpha x. \quad (2.15)$$

That is, the equivalent absorption coefficient for diffuse radiation in a thin slab is

$$a = 2\alpha. \quad (2.16)$$

When there are scattering centers present the analysis is complicated by the fact that, as a result of scattering, some path lengths are increased and some path lengths are decreased. Thus it is not obvious whether scattering will increase or decrease a . If we consider a slab of material between $x = 0$ and $x = d$, let the material contain a random distribution of scattering centers that scatter isotropically with a scattering coefficient S per unit path length. We consider the situation in which the intensity just inside the left boundary (at $x = 0+$) is given by

$$I'(0+, \theta) = I'_0 \text{ for } 0 \leq \theta \leq \pi/2, \quad (2.17)$$

and just inside the right boundary (at $x = d-$) is given by

$$I'(d-, \theta) = 0 \text{ for } \pi/2 < \theta \leq \pi.$$

Let I'_{ns} be the intensity of radiation which has not been scattered at all, and I'_s the intensity of once scattered radiation. The only source of I'_{ns} is at the boundary $x = 0$. In the material I'_{ns} is decreased by two processes. Some is absorbed by the material; this process is characterized by the absorption coefficient, α . The other process that decreases I'_{ns} is scattering (this energy goes into I'_s) which

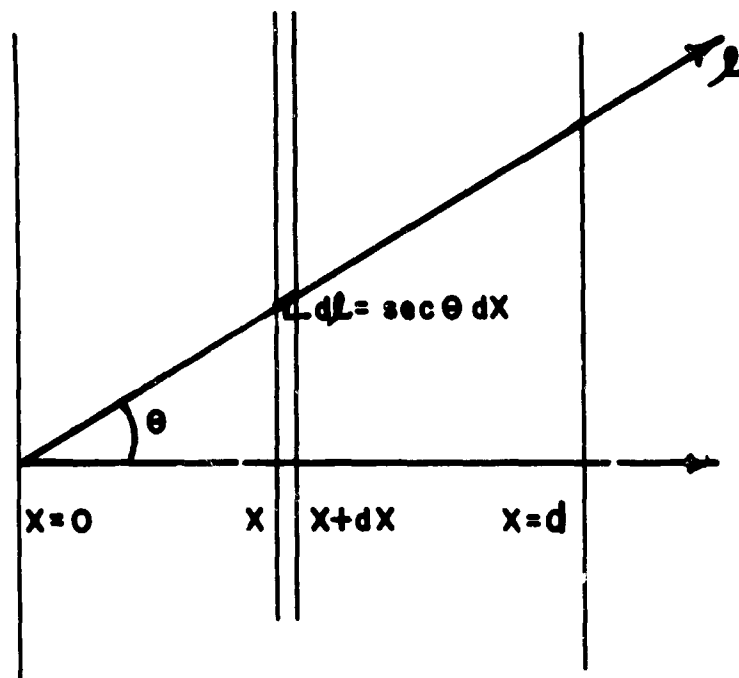


Fig. 2.1 Diagram of geometry of radiation in a thin slice of absorbing material.

may be characterized by the scattering coefficient S . Taking both absorption and scattering into account,

$$\frac{dI'}{d(x \sec \theta)} = - (\alpha + S) I'_{ns} \quad (2.18)$$

and the solution satisfying the boundary conditions is

$$I'_{ns} = I'_0 \exp [-(\alpha + S) x \sec \theta] \text{ for } 0 \leq \theta \leq \pi/2,$$

$$\text{and } I'(x, \theta) = 0 \text{ for } \pi/2 < \theta \leq \pi. \quad (2.19)$$

Now the amount of radiation scattered in all directions per unit volume of material from $I'_{ns}(x, \theta)$ is $S I'_{ns}(x, \theta)$. Scattering is isotropic, so the amount scattered per unit volume per unit solid angle is $(S/4\pi) I'_{ns}(x, \theta)$.

Integrating this over all directions of incoming radiation gives the emission coefficient j^1 for once scattered radiation. j^1 is defined as the amount of radiant energy emitted per unit volume per unit time per unit solid angle (due to scattering of I'_{ns}). So we have

$$j^1 = \frac{S}{4\pi} \int_{\omega} I'_{ns}(x, \theta) d\omega = \frac{S}{4\pi} \int_{\theta=0}^{\pi} \int_{\phi=0}^{2\pi} I'_{ns}(x, \theta) \sin \theta d\phi d\theta. \quad (2.20)$$

$$j^1 = \frac{S}{2} \int_0^{\pi} I'_{ns}(x, \theta) \sin \theta d\theta = \frac{S}{2} \int_0^{\pi/2} I'_0 \exp [-(\alpha + S) x \sec \theta] \sin \theta d\theta. \quad (2.21)$$

Let $\mu = \cos \theta$.

$$j^1 = \frac{SI'_0}{2} \int_0^1 \exp \left[-(\alpha+S) \frac{x}{\mu} \right] d\mu = \frac{SI'_0}{2} E_2 [(\alpha+S)x], \quad (2.22)$$

where E_2 is the exponential integral of order 2.

The equation of transfer (see Chandrasekhar,⁵ p. 6) for once scattered radiation is

$$\frac{dI'_s}{\sec \theta dx} = -(\alpha+S)I'_s + j^1 = -(\alpha+S)I'_s + \frac{SI'_0}{2} E_2 [(\alpha+S)x] \quad (2.23)$$

This may be written as

$$-\frac{1}{(\alpha+S) \sec \theta} \frac{dI'_s}{dx} = I'_s - \frac{S}{2(\alpha+S)} I'_0 E_2 [(\alpha+S)x] \quad (2.24)$$

For $0 \leq \theta \leq \pi/2$ the boundary condition is $I'_s(0+, \theta) = 0$, and for $\pi/2 < \theta \leq \pi$ the boundary condition is $I'_s(d-, \theta) = 0$. The solution to the equation which satisfies this boundary condition is

$$I'_s(x, \theta) = \frac{SI'_0}{2} \int_0^x E_2 [(\alpha+S)x'] \exp [-(\alpha+S) \sec \theta (x-x')] \sec \theta dx' \quad \text{for } 0 \leq \theta \leq \frac{\pi}{2}. \quad (2.25)$$

Let $t' = (\alpha+S)x'$ and $\mu = \cos \theta$. Then,

$$I'_s(x, \theta) = \frac{SI'_0}{2} \frac{\sec \theta}{(\alpha+S)} \exp [-(\alpha+S) \sec \theta x] \int_0^t E_2(t') \exp (t'/\mu) dt' \quad (2.26)$$

$$= \frac{SI'_0 \sec \theta}{2(\alpha+S)} \exp [-(\alpha+S) \sec \theta x] F_2(t, \mu) \quad (2.27)$$

for $0 \leq \theta \leq \pi/2$.

where $t = (\alpha + S)x$ and F_2 is defined in Appendix 1 of Chandrasekhar.⁵ He gives

$$F_2(t, \mu) = [F_1(t, \mu) + \exp(t/\mu) E_2(t) - 1]. \quad (2.28)$$

So,

$$I'_s(x, \theta) = \frac{SI'_0}{2(\alpha + S)} [\exp(-t/\mu) F_1(t, \mu) + E_2(t) - \exp(-t/\mu)] \quad (2.29)$$

$$\text{for } 0 \leq \theta \leq \pi/2.$$

Now let $I' = I'_{ns} + I'_s$ and neglect all higher order scattering. This is a good approximation if the slab of material is optically thin. We wish to calculate the flux of energy across any plane $x = \text{const.}$ This is given by

$$\pi F(x) = \int_{\omega} I'(x, \theta) \cos \theta \, d\omega = 2\pi \int_0^{\pi} I'(x, \theta) \cos \theta \sin \theta \, d\theta \quad (2.30)$$

$$\pi F(x) = 2\pi \int_0^{\pi} [I'_{ns}(x, \theta) + I'_s(x, \theta)] \cos \theta \sin \theta \, d\theta \quad (2.31)$$

$$\text{Now we know } I'_{ns}(x, \theta) = I'_0 \exp[-(\alpha + S)x \sec \theta] \text{ for } 0 \leq \theta \leq \pi/2 \quad (2.32)$$

$$\text{and } I'_{ns}(x, \theta) = 0 \text{ for } \pi/2 < \theta \leq \pi. \quad (2.33)$$

Also $I'_s(x, \theta)$ is known for $0 \leq \theta \leq \pi/2$. But we also need to know I'_{ns} for $\pi/2 < \theta \leq \pi$ to do the complete flux integral. We have not solved for I'_s for these angles and we do not need to if we restrict ourselves to calculating the flux at $x = d$, where the boundary condition is $I'_s(d, \theta) = 0$, $\pi/2 < \theta \leq \pi$.

That is, no scattered radiation comes from the right. Using this fact, we have

$$\pi F(d) = 2\pi \int_0^{\pi/2} [I'_{ns}(d, \theta) + I'_s(d, \theta)] \cos \theta \sin \theta d\theta \quad (2.34)$$

$$= 2\pi I'_o E_3[(\alpha+S)d] + \frac{\pi S I'_o}{\alpha+S} \int_0^1 \exp[-(\alpha+S)d/\mu] F_2[(\alpha+S)d, \mu] d\mu. \quad (2.35)$$

Thus the integral is recognizable as the function $G'_{2,2}[(\alpha+S)d]$ given by Chandrasekhar⁵ in Appendix 1.

So,

$$\pi F(d) = 2\pi I'_o [E_3[(\alpha+S)d] + \frac{S}{2(\alpha+S)} G'_{2,2}[(\alpha+S)d]] \quad (2.36)$$

Van de Hulst gives power series expansion of E_3 and $G'_{2,2}$ in Appendix 1 of his 1948 paper in Astrophys. J.⁶

$$E_3(x) = 1/2 - x + 1/2 (-\gamma - \ln x + 3/2) x^2 + \dots \quad (2.37)$$

$$G'_{2,2}(x) = x + (\gamma + \ln x - 3/2) x^2 + \dots \quad (2.38)$$

where $x > 0$, and γ is Euler's constant.

So, for $(\alpha+S)d \ll 1$ we have,

$$\pi F(d) = 2\pi I'_o \left[\frac{1}{2} - (\alpha+S)d + O[(\alpha+S)^2 d^2] + \frac{S}{2(\alpha+S)} \{ (\alpha+S)d + O[(\alpha+S)^2 d^2] \} \right] \quad (2.39)$$

$$\pi F(d) = 2\pi I'_o \left[\frac{1}{2} - (\alpha+S/2)d + O[(\alpha+S)^2 d^2] \right] \quad (2.40)$$

So,

$$\frac{\pi F(d)}{\pi F(0)} = 1 - (2\alpha + s)d + 0 [(\alpha+s)^2 d^2] \quad (2.41)$$

This result has an easy physical interpretation. For an optically thin slab of thickness d , a fraction $2(\alpha+s)d$ of the incident flux is absorbed or scattered. Of the fraction $2dS$ which is scattered, half goes into backward flux and half into forward flux, since scattering is isotropic. Neglecting further scattering and absorption, we see that a fraction Sd of the original flux is added to the forward flux by scattering. A fraction $2(\alpha+s)d$ is removed by absorption scattering and a fraction Sd is added by the scattering. So the net fraction removed is $(2\alpha+s)d$. That is, the absorption coefficient appropriate to the Hamaker conditions is not affected by isotropic scattering centers, and Eq. 2.16 is the appropriate one to use for calculating a .

2.3 The Scattering Coefficient, s

The scattering coefficient, s , as used in the Hamaker equations refers to back scattering of diffuse radiation. In contrast, the commonly measured and calculated scattering coefficient, S , refers to total scattering for parallel radiation. Assuming, as Hamaker did, diffuse radiation, by the same analysis as given for the absorption coefficient above, $S_{\text{diffuse}} = 2S$; taking only the back scattering (assuming isotropic scattering) as shown in Eq. 2.41,

$$s = \frac{1}{2} S_{\text{diffuse}} = S \quad (2.42)$$

The scattering coefficient, S , is related to the number of pores per unit volume, N , and the pore radius, r , by the scattering factor, K , in the relation

$$S = K N (\pi r^2) \quad (2.43)$$

If the volume fraction porosity is P ,

$$S = \frac{3}{4} K \frac{P}{r} \quad (2.44)$$

The scattering factor K varies between zero and four and depends on the pore radius, r , wavelength of radiation, λ , and the relative index of the scattering center and medium m . Van de Hulst⁷ has summarized solutions for a number of systems in terms of the dimensionless parameter, $p = 4\pi r |m-1| / \lambda m$.

R. H. Boll, R. D. Gumprecht, and C. M. Sliepcevich⁸ have calculated the scattering factor K from the Mie equations for values of the relative refractive index of 0.93, 0.9, and 0.8 corresponding to our situation of spherical pores in a solid media. Their results show that the excursions of K from an average value near 2 are less marked as m decreases. D. W. Lee and W. D. Kingery⁹ extrapolated Boll et al's results to lower values of m and compared calculated and directly measured scattering coefficients for alumina and Vycor having pore sizes in the range 0.7-7 microns with good results (agreement within about $\pm 10\%$).

Now a basic question is "How isotropic is the scattering by pores in an oxide matrix?" That is, can we

use the available calculations for the total scattering coefficient discussed above to evaluate the back scattering appropriate to the Hamaker relation?

The angular intensity distribution of the scattered radiation depends on the size of the scattering center, the wavelength of radiation, and the relative refractive index. For very small particles (relative to the wavelength) scattering is nearly isotropic. For very large particles having an index of refraction greater than the media ($m > 1$), the scattering is almost completely forward. However, for the reverse case, pores of lower index embedded in a media of higher index, this is not the case. As shown in Fig. 2.2 when $m = 0$, the back scattering is just half the total scattering.⁷ For Al_2O_3 and MgO , the back scattering is about 25% for the total scattering.

For wavelengths of 0.5-8 microns and pore sizes from 0.5-5 microns (experimentally observed) we cover the gamut from "very small" to "very large" pores. Complete solutions of the Mie equations would be required for the intermediate range. Since the relative index enters each term of the required summations, there is no easy way to transpose available solutions to the case of scattering pores in a solid matrix.

Fortunately, the relative values of forward and backward scattering for pores in a solid matrix cover a much narrower range than is found for the more usual case of solid particles in a matrix of lower refractive index. For pores in alumina, for example, we can write:

$$\frac{3}{8} K \frac{P}{r} < S < \frac{3}{4} K \frac{P}{r} \quad (\text{Al}_2\text{O}_3) \quad (2.45)$$

That is, we can calculate the appropriate back scattering coefficient to better precision than it can be evaluated from measurements of diffuse transmissivity.

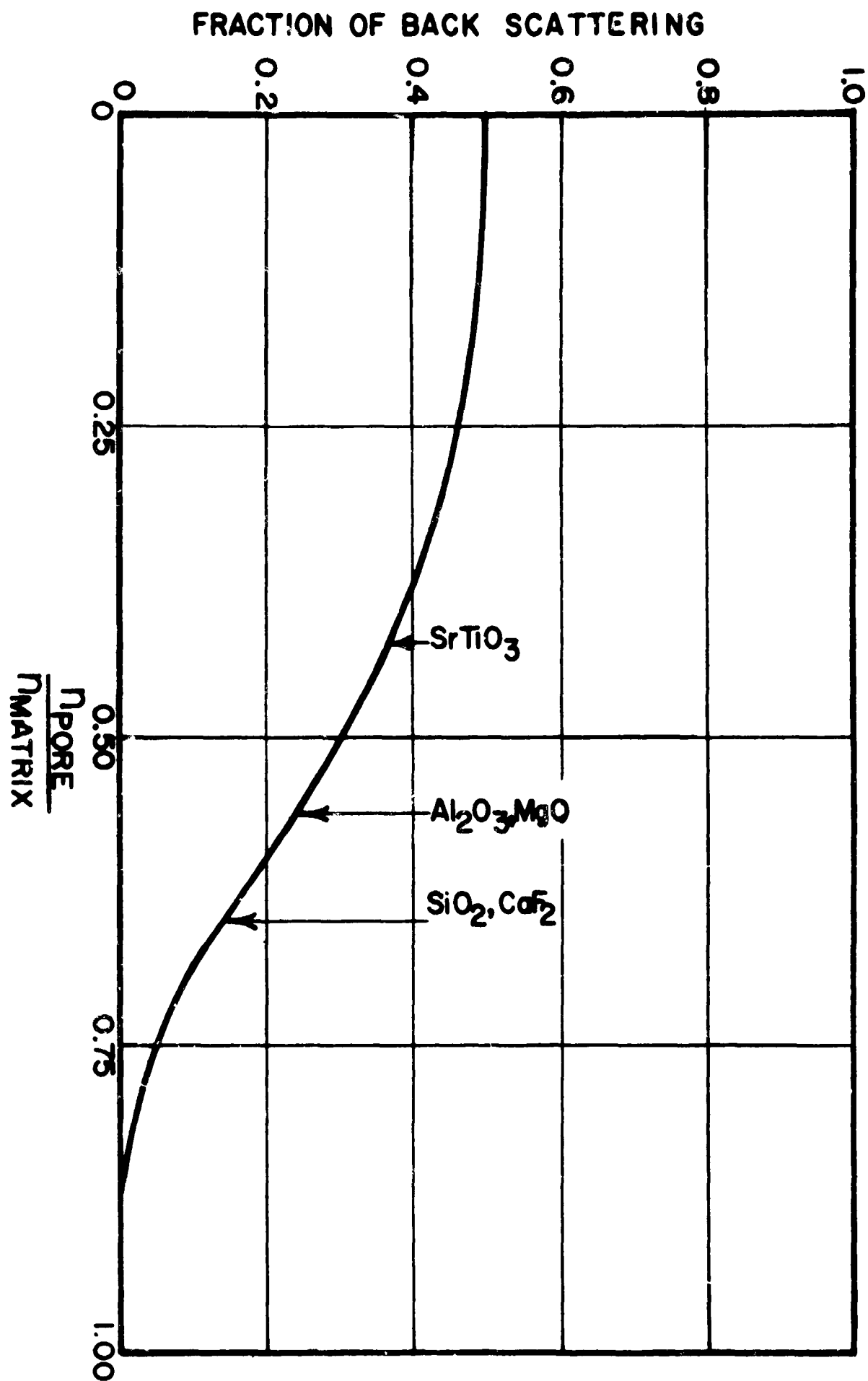


Fig. 2.2 Relative Fraction of Back Scattering for Pores of Large Size in a Solid Matrix.

It should be recognized that this calculation is appropriate only for pores in a solid matrix -- which is the system we are concerned with. It is not applicable to more complex multiphase compositions in which scattering centers have a higher index than the matrix material.

2.4 The Material Constant, β_o

The constant, $\beta_o = \sqrt{a/(a+2s)}$ can be calculated directly from values of a and s determined as described in the previous section. Since this calculation involves taking the square root of s , the precision of calculating β_o is better than the evaluation of s . That is, the maximum expected two-fold error in s leads to only a $\sqrt{2}$ error in β_o .

2.5 Calculation of Emissivity in the Wavelength Range 0.5-8 Microns

In this range of wavelengths emissivity is a volume process, and calculations have been made from Eq. (2.1). Values of the reflectivities for each wavelength were taken from Table 1. Values of the appropriate absorption coefficient were calculated for each wavelength from measured values of the intrinsic absorption coefficient with Eq. (2.16). Values of the appropriate back scattering coefficient were calculated for each wavelength and pore size from Eq. (2.44) using values of the scattering factor K taken from Fig. (2.3).

Results are compared with directly measured isothermal emissivity in Section 8.0.

2.6 Calculation of Emissivity in the Wavelength Range 8-15 Microns

At wavelengths above 5-8 microns, the absorption coefficient increases to such an extent that emissivity becomes

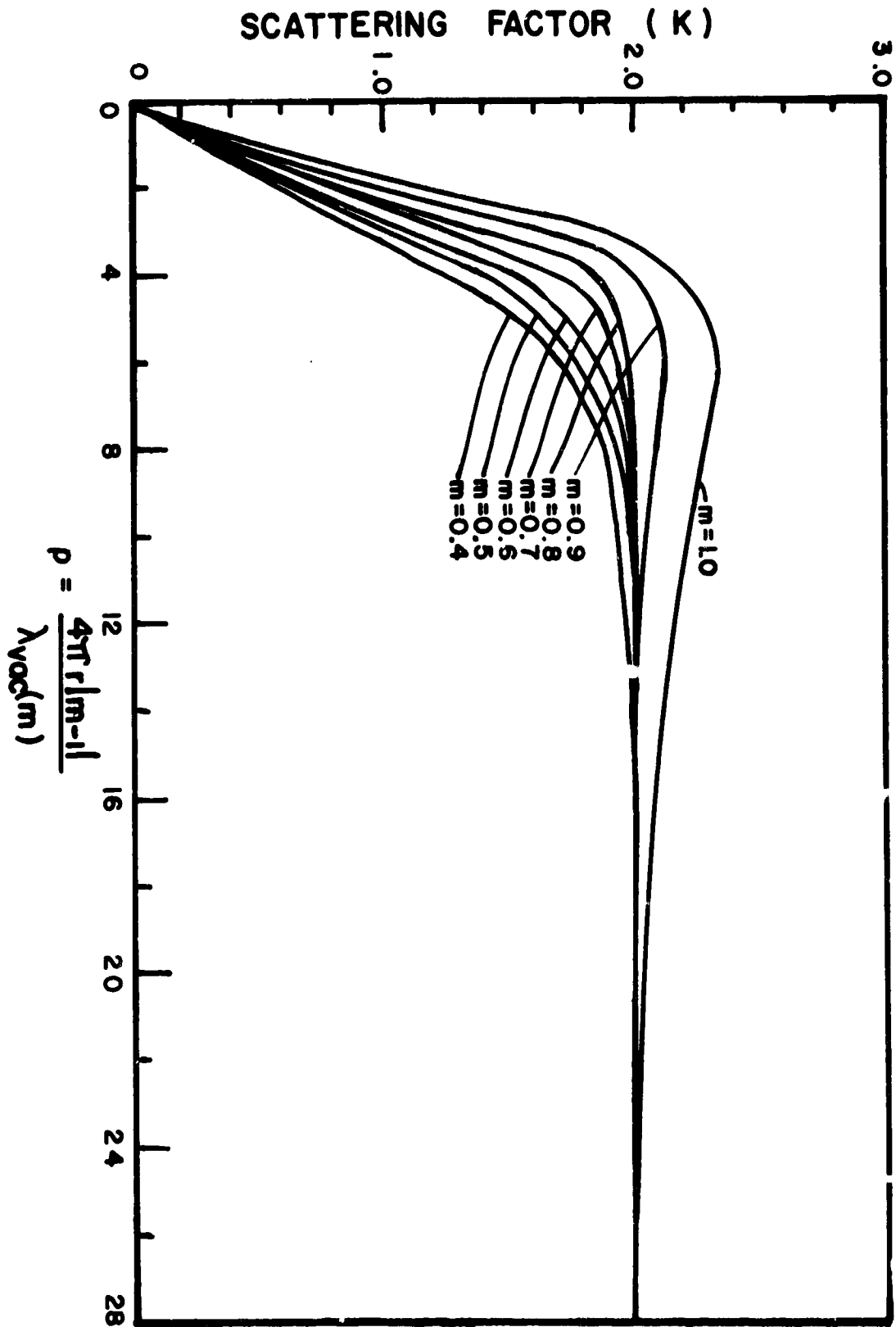


Fig. 2.3 Values of the Scattering Factor K for Various Values of the Relative Index, m , When $m < 1$.

a surface process depending on the reflectivity. Eq. (2.1) reduces to:

$$1 - \epsilon = \rho_o \quad (2.46)$$

Emissivity values can then be calculated directly from the data in Table 2.1

At variable wavelengths, which are above 10-12 microns for most oxides the restrahl frequency is approached, the reflectivity increases and the emissivity drops off. We have not analyzed behavior in this wavelength region in detail.

2.7 Normal vs. Hemispherical Emissivity

In the calculations discussed thus far, we have been concerned with the spectral hemispherical emissivity, while our experimental measurements have been for spectral normal emissivity.

For the wavelength range 8-15 microns where emissivity is essentially a surface process, and Eq. (2.46) applies, the difference is directly related to the difference in normal and diffuse reflectivity as given in Table 2.1. Comparable expected emissivity values are given in Table 2.2.

For the wavelength range below about 8 microns where emissivity is a volume process, we are concerned with the angular distribution of the emergent radiation. Radiation of intensity I'_θ at angle θ will be partly reflected and partly refracted at the surface. Assuming isotropic diffuse radiation just below the surface we can calculate the angular intensity distribution of the emergent radiation.

Table 2.2.

Expected Normal and Hemispherical Emissivity for Smooth Surfaces Having Given Values of the Refractive Index (for Sample with $a \gg s$).

<u>Refractive Index</u>	<u>Normal Emissivity</u>	<u>Hemispherical Emissivity</u>
1.1	.998	.974
1.2	.992	.955
1.3	.983	.939
1.4	.972	.923
1.5	.960	.908
1.55	.957	.900
1.6	.947	.893
1.65	.940	.886
1.7	.933	.879
1.8	.918	.866
1.9	.904	.854

Let dI be the rate of transport of radiant energy per unit area in directions confined to an element of solid angle $d\omega$ (see Fig. 2.4). dI is then expressed in terms of intensity I' :

$$dI = I' \cos \theta d\omega. \quad (2.47)$$

Consider isotropic radiation of intensity I' incident on a plane interface. Of the energy dI incident on a unit area from the solid angle

$$d\omega = \sin \theta d\theta d\phi \quad (2.48)$$

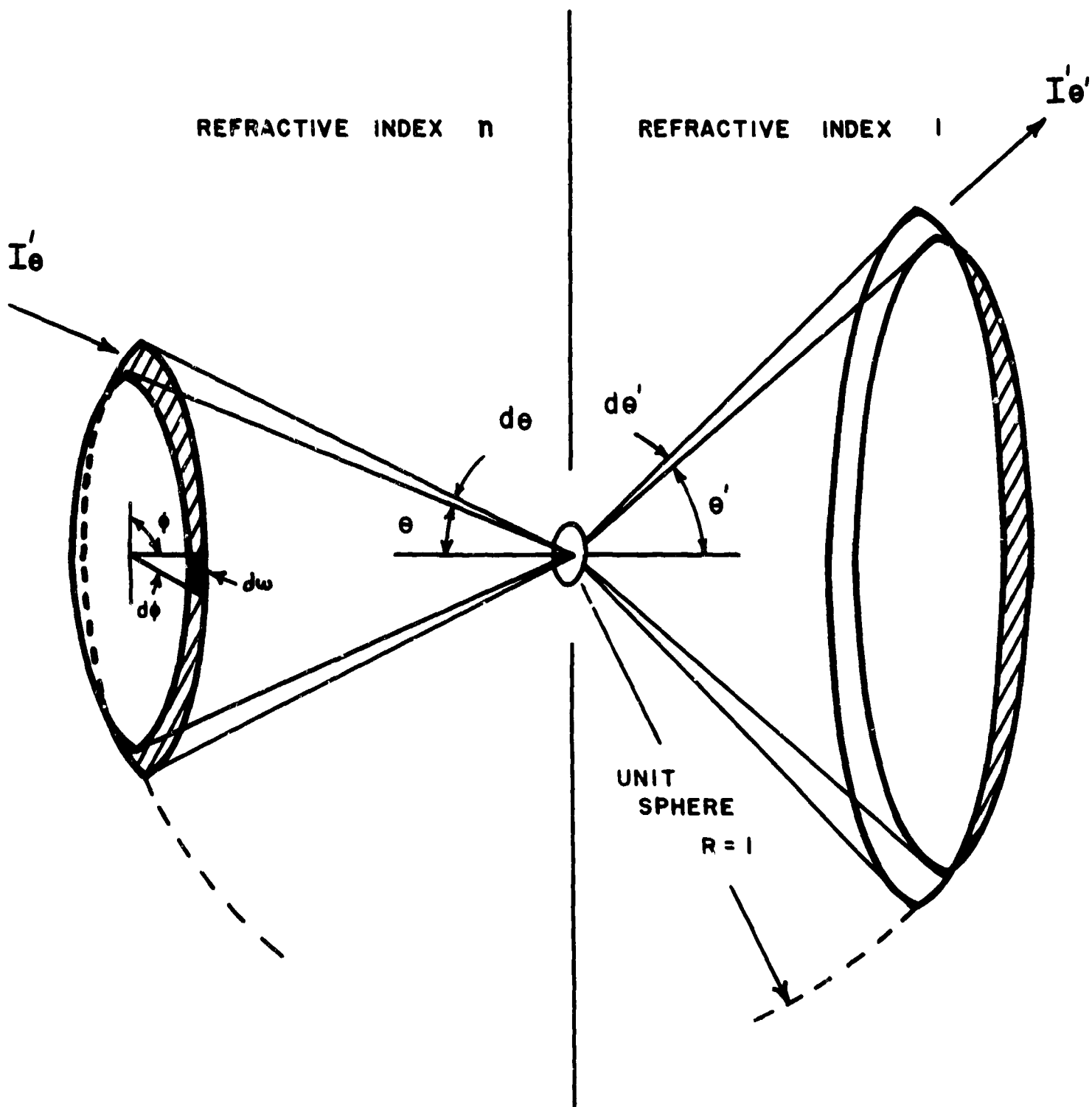


Fig. 2.4 Diagram of Geometry of Diffuse Radiation Leaving a Material of Index n (where $n > 1$).

$r_{\theta} dI$ is reflected and $(1-r_{\theta}) dI$ is refracted into the solid angle

$$d\omega' = \sin \theta' d\theta' d\phi' \quad (2.49)$$

where

$$\begin{aligned} \phi &= \phi' \\ \sin \theta' &= n \sin \theta \end{aligned} \quad (2.50)$$

The intensity $I'_{\theta'}$ of the refracted radiation is defined by

$$(1-r_{\theta}) dI = I'_{\theta'} \cos \theta' d\omega' \quad (2.51)$$

which, with the use of equations (2.47), (2.48) and (2.49) becomes

$$(1-r_{\theta}) I' \cos \theta \sin \theta d\theta d\phi = I'_{\theta'} \cos \theta' \sin \theta' d\theta' d\phi \quad (2.52)$$

From equation (2.50)

$$\cos \theta' \sin \theta' d\theta' = n^2 \cos \theta \sin \theta d\theta \quad (2.53)$$

and using (2.53) in (2.52)

$$I'_{\theta'} = \left(\frac{1-r_{\theta}}{n^2} \right) I' \quad (2.54)$$

The reflectivity is given by the well-known Fresnel equation

$$r_{\theta} = \frac{1}{2} \left[\frac{\sin^2(\theta-\theta')}{\sin^2(\theta+\theta')} + \frac{\tan^2(\theta-\theta')}{\tan^2(\theta+\theta')} \right] \quad (2.55)$$

Then for any value of n , we can calculate the angular distribution of the relative intensity of the reflected and transmitted energy. This is shown for Al_2O_3 ($n = 1.7$) in Fig. 2.5. The relative values of the normal and hemispherical emissivity are determined by comparing the normal intensity to the average value integrated over all wavelengths.

The integrated energy flux rate per unit area is

$$I = \int_{\text{hemisphere}} I'_{\theta'} \cos \theta' d\omega' = \pi \int_0^{\pi/2} I'_{\theta'} \sin 2\theta' d\theta' \quad (2.56)$$

where use has been made of equation (2.49) and the integration over the azimuthal angle ϕ has been carried out to arrive at the right-hand expression in equation (2.56). If $I'_{\theta'}$ is an isotropic intensity, \bar{I}' , the integration over θ' can be carried out to give

$$I = \pi \bar{I}' \quad (2.57)$$

Therefore an "equivalent" isotropic intensity will be defined by

$$\begin{aligned} \bar{I}' &= \int_0^{\pi/2} I'_{\theta'} \sin 2\theta' d\theta' \\ &= \frac{I'}{n^2} \int_0^{\pi/2} [1 - r_{\theta}(\theta')] \sin 2\theta' d\theta' \end{aligned} \quad (2.58)$$

From equation (2.54)

$$I'_{\theta'=0} = \frac{I'}{n^2} (1 - \rho_n) \quad (2.59)$$

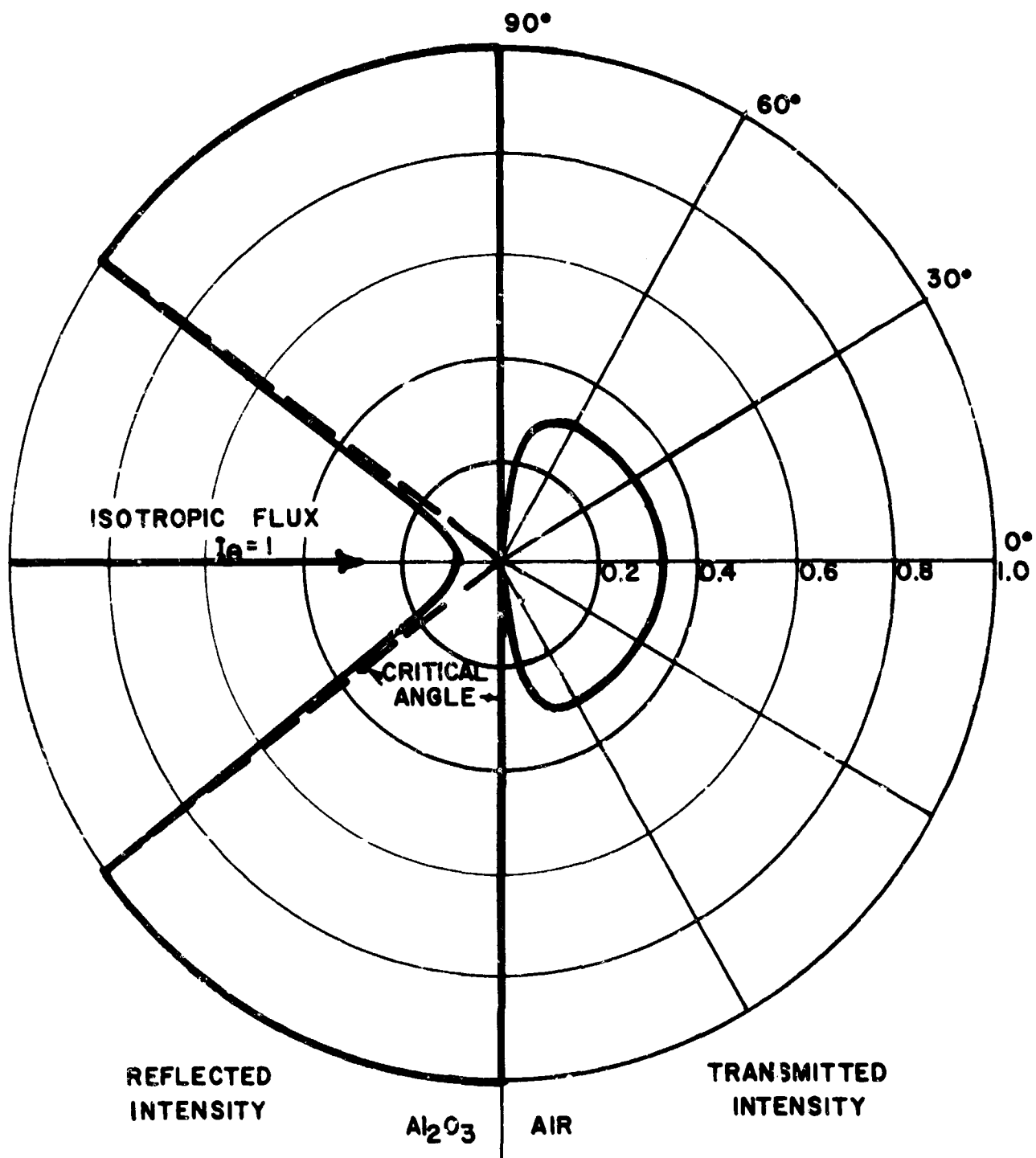


Fig. 2.5 Distribution of Intensity of Reflected and Transmitted Energy of Isotropic Radiation Incident on an Al_2O_3 - Air Interface.

where $\rho_n = r_{\theta'=0}$ is the reflectivity for normal incidence tabulated in Table 2.1.

Hence dividing (2.59) by (2.58)

$$\frac{I'_{\theta'=0}}{\overline{I'}} = \frac{1 - \rho_n}{\pi/2 \int_0^{\pi/2} (1-r_{\theta}) \sin 2\theta' d\theta'} \quad (2.60)$$

The integral in the denominator may be evaluated by changing the variable of integration from θ' to θ according to equation (2.50) and noting that the range of integration will then be from $\theta = 0$ to $\theta = \text{arc.sin}(1/n)$. Thus:

$$\begin{aligned} \int_0^{\pi/2} (1-r_{\theta}) \sin 2\theta' d\theta' &= n^2 \int_0^{\text{arc.sin}(1/n)} (1-r_{\theta}) \sin 2\theta d\theta \\ &= 1 - n^2 \int_0^{\text{arc.sin}(1/n)} r_{\theta} \sin 2\theta d\theta \end{aligned} \quad (2.61)$$

This integral has been evaluated by Walsh,¹⁰ and the result is also recorded by Folweiler³ (p 18). The result is finally

$$\begin{aligned} \int_0^{\pi/2} (1-r_{\theta}) \sin 2\theta' d\theta' &= \frac{1}{2} - \frac{(n-1)(3n+1)}{6(n+1)^2} - \frac{n^2(n^2-1)^2}{(n^2+1)^3} \log \frac{(n-1)}{(n+1)} \\ &\quad + \frac{2n^3(n^2+2n-1)}{(n^2+1)(n^4-1)} - \frac{8n^4(n^4+1)}{(n^2+1)(n^4-1)^2} \log n \\ &= 1 - \rho_0 \end{aligned} \quad (2.62)$$

ρ_o is the reflectivity for diffuse radiation tabulated in Table 2.1.

Hence equation (2.60) may be written

$$\frac{I'_{\theta=0}}{I'} = \frac{1-\rho_n}{1-\rho_o} = \frac{\epsilon_n}{\epsilon_h} \quad (2.63)$$

That is, for isotropic radiation emergent from a surface, the ratio between the normal and hemispherical emissivities is given by the relative value of $(1 - \rho_n)$ and $(1 - \rho_o)$. Values for different refractive indices are given in Table 2.3.

Table 2.3

Ratio of the Normal to Hemispherical Emissivities for Varying
Index of Refraction.

<u>n</u>	<u>$1-\rho_n$</u>	<u>$1-\rho_o$</u>	<u>$\frac{1-\rho_n}{1-\rho_o} = \frac{\epsilon_n}{\epsilon_h}$</u>
1.0	1.000	1.000	1.000
1.2	.992	.955	1.038
1.3	.983	.939	1.047
1.4	.972	.923	1.053
1.5	.960	.908	1.057
1.6	.947	.893	1.060
1.7	.933	.879	1.061
1.8	.918	.866	1.060
1.9	.904	.854	1.058

2.8 Reflectivity for Parallel Radiant Flux at Normal Incidence

If a beam of parallel radiation is incident normally on a slab, it is necessary to extend the calculation for₃ diffuse incident light in Section 3.1 of Folweiler's report. The necessary calculations have been done by Ryde.¹ Some of Ryde's equations are reproduced here to have them available in the notation of this report. It is necessary to define three new scattering coefficients, f , f' , and s' , where these are a forward scattering coefficient for the diffuse radiation and forward and backward scattering coefficients for the parallel radiation respectively.

The equations for the forward and backward diffuse flux are then:

$$\frac{dI}{dx} = f' I_p - (a + s) I + sJ \quad (2.64)$$

$$- \frac{dJ}{dx} = s' I_p - (a + s) J + sI \quad (2.65)$$

and for the parallel flux I_p

$$- \frac{dI_p}{dx} = (a + s' + f') I_p = g' I_p \quad (2.66)$$

The solutions to these equations obtained by Ryde are

$$I_p = e^{-g'x} \quad (2.67)$$

$$I = A(1-\beta_o) e^{\sigma_o x} + B(1+\beta_o) e^{-\sigma_o x} - Ue^{-g'x} \quad (2.68)$$

$$J = A(1+\beta_o) e^{\sigma_o x} + B(1-\beta_o) e^{-\sigma_o x} - V e^{-g'x} \quad (2.69)$$

where

$$U = \frac{[2af' + (s+f')(s'+f')]}{2af + (s'+f')^2} \quad (2.70)$$

$$V = \frac{(s-s')(f'+s')}{[2af + (s'+f')^2]} \quad (2.71)$$

and A, B are to be determined from the appropriate boundary conditions, which are,

$$I_{p_o} = (1 - \rho_n) I_{p_i} \text{ and } I_o = \rho_i J_c \text{ at } x = 0;$$

$$\text{and } J_D = \rho_i I_D \text{ at } x = D.$$

I_{p_i} is the parallel flux incident on the surface of the slab. Also, the assumption is made that $I_p \sim 0$ at $x = d$ or more explicitly that $g \gg \sigma$.

From the second and third boundary conditions we find:

$$A = \frac{-(U-V) \{ (1-\rho_i) - (1+\rho_i) \beta_o \} \exp(-\sigma_o d)}{2 \{ [(1-\rho_i)^2 + (1+\rho_i)^2 \beta_o^2] \sinh \sigma_o d - 2 (1-\rho_i^2) \beta_o \cosh \sigma_o d \}} \quad (2.72)$$

$$B = \frac{(U-V) \{ (1-\rho_i) + (1+\rho_i) \beta_o \} \exp(\sigma_o d)}{2 \{ [(1-\rho_i)^2 + (1+\rho_i)^2 \beta_o^2] \sinh \sigma_o d - 2 (1-\rho_i^2) \beta_o \cosh \sigma_o d \}} \quad (2.73)$$

and using the first boundary condition the reflectivity ρ of the surface is

$$\rho = \rho_n + \frac{J_o}{I_{p_i}} (1-\rho_i) = \rho_n + (1-\rho_n) (1-\rho_i) J_o \quad (2.74)$$

Substituting for J_o

$$\rho = \rho_n + (1-\rho_n) (1-\rho_i)$$

$$\left\{ \frac{(U-V) \{ [(1-\rho_i) - (1+\rho_i)\beta_o^2] \sinh \sigma_o d + 2 \rho_i \beta_o \cosh \sigma_o d \}}{[(1-\rho_i)^2 + (1+\rho_i)^2 \beta_o^2] \sinh \sigma_o d + 2(1-\rho_i^2) \beta_o \cosh \sigma_o d} - V \right\} \quad (2.75)$$

If the incident radiation is diffuse, the reflectivity ρ may be obtained from the above by setting $f' = f$ and $s' = s$, in which case $U = 1$ and $V = 0$; and by replacing ρ_n by ρ_o which gives

$$\rho = \rho_o + (1-\rho_o) (1-\rho_i)$$

$$\left\{ \frac{(1-\rho_i) - (1+\rho_i)\beta_o^2 \sinh \sigma_o d + 2\rho_i \beta_o \cosh \sigma_o d}{[(1-\rho_i)^2 + (1+\rho_i)^2 \beta_o^2] \sinh \sigma_o d + 2(1-\rho_i^2) \beta_o \cosh \sigma_o d} \right\} \quad (2.76)$$

which is the same as Eq. (20) of Folweiler's report.³

3.0 THE HAMAKER APPROXIMATION FOR CONDUCTIVE HEAT FLOW

In the development of the Hamaker equations, an approximation is introduced for the conductive part of the combined heat transfer by conduction and radiation. Measurements of the effective thermal conductivity of polycrystalline alumina at temperatures near 2000°C indicate that the conductive part is still a major contributor, even at this high temperature.⁹ This results from the relatively high conductivity and large scattering coefficients in polycrystalline oxides.

Since the utility of the Hamaker equation depends on the validity of the underlying assumptions, we felt it essential to critically evaluate the nature of these limitations.

The exact equations for describing the transmission of heat by combined conductive and radiative transfer in a homogeneous medium are (for the one-dimensional case and the steady state):

$$k \frac{d^2 T}{dx^2} - 2 a n^2 \sigma' T^4 + a (I + J) = 0 \quad (3.1)$$

$$\frac{dI}{dx} = a n^2 \sigma' T^4 - (a + s) I + sJ \quad (3.2)$$

$$\frac{dJ}{dx} = (a + s) J - sI - a n^2 \sigma' T^4 \quad (3.3)$$

where I and J are the radiant fluxes in the +x and -x direction, T is the absolute temperature, σ' is the Boltzmann constant, n is the refractive index, k is the thermal conductivity, a is the absorption coefficient for diffuse radiation, and s is the back-scattering coefficient for diffuse radiation.

3.1 Direct Numerical Integration

It is convenient to reduce the set of Eq. (3.1), (3.2), and (3.3), to a single second-order equation. Eq. (3.2) and Eq. (3.3) are added and the sum integrated once to give:

$$I + J = - (a + 2s) (Hx + kT) + A \quad (3.4)$$

in which A is a constant of integration and H is the constant heat flux defined by:

$$H = I - J - k \frac{dT}{dx} \quad (3.5)$$

Substituting in Eq. 3.1 we obtain:

$$k \frac{d^2 T}{dx^2} - 2 a n^2 \sigma' T^4 - a (a + 2s) (Hx + kT) + a A = 0 \quad (3.6)$$

For simplicity we will consider the one-dimensional flow of heat by conduction and radiation inside a medium as shown in Fig. 3.1. Once the material constants, k, a, s, and n^2 are specified, there remain four independent initial conditions to be fixed; i.e., T_0 , $(dT/dx)_0$, I_0 , and J_0 . For various values of these initial conditions we have constructed a family of solutions by numerical integration of Eq. (3.6).

The calculation consists of (1) selection of material constants and initial conditions; (2) evaluation of A and H from Eqs. (3.4) and (3.5); (3) calculation of T(x) by numerical integration of Eq. (3.6); (4) calculation of $k (dT/dx)$; and (5) calculation of I(x) and J(x) from the relations:

$$I = \frac{1}{2} [- (a + 2s) (Hx + kT) + a + H + k \left(\frac{dT}{dx} \right)] \quad (3.7)$$

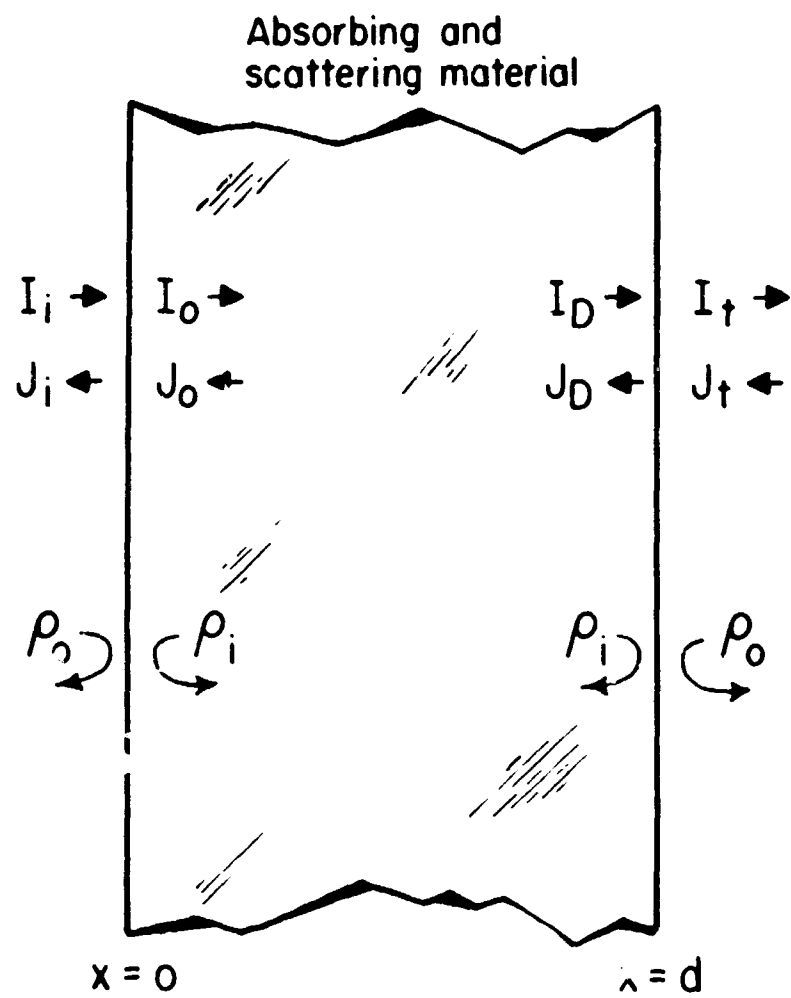


Fig. 3.1 Heat flow by combined radiation and conduction.

$$J = \frac{1}{2} \left[- (a + 2s) (Hx + kT) + C - H - k \left(\frac{dT}{dx} \right) \right] \quad (3.8)$$

3.2 The Hamaker Approximation

Hamaker's approximation consists of replacing the first term in Eq. (3.1) $k (d^2T/dx^2)$ by $k/T_o^3 d^2(T^4)/dx^2$ in which T_o is some average temperature in the material. This replacement makes the set of Eqs. (3.1), (3.2) and (3.3) linear and homogeneous in the quantities I , J , and T^4 so that a solution in closed form can be obtained readily.

3.3 Numerical Evaluations of the Hamaker Solutions

The Hamaker solutions for the radiant fluxes are given in terms of the lumped material constants:

$$b = 4n^2 \sigma' T_o^3 \quad (3.9)$$

$$\sigma = + \sqrt{\frac{2ab}{k} + a(a+2s)} = \sigma_o \sqrt{(1 + \kappa)} \quad (3.10)$$

$$\beta = \sigma / (a + 2s) \quad (3.11)$$

$$\kappa = 2b/k (a + 2s) = 2b\beta/k\sigma \quad (3.12)$$

Then, the radiant energy fluxes and temperature are given by:

$$I = A(1-\beta) e^{\sigma x} + B(1+\beta) e^{-\sigma x} + C(\sigma x - B) + D \quad (3.13)$$

$$J = A(1+\beta) e^{\sigma x} + B(1-\beta) e^{-\sigma x} + C(\sigma x + \beta) + D \quad (3.14)$$

$$E = -A\kappa e^{\sigma x} - B\kappa e^{-\sigma x} + C\sigma x + D \quad (3.15)$$

$$T = T_o + \frac{1}{b} (E - E_o) \quad (3.16)$$

where

$$A = \frac{J_o \sigma (1+\beta) - E_o (2\beta\sigma) - \left(\frac{dE}{dx}_o\right) 2\beta}{4\beta\sigma(\kappa + 1)} \quad (3.17)$$

$$B = \frac{-J_o \sigma (1-\beta) - E_o (2\beta\sigma) + \left(\frac{dE}{dx}_o\right) 2\beta}{4\beta\sigma(\kappa + 1)} \quad (3.18)$$

$$C = \frac{J_o 2\kappa\sigma + \left(\frac{dE}{dx}_o\right) 2\beta}{4\beta\sigma(\kappa + 1)} \quad (3.19)$$

$$D = \frac{J_o 2\beta\kappa\sigma + E_o (4\beta\sigma)}{4\beta\sigma(\kappa + 1)} \quad (3.20)$$

The calculation consists of (1) selection of material constants and initial conditions; (2) evaluation of b , σ , β and κ from Eq. (3.9), (3.10), (3.11), and (3.12); (3) evaluation of A , B , C , and D from Eqs. (3.17), (3.18), (3.19), and (3.20); and (4) calculation of I , J , E , and T for various values of x from Eqs. (3.13), (3.14), (3.15), and (3.16).

3.4 Comparison of the Exact and Hamaker Solutions

A comparison has been made between numerical integration of the exact equation as described in Section 3.1 and numerical evaluation of the Hamaker solution as described in Section 3.3 for the system shown in Fig. 3.1 for a range of initial conditions. Computations were done on an IBM 7090 computer at the Aeronautical Systems Division, Wright-Patterson Air Force Base. For one set of conditions a hand calculation was done in excellent agreement with the computer calculation as shown in Fig. 3.2.

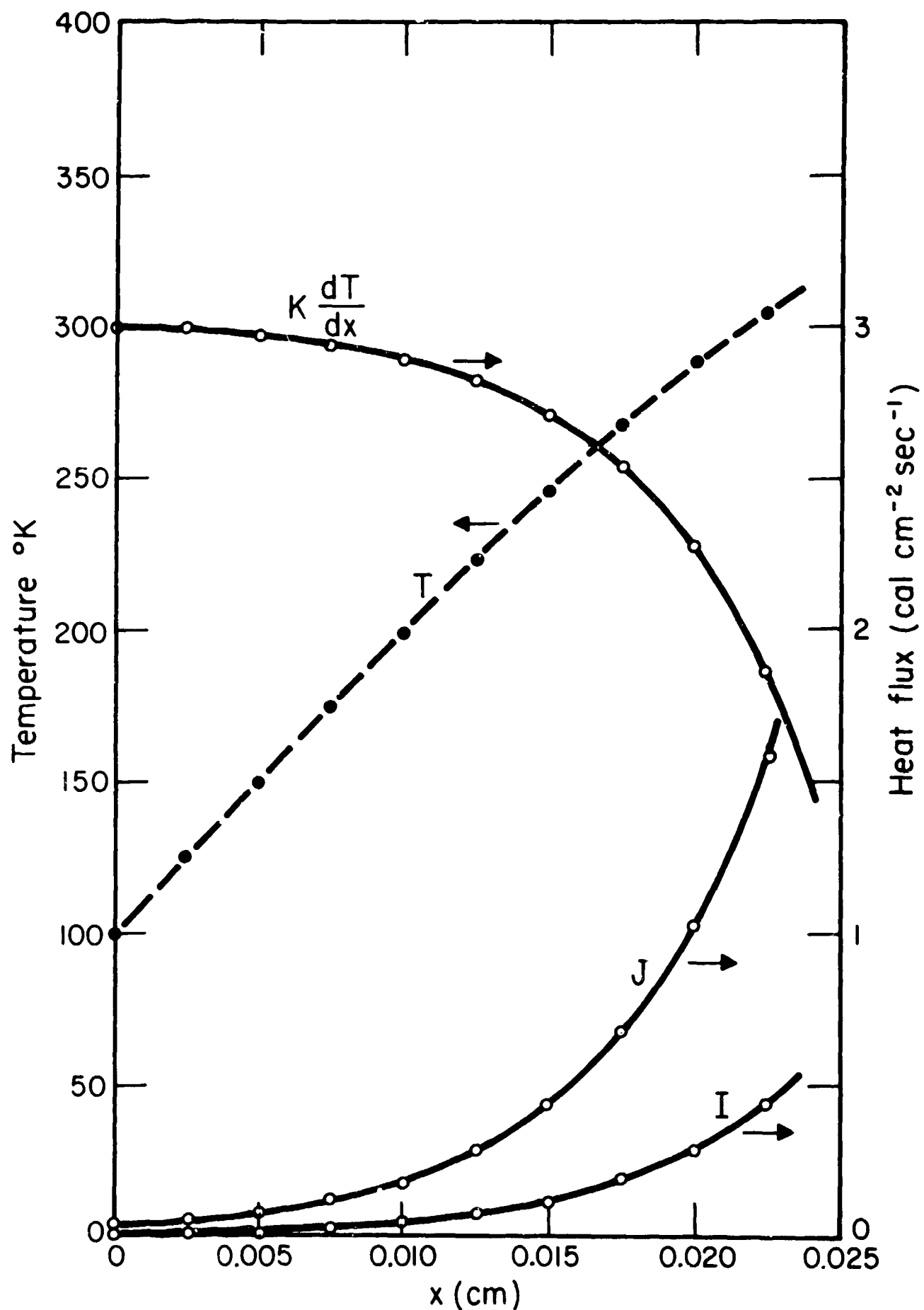


Fig. 3.2 Computer Results (Solid Lines) and Hand Calculated Results (Points) for the Exact Solution of Radiant Energy Heat Transfer.

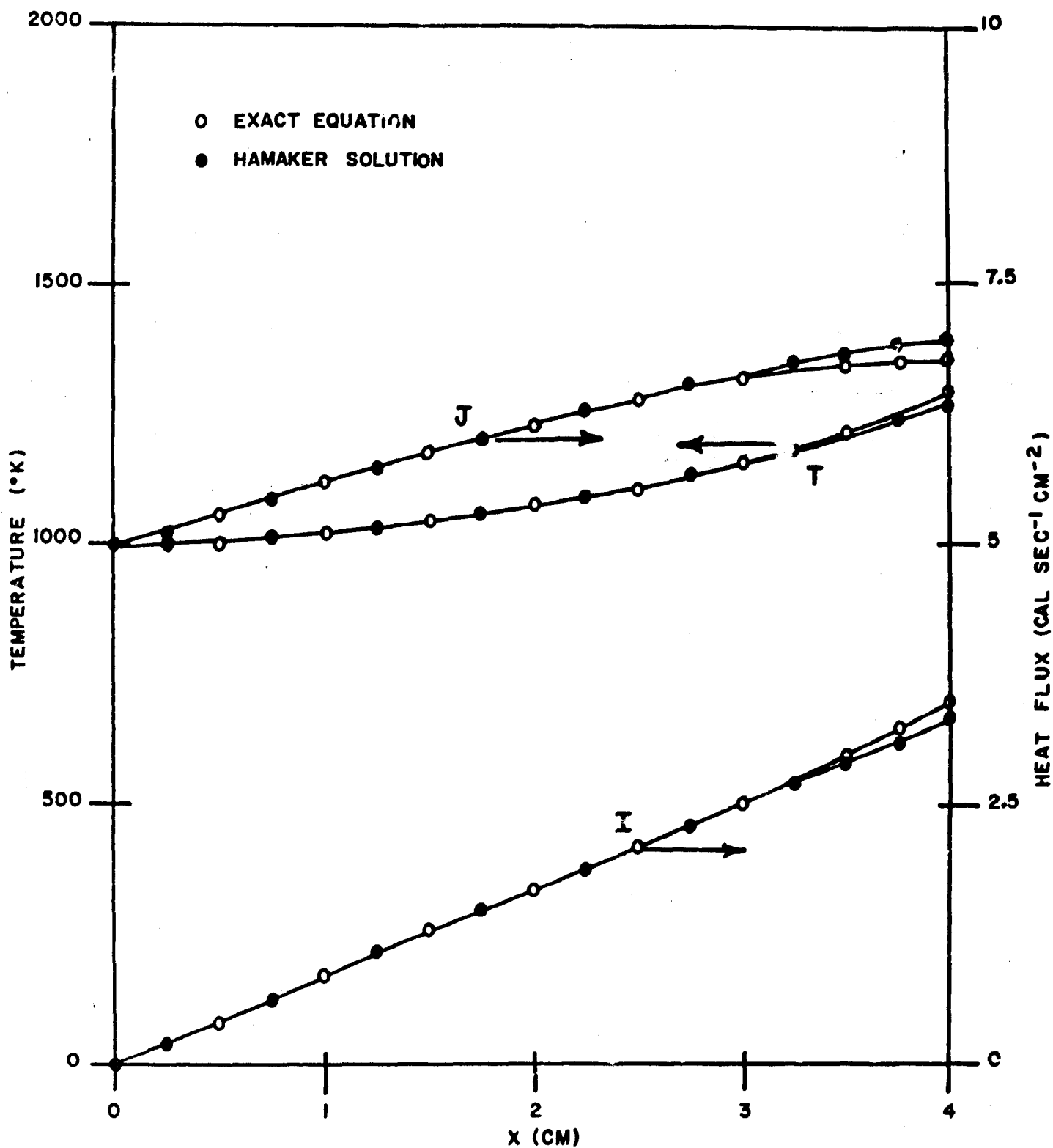


Fig. 3.3 Typical results between exact and Hamaker equations for small values of a and s . $I_0 = 0$; $J_0 = J$; $k = 0.01$; $T_0 = 1,000$; $(\frac{dT}{dx})_0 = 10$; $a = 0.1$; $s = 0.1$; $n^2 = 3$.

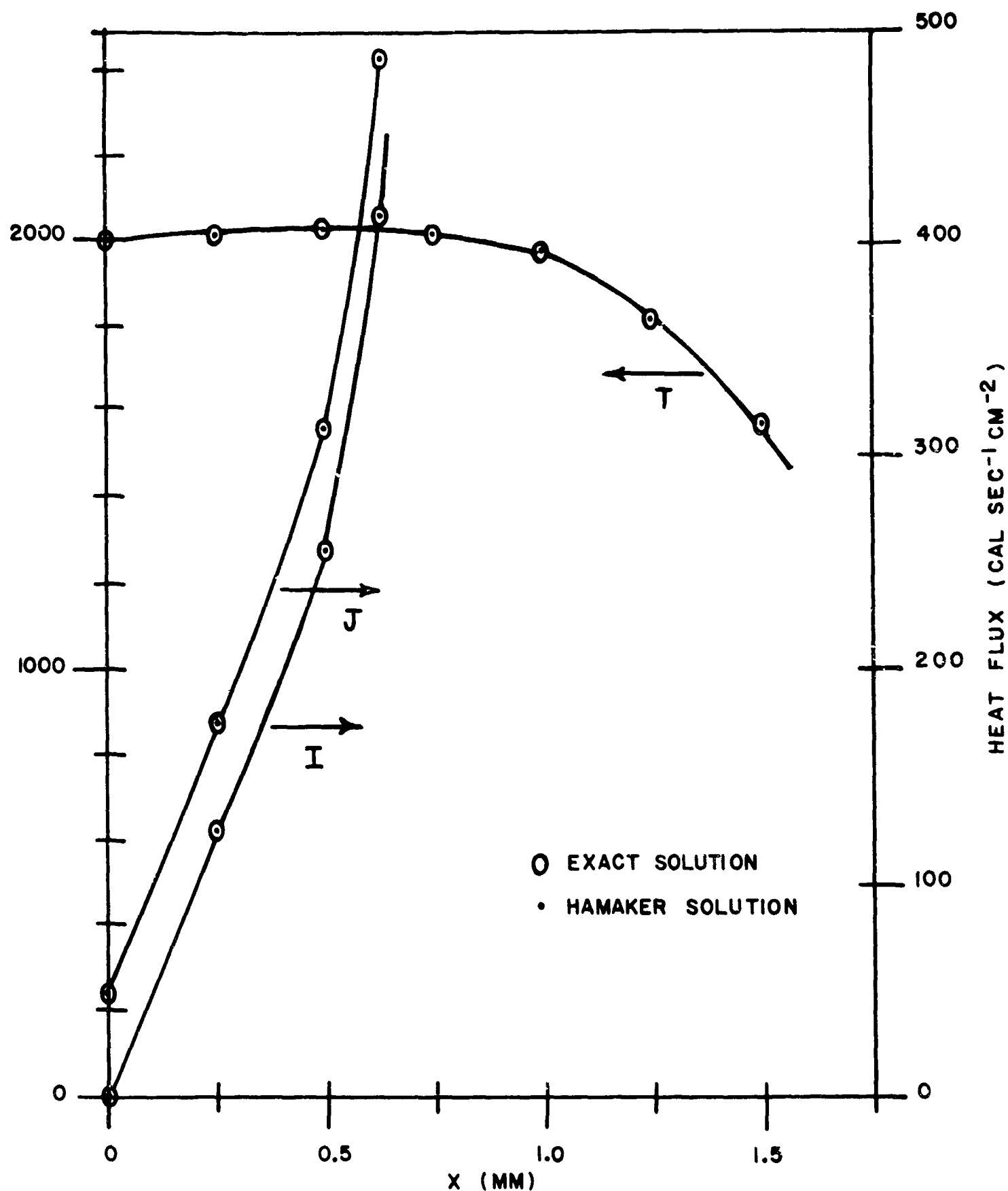


Fig. 3.4 Typical Results of Comparison between Exact and Hamaker Equations in Large Values of a , s and $k(\frac{dT}{dx}_0)$. $I_0 = 0$; $J_0 = 50$; $k = .01$; $T_0 = 2000$; $(\frac{dT}{dx}_0) = 1000$, $a = 1$, $s = 100$, $n^2 = 3$.

Table 3.1 Input Constants and Comparison of Results of Exact and Hamaker Equations
for 20 Conditions

Condi- tion	k	T_o	$\left(\frac{dT}{dx}\right)_o$	I_o	J_o	n^2	a	s	at $x = (a+2s)^{-1}$:			at $x = 2(a+2s)^{-1}$:		
									$\frac{J_H}{J_E}$	$\frac{I_H}{I_E}$	$\frac{T_H}{T_E}$	$\frac{J_H}{J_E}$	$\frac{I_H}{I_E}$	$\frac{T_H}{T_E}$
1	.01	1000	10	0	5	3	0.1	0.1	.987	.986	.993	-	-	-
2	.01	1000	10	0	5	3	1	1	1.000	1.000	1.000	1.000	1.000	1.000
3	.01	1000	10	0	5	3	1	10	1.000	1.000	1.000	1.000	1.000	1.000
4	.01	1000	10	0	5	3	1	100	1.000	1.000	1.000	1.000	1.000	1.000
5	.01	2000	10	0	35	3	1	10	1.000	1.000	1.000	1.000	1.000	1.000
6	.01	2000	10	0	35	3	1	100	1.000	1.000	1.000	1.000	1.000	1.000
7	.01	3000	10	0	125	3	1	10	1.000	1.000	1.000	1.002	0.999	1.000
8	.01	3000	10	0	125	3	1	100	1.000	1.000	1.000	1.000	1.000	1.000
9	.005	2000	100	0	35	3	1	10	1.000	1.000	1.000	1.000	1.000	1.000
10	.005	2000	100	0	35	3	1	100	1.000	1.000	1.000	1.000	1.000	1.000
11	.01	2000	100	0	35	3	1	10	1.000	1.000	1.000	1.000	1.000	1.000
12	.01	2000	100	0	35	3	1	100	1.000	1.000	1.000	1.000	1.000	1.000
13	.05	2000	100	0	35	3	1	10	1.000	1.000	1.000	1.000	1.000	1.000

Table 3.1 (Continued)

Condi- tion	k	T_o	$\left(\frac{dT}{dx}\right)_o$	I_o	J_o	n^2	a	s	at $x = (a+2s)^{-1}$			at $x = 2(a+2s)^{-1}$		
									$\frac{J_H}{J_E}$	$\frac{I_H}{I_E}$	$\frac{T_H}{T_E}$	$\frac{J_H}{J_E}$	$\frac{I_H}{I_E}$	$\frac{T_H}{T_E}$
14	.05	2000	1000	0	35	3	1	100	1.000	1.000	1.000	1.000	1.000	1.000
15	.005	2000	1000	0	50	3	1	10	1.000	1.000	1.000	1.001	.999	1.000
16	.005	2000	1000	0	50	3	1	100	1.000	1.000	1.000	1.000	1.000	1.000
17	.01	2000	1000	0	50	3	1	10	1.000	1.000	1.000	1.000	1.000	1.000
18	.01	2000	1000	0	50	3	1	100	1.000	1.000	1.000	1.000	1.000	1.000
19	.05	2000	1000	0	50	3	1	10	1.000	1.000	1.000	1.000	1.000	1.000
20	.05	2000	1000	0	50	3	1	100	1.000	1.000	1.000	1.000	1.000	1.000

For all calculations I_0 was set equal to zero; physically this corresponds to radiation from the surface into a semi-infinite media with the same index as the test section (no surface reflection) and having perfect transmissivity (no scattering or absorption). Values of J_0 ranged from 0.26-125 cal cm⁻² sec⁻¹, values of $(dT/dx)_0$ ranged from 10-1000°K cm⁻¹ and values of T_0 ranged from 100-3000°K. Material constants were varied in the range: k , .005-05 cal cm⁻¹ sec⁻¹ °K⁻¹; a , 0.1-1.0 cm⁻¹; s , 0.1-100 cm⁻¹; $n^2 = 3$. Some typical results are shown in Fig. 3.3 and Fig. 3.4. Tabulated input data and a comparison of results between the Exact and Hamaker solutions are given in Table 3.1.

The depth of the sample contributing to the emissivity characteristics is that part that is optically "near" the surface. Thus, even though calculations were carried out to a greater sample depth in most cases, we have compared results at $x = (a + 2s)^{-1}$ and $x = 2(a + 2s)^{-1}$ in Table 3.1. As shown there for the entire range of conditions where a and s are greater than unity, agreement between the exact and the Hamaker equations was within 0.1%. For the calculation with $a = 0.1$ and $s = 0.1$, agreement was within about 1% at $x = (a + 2s)^{-1}$. Considering that values of thermal conductivity up to the highest observed for oxides (0.05 for BeO) and values of temperature gradients up to 1000°/cm were evaluated, the results clearly show that the Hamaker equation is a satisfactory approximation for any thermal conditions likely to be encountered for heat transfer problems related to oxide materials.

4.0 EXTENSION OF THE HAMAKER EQUATIONS

The Hamaker equations for radiant energy fluxes and energy distribution are:

$$I = A(1-\beta)e^{\sigma x} + B(1+\beta)e^{-\sigma x} + C(\sigma x - \beta) + D \quad (4.1)$$

$$J = A(1+\beta)e^{\sigma x} + B(1-\beta)e^{-\sigma x} + C(\sigma x + \beta) + D \quad (4.2)$$

$$E = -A\kappa e^{\sigma x} - B\kappa e^{-\sigma x} + C\sigma x + D \quad (4.3)$$

$$\text{where } \sigma = \sqrt{\frac{2ab}{k} + a(a+2s)} = \sigma_0 \sqrt{1+\kappa} \quad (4.4)$$

$$\text{and } \beta = \sigma/(a+2s) \quad (4.5)$$

$$\text{and } \kappa = 2b/k(a+2s) = 2b\beta/k\sigma \quad (4.6)$$

We have recalculated the values of the constants A, B, C and D for boundary conditions when I_0 , J_0 , $(\frac{dE}{dx})_0$ and E_0 are given at $x = 0$ without the limitation that $I_0 = 0$. We find:

$$A = \frac{-2\beta \left(\frac{dE}{dx}\right)_0 - \sigma(1-\beta)I_0 + \sigma(1+\beta)J_0 - 2\beta\sigma E_0}{4\beta\sigma(1+\kappa)} \quad (4.7)$$

$$B = \frac{2\beta \left(\frac{dE}{dx}\right)_0 + \sigma(1+\beta)I_0 - \sigma(1-\beta)J_0 - 2\beta\sigma E_0}{4\beta\sigma(1+\kappa)} \quad (4.8)$$

$$C = \frac{4\beta \left(\frac{dE}{dx} \right)_0 - 2\kappa\sigma I_0 + 2\kappa\sigma J_0}{4\beta\sigma (1+\kappa)} \quad (4.9)$$

$$D = \frac{2\sigma\beta\kappa(I_0 + J_0) + 4\beta\sigma E_0}{4\beta\sigma (1+\kappa)} \quad (4.10)$$

We have also calculated values for the boundary conditions $I_0 = 0$ at $x = 0$, T_0 (or E_0) at $x = 0$, T_d or E_d at $x = d$, and a constant for the heat flux H , where

$$H = I_0 - J_0 - \frac{k}{b} \frac{dE}{dx}_0 \quad (4.11)$$

Inserting the boundary conditions in equations 4.1 and 4.2,

$$I_0 = A(1-\beta) + B(1+\beta) - C\beta + D \quad (4.12)$$

$$J_0 = A(1+\beta) + B(1-\beta) + C\beta + D \quad (4.13)$$

From 4.3

$$\frac{dE}{dx} = -A\kappa\sigma e^{\sigma x} + B\kappa\sigma e^{-\sigma x} + C\sigma \quad (4.14)$$

$$H = I_0 - J_0 - \frac{k}{b} (-A\kappa\sigma + B\kappa\sigma + C\sigma) \quad (4.15)$$

From 4.12, 4.13, and 4.14,

$$H = \left(\frac{k}{b} \kappa\sigma - 2\beta \right) A + \left(2\beta - \frac{k}{b} \kappa\sigma \right) B - \left(\frac{k}{b} \sigma + 2\beta \right) C \quad (4.16)$$

also, at $x = 0$

$$E_0 = \sigma' n^2 T_0^4 = -A\kappa - Bk + D \quad (4.17)$$

while at $x = d$,

$$E_d = -3\sigma' n^2 T_0^4 + 4\sigma' n^2 T_0^3 T_d = -A\kappa e^{\sigma d} - B\kappa e^{-\sigma d} + C\sigma d + D \quad (4.18)$$

Then, equations 4.12, 4.15, 4.17 and 4.18 constitute the boundary conditions and a set of four simultaneous linear algebraic equations in A, B, C and D:

$$I_0 = (1-\beta) A + (1+\beta) B - \beta C + D \quad (4.12)$$

$$E_0 = -\kappa A - \kappa B + D \quad (4.17)$$

$$E_d = -\kappa e^{\sigma d} A - \kappa e^{-\sigma d} B + d\sigma C + D \quad (4.18)$$

$$H = \left(\frac{k}{b} \kappa \sigma - 2\beta\right) A - \left(\frac{k}{b} \kappa \sigma - 2\beta\right) B - \left(\frac{k}{b} \sigma + 2\beta\right) C \quad (4.16)$$

Solving these equations for A, B, C, and D, we obtain,
for $I_0 = 0$,

$$A = \frac{1}{\Delta} \left\{ \frac{2\beta(1+\kappa)}{\kappa} [-E_0(1+\beta+\kappa e^{-\sigma d}) + E_d(1+\beta+\kappa)] \right. \\ \left. + H[d\sigma(1+\beta+\kappa) + \kappa\beta(1-e^{-\sigma d})] \right\} \quad (4.19)$$

$$B = \frac{1}{\Delta} \left\{ \frac{2\beta(1+\kappa)}{\kappa} [E_c (1-\beta+\kappa e^{\sigma D}) - E_d (1-\beta+\kappa)] \right. \\ \left. - H[d\sigma(1-\beta+\kappa) + \kappa\beta(1-e^{\sigma d})] \right\} \quad (4.20)$$

$$C = \frac{1}{\Delta} H\kappa \{ (1-\beta+\kappa)(1-e^{-\sigma d}) - (1+\beta+\kappa)(1-3^{\sigma d}) \} \quad (4.21)$$

$$F = E_o + \frac{1}{\Delta} \kappa \left\{ \frac{4\beta(1+\kappa)}{\kappa} [E_o (\kappa \sinh \sigma d - \beta) + \beta E_d] \right. \\ \left. + H [2\beta(d\sigma + \kappa \sinh \sigma d)] \right\} \quad (4.22)$$

$$= E_o + \kappa(A+B)$$

where

$$\Delta \equiv (1+\kappa) 4 \beta \{ \beta(1-\cosh \sigma d) - (1+\kappa) \sinh \sigma d \} \quad (4.23)$$

The suitability of the Hamaker solution for this kind of boundary conditions is one of its strong features. In contrast, there is no obvious way in which the exact solution can be utilized except when the four necessary boundary conditions are all given at one point.

5.0 SAMPLE PREPARATION AND CHARACTERIZATION

Samples of several materials were prepared for emissivity measurements. The materials and their sources and average particle size were:

<u>Material</u>	<u>Powder</u>	<u>Particle Size</u>	<u>Fabricator</u>
Al_2O_3	Linde A	0.3 micron	Lexington Laboratories
MgO		1 micron	Avco RAD
SrTiO_3	TAM C.P.	-325 mesh	Lexington Laboratories
SiO_2			Avco RAD & Corning
CaF_2	Baker CP		Lexington Laboratories

Initial attempts were made to prepare all of the materials except SiO_2 by isostatic pressing and sintering. This procedure resulted in complete success with the Al_2O_3 , partial success with SrTiO_3 and CaF_2 . Other methods were used to prepare the remaining samples.

Measurements of density were performed by both point count on a polished section (counting the pores falling under the intersections of a uniform grid) and by immersion in xylene. Xylene was chosen because of its low surface tension relative to the solids to be immersed. Weights of the sample were taken (a) dry, (b) immersed and (c) saturated but not immersed. The measurements have been generally reproducible within 1%.

Pore radius was computed from the measured average length of line intersected by the pores. The relation used to obtain

the value of the pore radius was

$$\bar{r} = \frac{3}{4} \bar{\ell} \quad (5.1)$$

where \bar{r} = average pore radius and $\bar{\ell}$ = average length of line intercepted by pore.

5.1 Al_2O_3

5.1.1 Preparation

Five samples of Al_2O_3 were prepared by isostatic pressing at 8000 psi. An addition of 20 wt % distilled water was made to aid green strength. The samples, as pressed, were disks approximately 5 inches in diameter by 2 inches in thickness; extra material was allowed in order that the surface be characteristic of the bulk material.

Firing was done in air using a furnace with a program controller. Variations of time and temperature were used to control the density. Where necessary samples were fired more than once to adjust the density to a desired value.

5.1.2 Characterization

The measured density of the Al_2O_3 samples is as follows (% of theoretical):

<u>Sample</u>	<u>Point Count</u>	<u>Immersion</u>	<u>Figure</u>
Al-1	88.1	95.8	5.1
Al-2	77.4	86.0	5.2
Al-3	96.4	95.8	5.3
Al-4	85.5	90.0	5.4
Al-6	77.0	87.6	5.5

Greater discrepancies were observed between the less dense samples for two reasons: (1) low density and fine grain size

made preparation of polished sections extremely difficult and
(2) immersion measurement problems increase with low density.

Pore radius measurements yielded values for the various Al_2O_3 samples as follows:

<u>Sample</u>	<u>Pore Radius (microns)</u>
Al-1	2.50
Al-2	1.69
Al-3	1.77
Al-4	1.17
Al-6	1.68

5.2 MgO

5.2.1 Preparation

Controlled hot pressing, performed at Avco RAD, was done in graphite dies. A measured charge was placed in the die, then pressure and temperature increased until a pre-determined ram travel was observed.

Machining of the finished samples was done dry using diamond tools. Special care was observed with the lower density sample because of the tendency of fine particle MgO to react with atmospheric CO_2 and H_2O .

5.2.2 Characterization

Density measurements provided the following values (% of theoretical):

<u>Sample</u>	<u>Point Count</u>	<u>Immersion</u>	<u>Figure</u>
Mg-3	88.0	94.0	5.6
Mg-5	90.0	97.5	5.7

The fine grain size of the less dense material generated exceptional difficulty in producing a polished section that could be photographed.

The average pore radius observed for each sample was

<u>Sample</u>	<u>Pore Radius (microns)</u>
Mg-3	2.13
Mg-5	1.78

5.3 SrTiO_3

5.3.1 Preparation

Isostatic pressing and sintering was used to obtain a high density sample (Sr-1); slip casting was used to obtain a lower density sample. Both samples were fired in air using slow heating rates.

Samples were machined wet using diamond tools.

5.3.2 Characterization

Sample densities were observed as follows (% of theoretical):

<u>Sample</u>	<u>Point Count</u>	<u>Immersion</u>	<u>Figure</u>
Sr-1	92.9	98.7	5.8
Sr-2 (cast)	* 63.	64.	5.9

Average pore radius for the two samples was

<u>Sample</u>	<u>Pore Radius (microns)</u>
Sr-1	2.47
Sr-2 (cast)	3.00

5.4 SiO_2

5.4.1 Preparation

Two sample preparation techniques were used; a higher density sample was hot pressed by Avco, and two of lower densities were slip cast by Corning, and fired to a terminal

* Because of the difficulty in polishing Sr-2 (cast), the value .63 was used; it was obtained both on a xylene immersion measurement and by mechanical measurement of the weight and volume of a regular cylinder of the material.

density. In both cases, the maximum temperature was low enough to cause little or no devitrification.

The hot pressed sample, however, was observed to be over 99% dense. As a result, it was not considered a semi-transparent material with pores as scattering centers, but a nearly transparent glass. The two samples from Corning were measured and the resulting data used.

Calculated values for emissivity of fused silica were computed on the basis of the microstructure of the Corning samples.

Machining was done wet with diamond tools.

5.4.2 Characterization

Observed values of density were (% of theoretical):

<u>Sample</u>	<u>Point Count</u>	<u>Immersion</u>	<u>Figure</u>
FS-3	65.9	84.3	5.10
FS-5	71.7	87.0	5.11
FS-7	100.0	99.5	5.12

Average pore radius for the two samples was:

<u>Sample</u>	<u>Average Pore Radius (microns)</u>
FS-3	1.28
FS-5	3.06

5.5 CaF_2

5.5.1 Preparation

Efforts at preparing a satisfactory sample were thwarted by adsorption of water on the surface of the powder; during firing the water reacted to form a complex hydrate and finally CaO . Attempts at preparing the powder and firing the slug in an atmosphere of dry, CO_2 -free nitrogen were partially successful. Two samples, free of CaO , were prepared; but failed in machining.

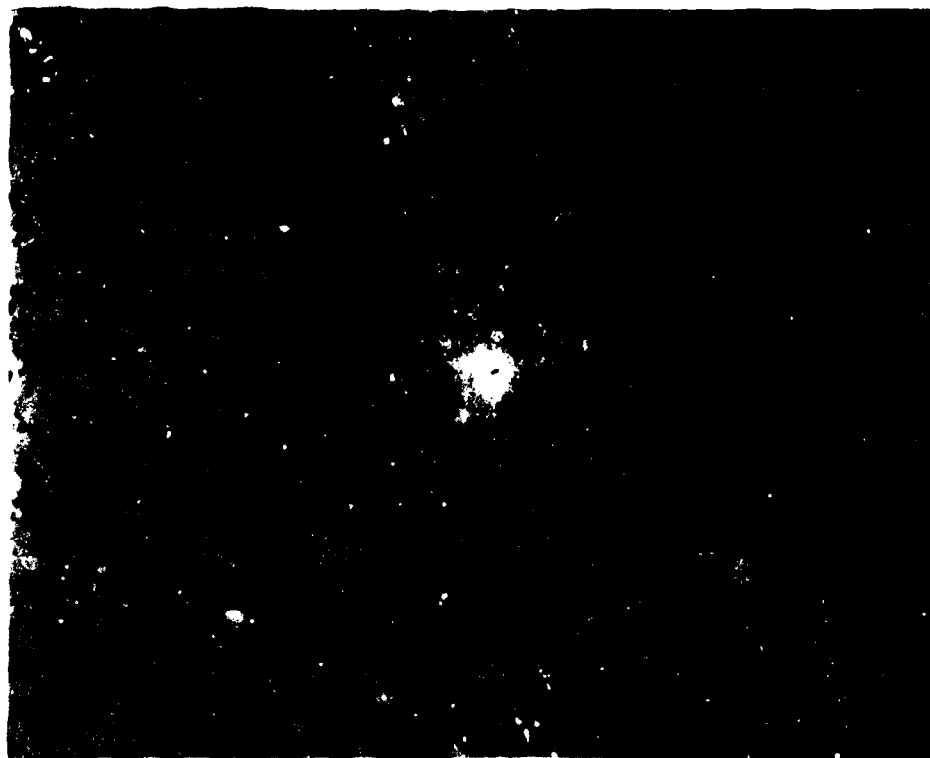


Fig. 5.1 Al-1 532X. Point Count Density = 88.1% of Theoretical Density.

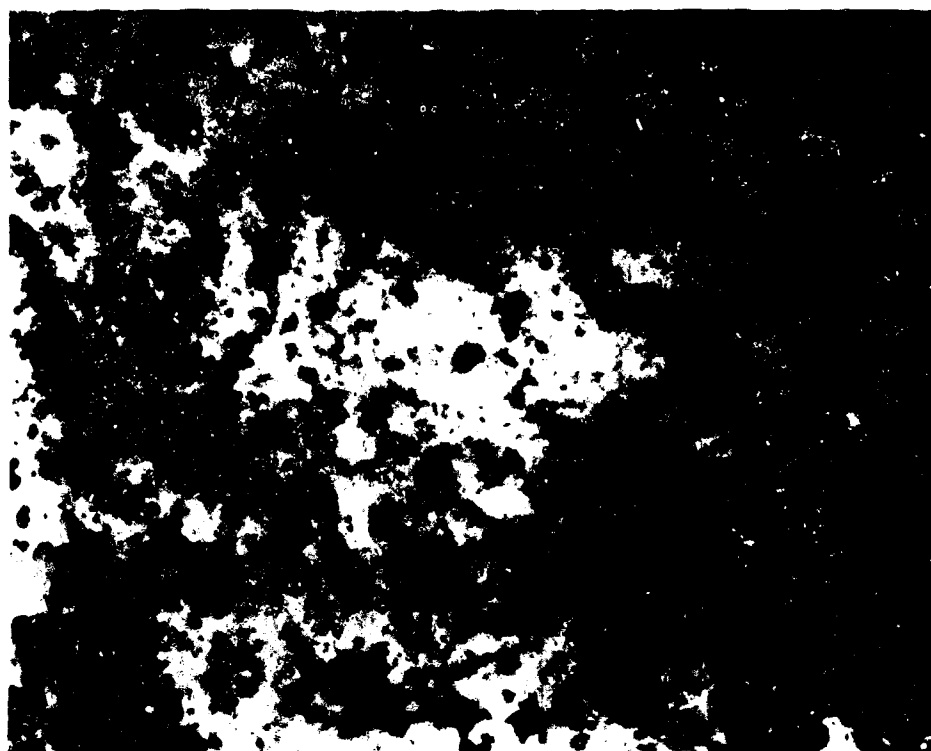


Fig. 5.2 Al-2 532X. Point Count Density = 77.4% of Theoretical Density.

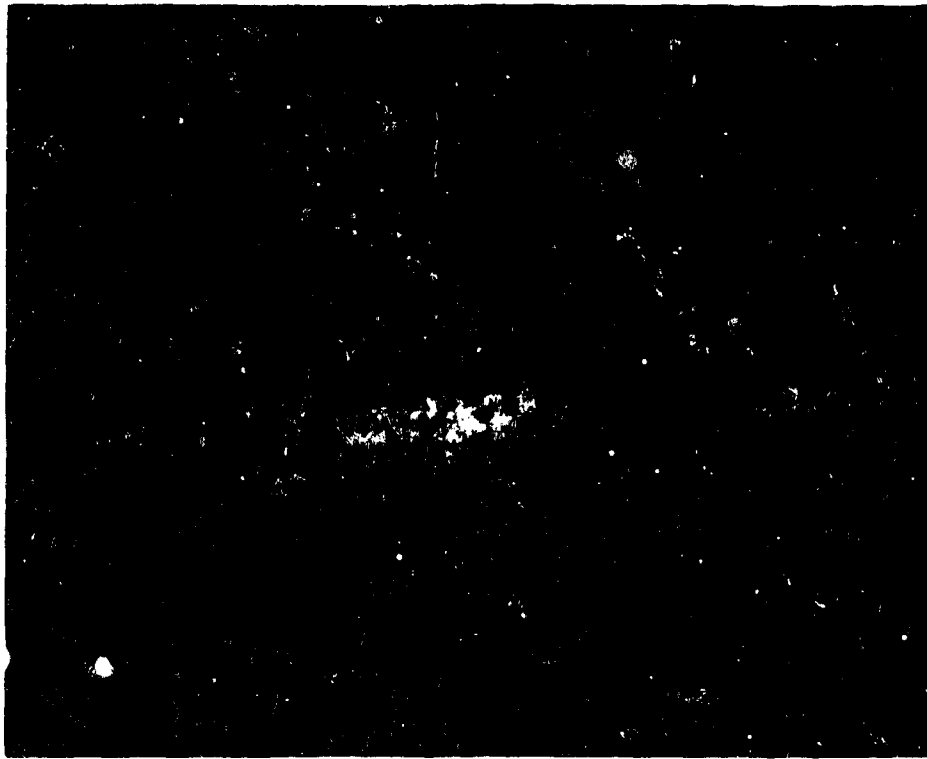


Fig. 5.3 Al-3 532X. Point Count Density = 96.4% of Theoretical Density.

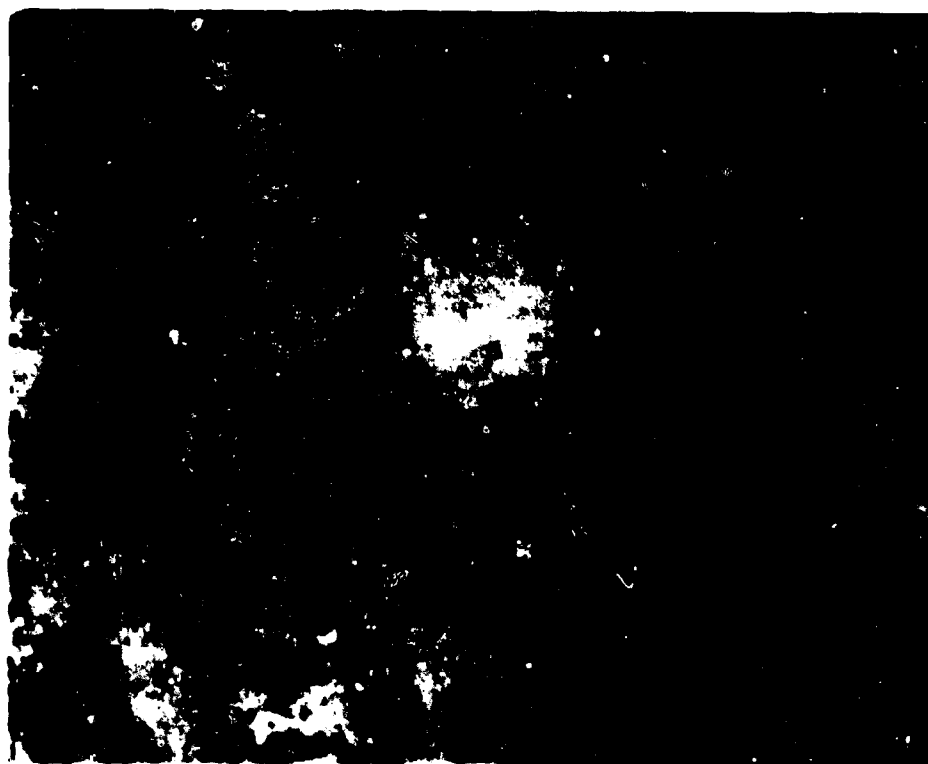


Fig. 5.4 Al-4 532X. Point Count Density = 85.5% of Density.

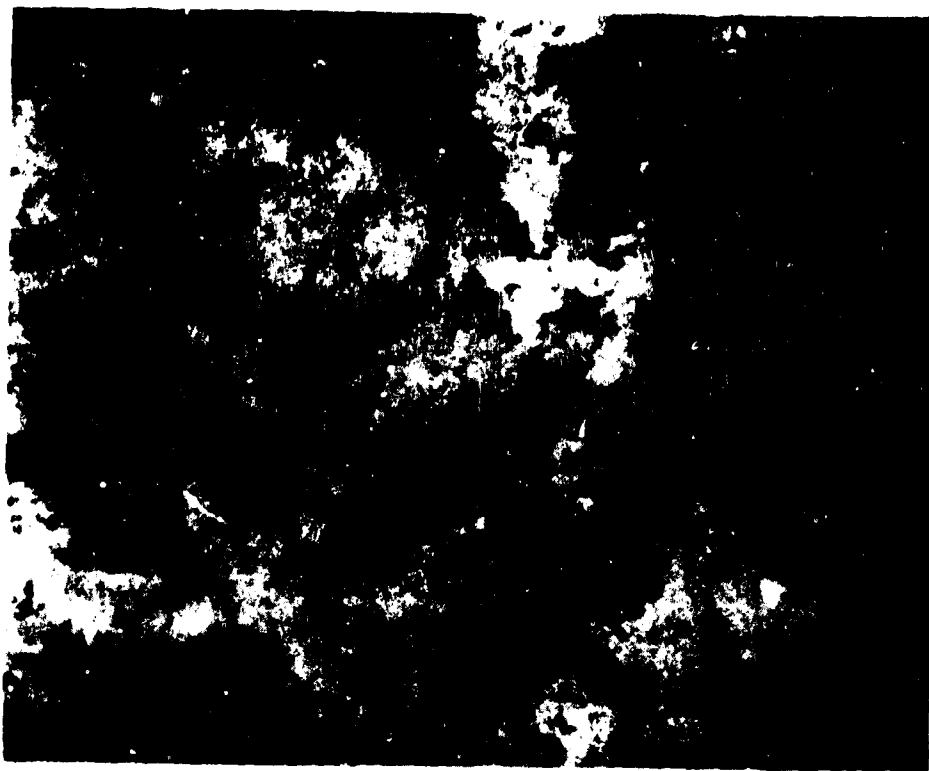


Fig. 5.5 Al-6 532X. Point Count Density = 77.0% of Theoretical Density.

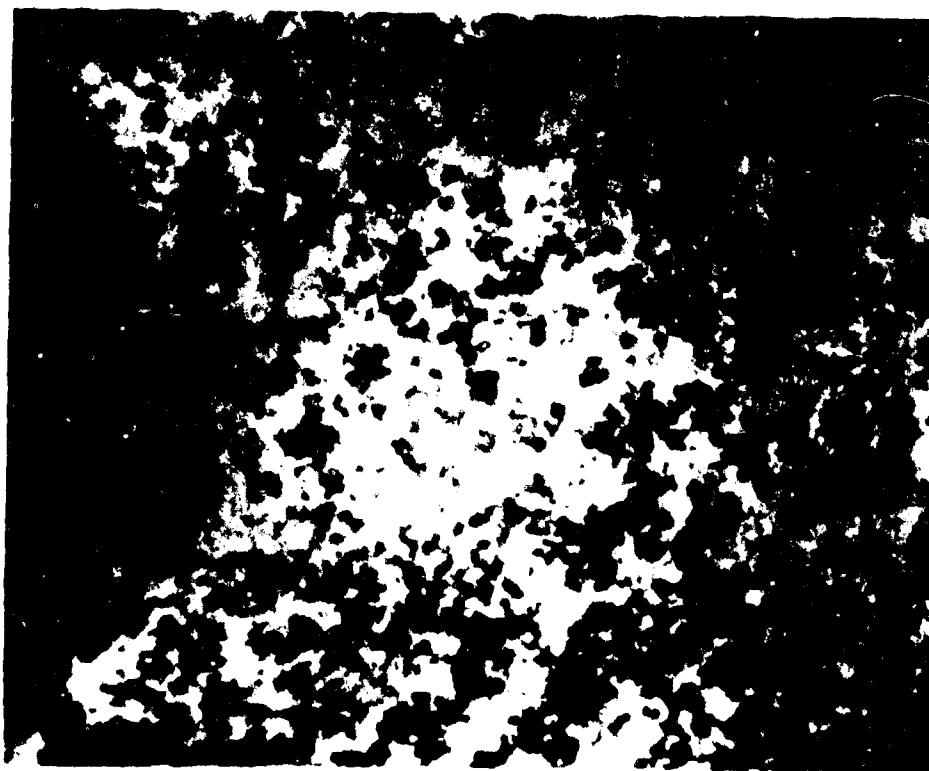


Fig. 5.6 Mg-3 532X. Point Count Density = 88.0% of Theoretical Density.

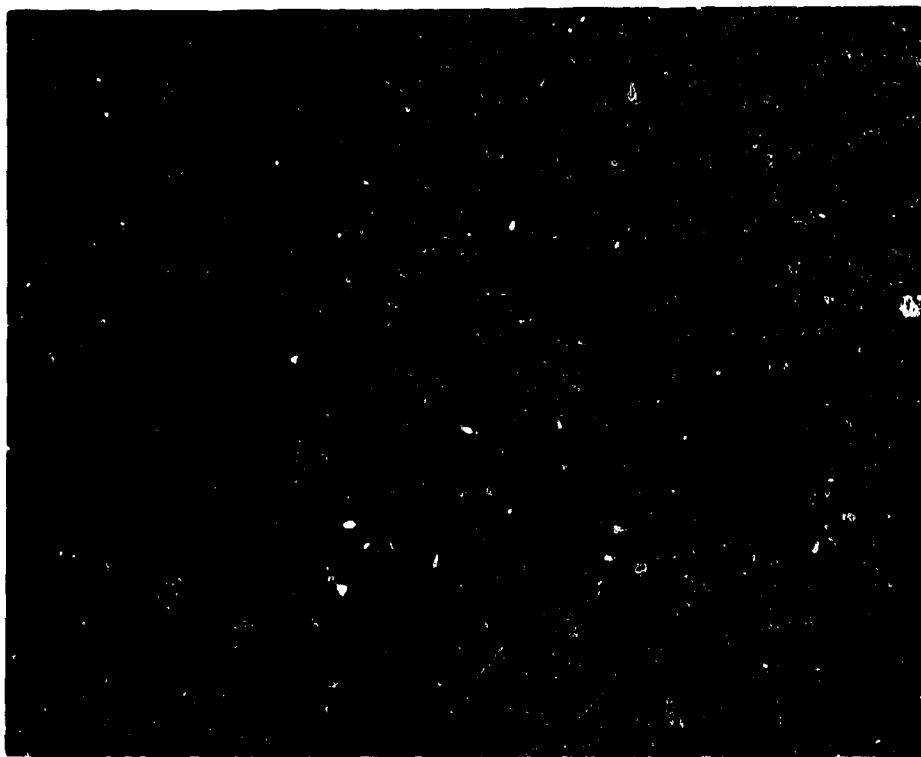


Fig. 5.7 Mg-5 532X. Point Count Density = 90.0% of Theoretical Density.

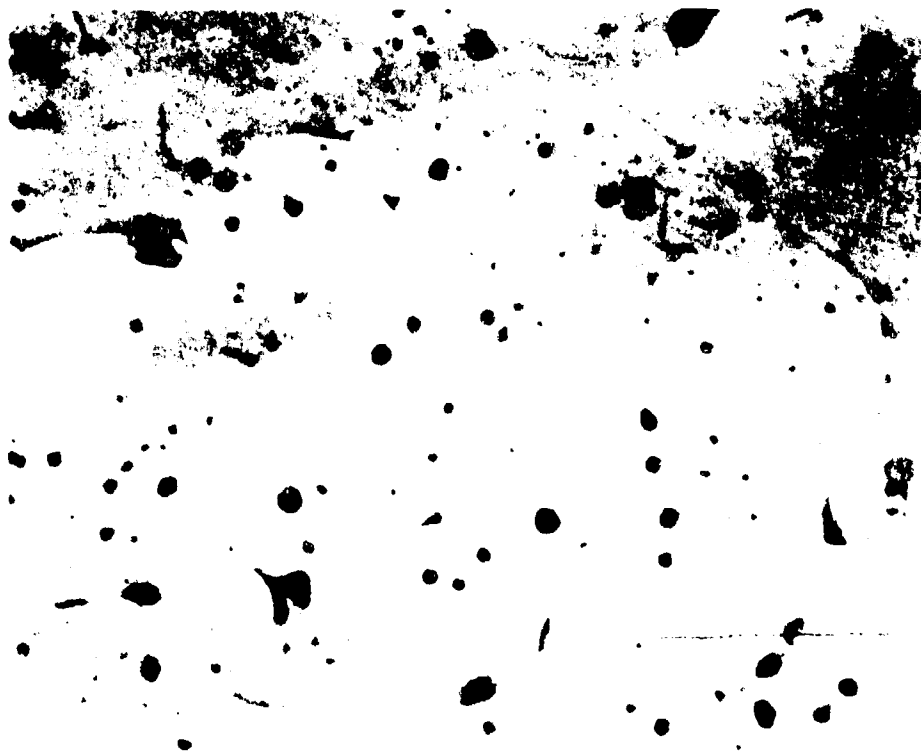


Fig. 5.8 Sr-1 1064X. Point Count Density = 92.9% of Theoretical Density.

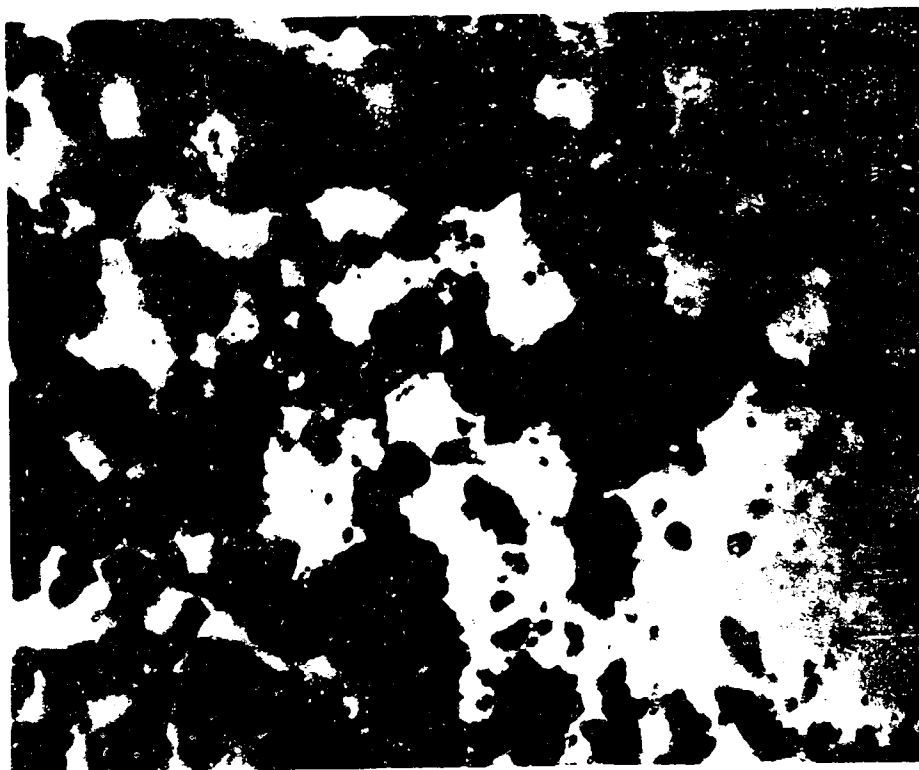


Fig. 5.9 Sr-2 1064X. Immersion Density = 63% of Theoretical Density.

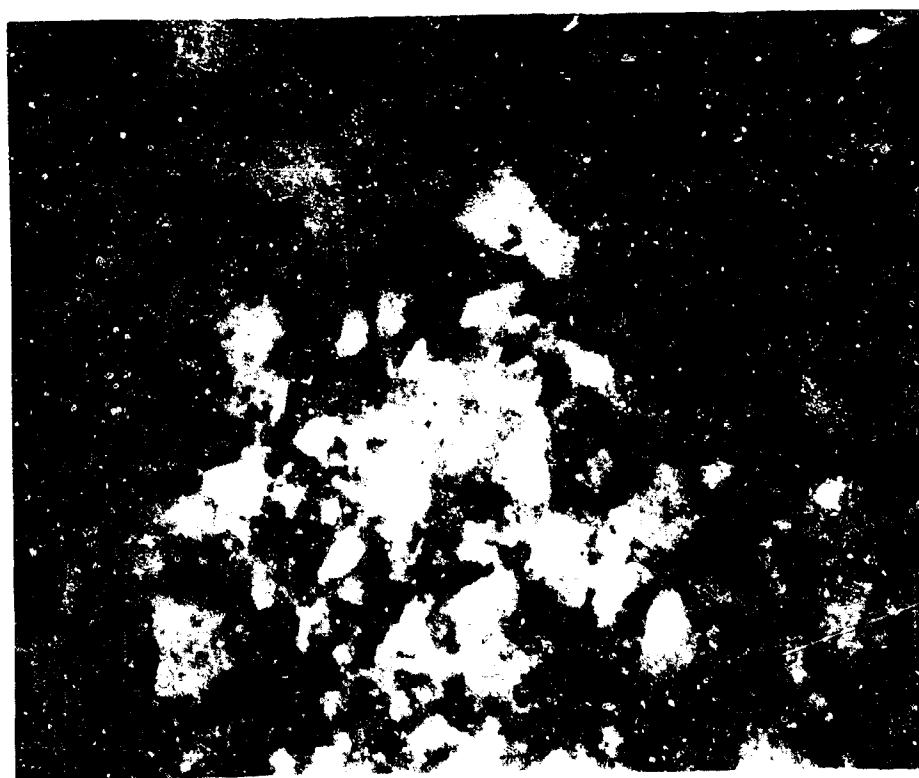


Fig. 5.10 FS-3 532X. Point Count Density = 65.9% of Theoretical Density.



Fig. 5.11 FS-5 532X. Point Count Density = 71.7% of Theoretical Density.



Fig. 5.12 FS-7 532X. Polarized Incident Light Shows Crystalline Phase. Immersion Density = 99.5% of Theoretical Density.

6.0 SINGLE CRYSTAL ABSORPTIVITY

Transmission of various single crystals was measured to determine the absorptivity, α , as a function of wavelength and temperature. Measurements were made at temperatures up to 1200°C and at wavelengths as long as 15 microns or as permitted by material properties. In the calculation of α , correction was made for surface reflections by the following formula:

$$\frac{I}{I_0} = (1-\rho)^2 e^{-\alpha t} \quad (6.1)$$

where

- I = transmitted energy
- I_0 = incident energy
- t = thickness of sample (cm)
- e = natural logarithm base
- ρ = surface reflectivity

The value of ρ at a particular wavelength may be calculated if the index of refraction, n_λ , is known at that wavelength. The relation is

$$\rho = \frac{(1-n_\lambda)^2}{(1+n_\lambda)^2} \quad (6.2)$$

6.1 Experimental Technique

A small high temperature furnace with a rectangular cross-section was used to heat the samples. Special optics are required for use with the spectrophotometer. Details have been presented previously.⁽³⁾

6.2 Samples

Single crystals of Al_2O_3 , MgO , SrTiO_3 and CaF_2 , were

measured as well as samples of SiO_2 glass. Isothermal emissivity measurements were done on most of the same group of materials. Sources of the materials were

Al_2O_3	Linde
MgO	Semi-Elements
SiO_2	A. D. Jones Optical
SrTiO_3	TAM Division National Lead
CaF_2	Semi-Elements

6.3 Results

Figures 6.1 through 6.5 show absorption coefficients as a function of temperature and wavelength.

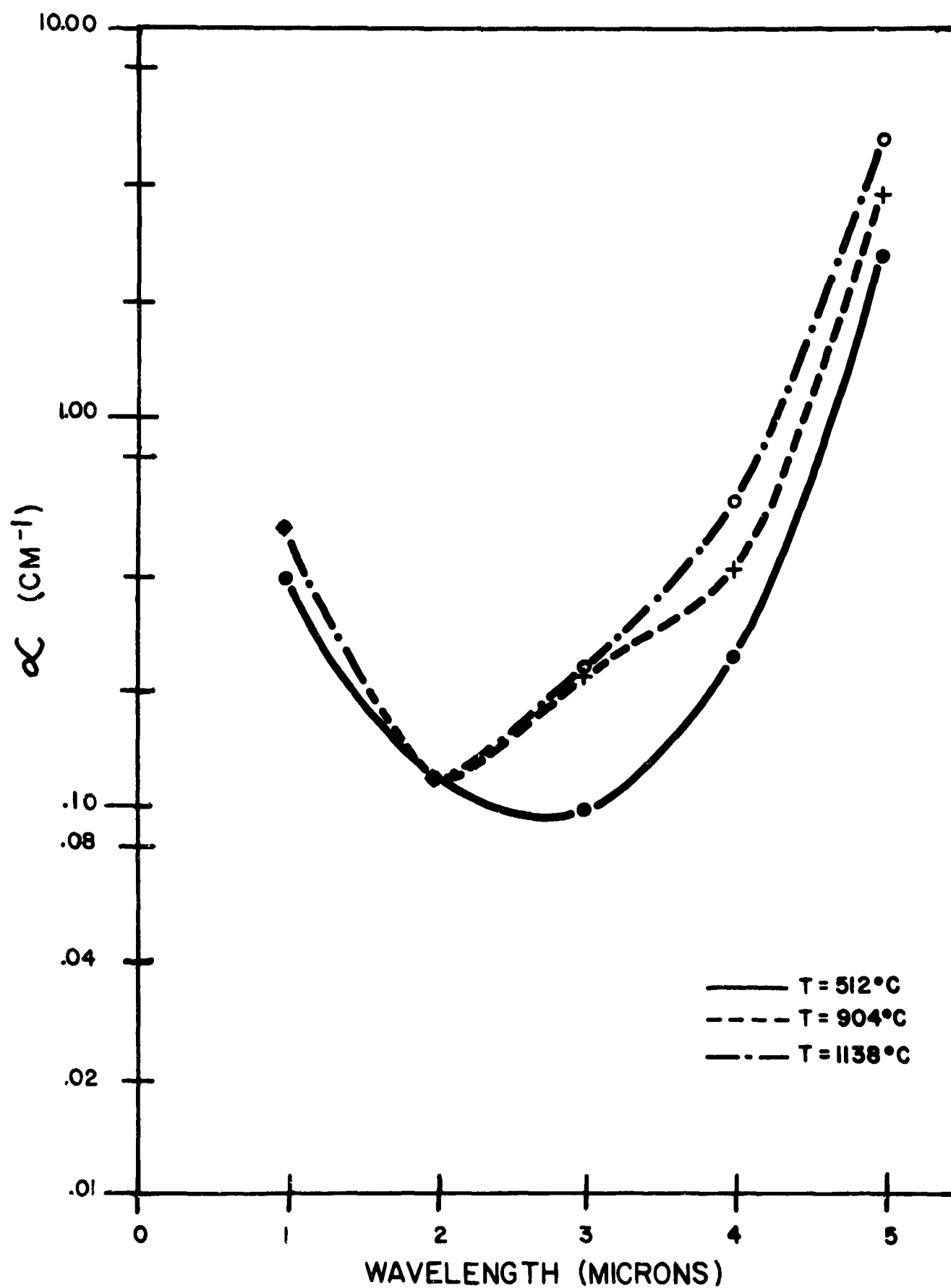


Fig. 6.1 Absorption coefficient of Single Crystal Al_2O_3 .

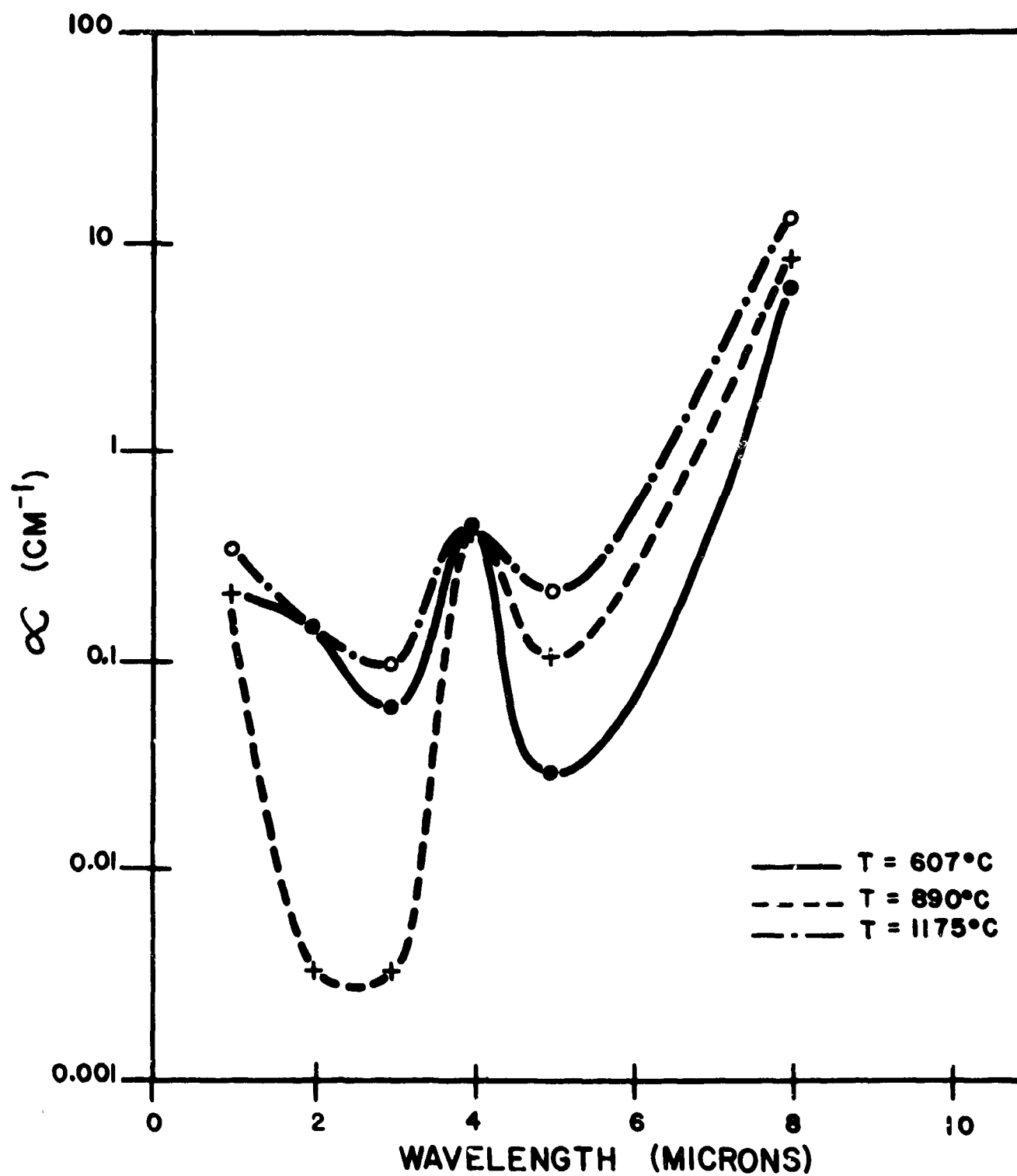


Fig. 6.2 Absorption coefficient of Single Crystal MgO.

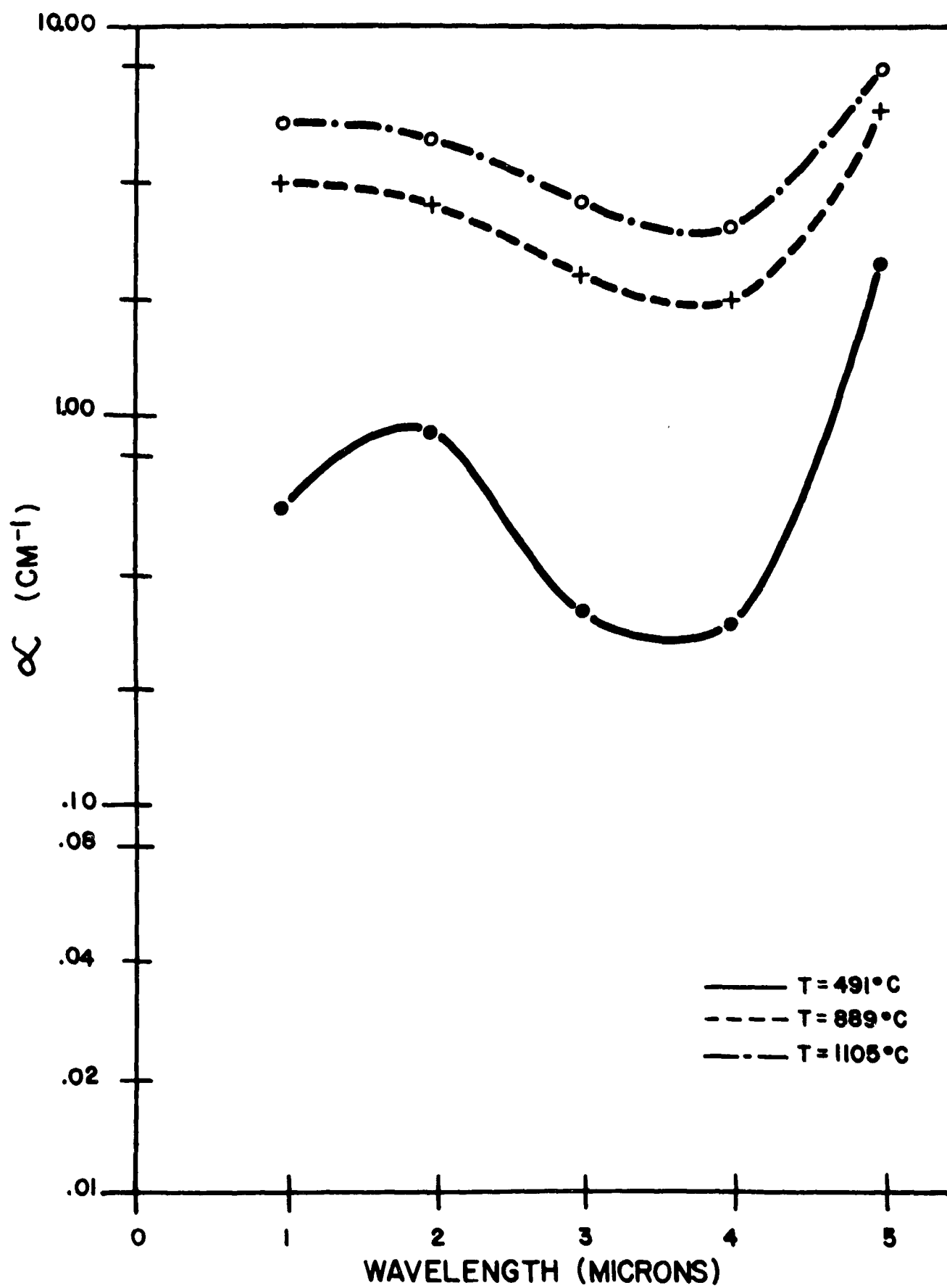


Fig. 6.3 Absorption coefficient of Single Crystal SrTiO_3 .

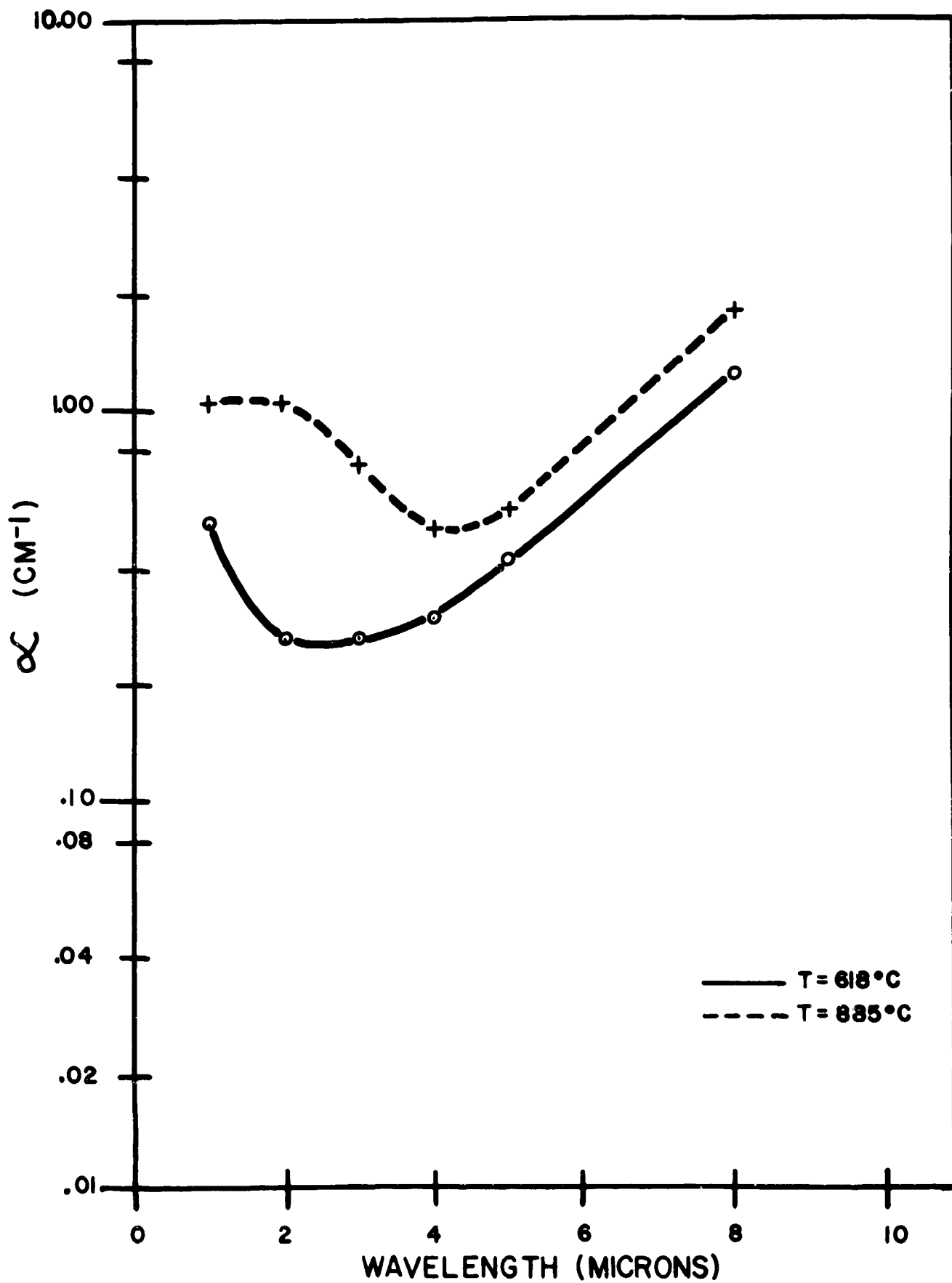


Fig. 6.4 Absorption coefficient of Single Crystal CaF_2 .

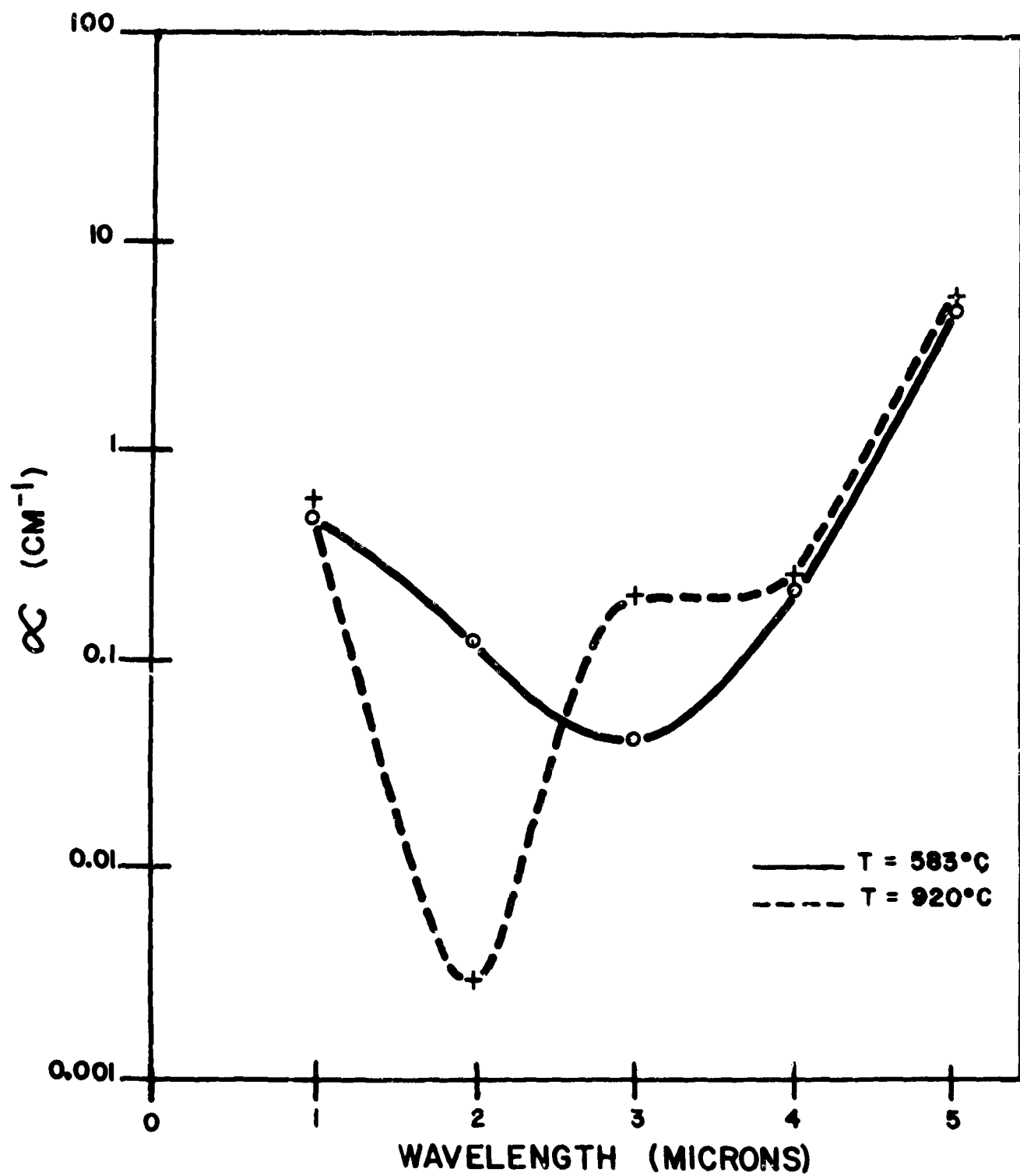


Fig. 6.5 Absorption coefficient of SiO_2 Glass.

7.0 ISOTHERMAL EMISSIVITY AND CALIBRATION MEASUREMENTS

Measurements of isothermal emissivity were made on well characterized samples and a check of the effectiveness of the blackbody source was performed using a special blackbody as a reference.

7.1 Isothermal Emissivity

7.1.1 Measurements

Measurements of emissivity were performed using the same equipment as previously described.³ Basically it consists of two disk shaped samples adjoining each other within a furnace with optical access through a water cooled port. Transfer optics provide two beams to a recording spectrophotometer, one the reference beam from a cylindrical groove between the samples that provides a blackbody; the other from the cylindrical surface of the sample as it rotates past the port. Thus the spectrophotometer records emissivity of the sample directly with no correction for temperature.

7.1.2 Results of isothermal measurements

Figures 7.1 through 7.29 present the results of measurements. Figures 7.30 through 7.36 present comparison calculations made during the present contract and measurements made on the previous contract.

7.2 Blackbody Calibration

Emissivity measurements made by direct comparison of the radiation emitted from a sample surface and a reference blackbody can only be as good as the blackbody reference. Two general requirements must be met: (1) the blackbody must have an emissivity near unity and (2) the blackbody must be at the same temperature as the sample.

In the Lexington Laboratories design, these requirements are met with a rotating wedge which is actually part of the sample and thus is at the same temperature. The slot surface is blackened with a silicon carbide coating having an emissivity near 0.9 over most of the wavelengths of interest and above 0.7 at all wavelength. With this surface, the geometry is such as to give an emissivity above 0.995 over all wavelengths of interest.

7.2.1 Apparatus

A blackbody furnace has been constructed and the essential details of the unit are shown in Fig. 7.37. The unit is based on a design used at the National Bureau of Standards.¹¹ By their calculations, the calculated emissivity was 0.999, although the actual emissivity is probably somewhat less.

The only changes in the NBS design are: (a) the use of Kanthal A-1 instead of Pt-20%Rh, (b) machining the core instead of casting, and (c) use of air cooling instead of water.

The furnace is introduced to the optical system of the spectrophotometer by rotating one of the mirrors in the external entrance optics (See Fig. 7.38). By rotating this mirror, the system may be adjusted to the proper energy source without introducing any auxiliary mirrors but still using the full complement of mirrors. Introduction of auxiliary mirrors, exclusion of any mirrors, or changes in reflection angle would tend to introduce differences in the beam path. Such differences would prevent useful calibration.

7.2.2 Calculations

In emissivity measurements and comparison tests using a separate blackbody, it is essential to have well-defined

temperatures. The energy emitted by a blackbody as a function of temperature is given by Planck's radiation law:

$$\psi_{\lambda, T} = c_1 \lambda^{-5} \frac{1}{e^{c_2/\lambda T} - 1} \quad (7.1)$$

For considering the effect of small temperature differences, Wien's radiation law is a good approximation,

$$\psi_{\lambda, T} = \lambda^{-5} e^{-c_2/\lambda T} \quad (7.2)$$

Then, if the reference blackbody and the sample are at slightly different temperatures,

$$\frac{\psi_{\lambda, T_1}}{\psi_{\lambda, T_2}} = \frac{c_1 \lambda^{-5} e^{-c_2/\lambda T_1}}{c_1 \lambda^{-5} e^{-c_2/\lambda T_2}} \quad (7.3)$$

or,

$$\frac{\psi_{\lambda, T_1}}{\psi_{\lambda, T_2}} = e^{c_2/\lambda} \left[\frac{1}{T_1} - \frac{1}{T_2} \right] \quad (7.4)$$

and,

$$\ln \frac{\psi_{\lambda, T_1}}{\psi_{\lambda, T_2}} = \frac{c_2}{\lambda} \left[\frac{1}{T_1} - \frac{1}{T_2} \right] \quad (7.5)$$

where $c_2 = 1.435$ when λ is given in centimeters and T in $^{\circ}K$

7.2.3 Results and discussion

Inspection of equation 7.5 shows that the effect of temperature differences is particularly important at the shorter wavelengths. That is, at 1000°C , a difference in temperature of 5° between the standard and the reference leads to a difference of energy emitted by the blackbody of about 5% at 1 micron and only .5% at ten microns. Thus, in comparing blackbodies, measurements at the shorter wavelengths are of particular significance.

Results of one set of measurements are illustrated in Fig. 7.39. The blackbody furnace was at a temperature of 1008°C and stabilized; the rotating slot was stabilized at a temperature of 10°C . The ratio of measured energy emitted was within less than 1% of the calculated value over the entire range of wavelengths and no systematic deviation was observed, except perhaps at the shorter wavelengths where small variations in temperature assume greater significance. We interpret these results as confirming the blackness of our rotating wedge configuration, and illustrating the need for precise temperature measurement and control when an exterior blackbody source is used.

In the case of these measurements we also confirmed previous observations of the need for care in alignment, particularly at the longer wavelengths when the spectrometer slit is wide open. A measurement under similar conditions for those shown in Fig. 7.39 is illustrated in Fig. 7.40. Here the agreement between blackbody furnace and rotating wedge is good at the shorter wavelengths, but decreased energy is obtained from the rotating wedge at wavelengths above about 11 microns because of misalignment.

Thus the present results confirm our previous experience that experimental measurements are reproducible within $\pm 1\%$. However, the possibility of minor misalignment, changes in optical path, or other minor variations, leads us to conservatively claim no more than a maximum possible error of up to 5% for any individual measurement.

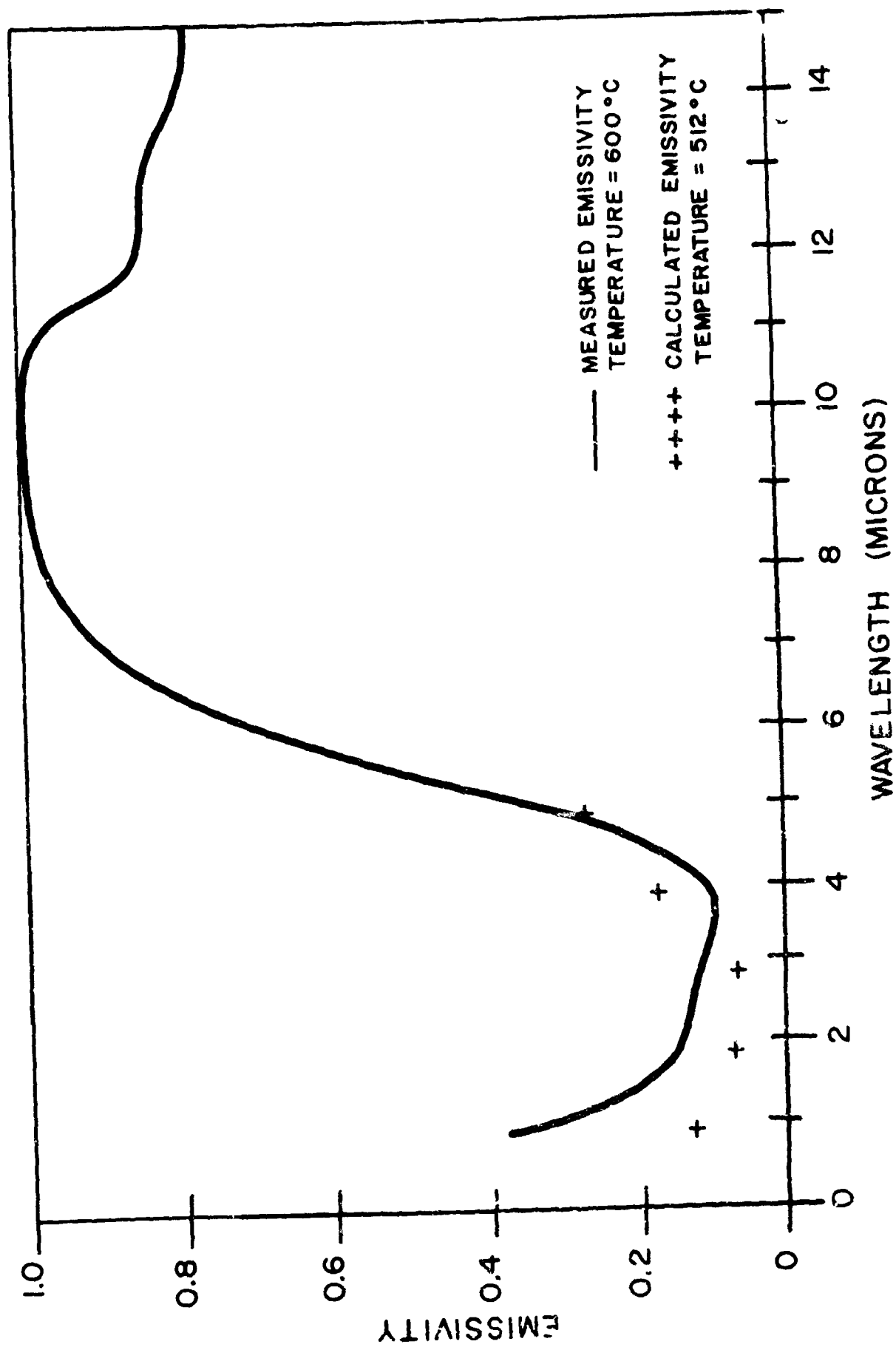


Fig. 7.1 Measured vs. Calculated Emissivity of Al_2O_3 (A-I) 600°C.

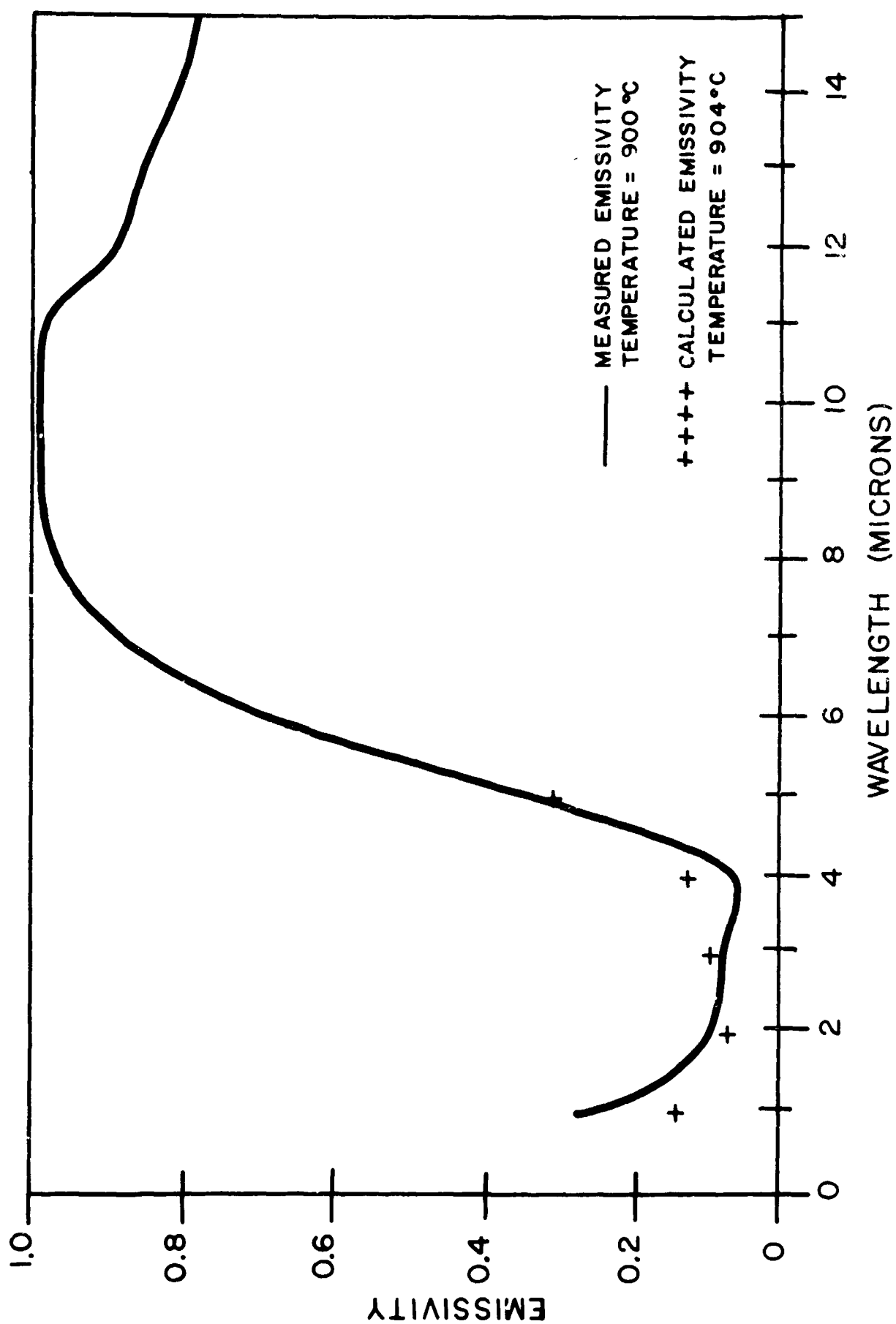


Fig. 7.2 Measured vs. Calculated Emissivity of Al_2O_3 (A2-1) 900°C .

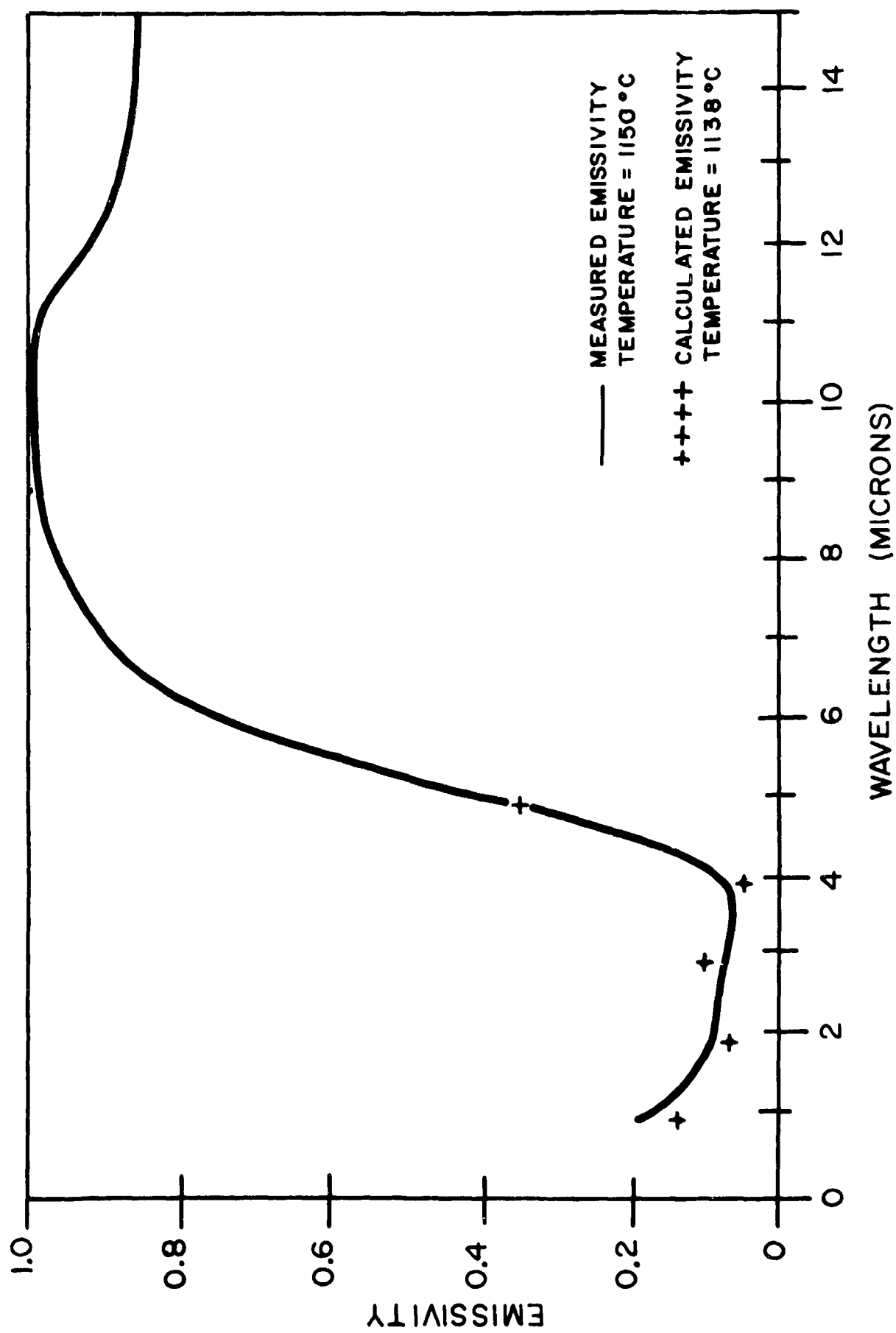


Fig. 7.3 Measured vs. Calculated Emissivity of Al_2O_3 (Al-1) 1150°C .

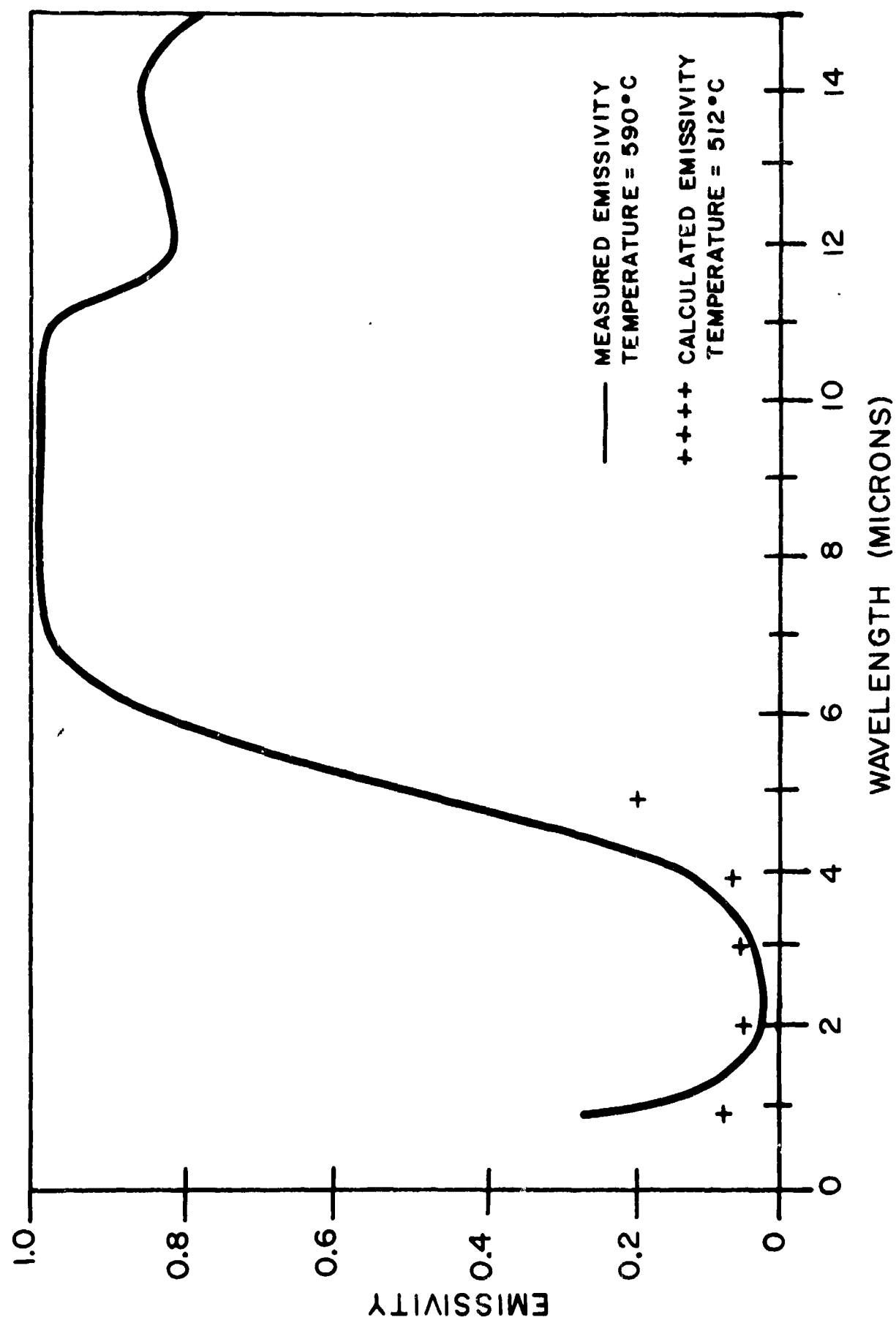


Fig. 7.4 Measured vs. Calculated Emissivity of Al_2O_3 (Al-2) 590°C.

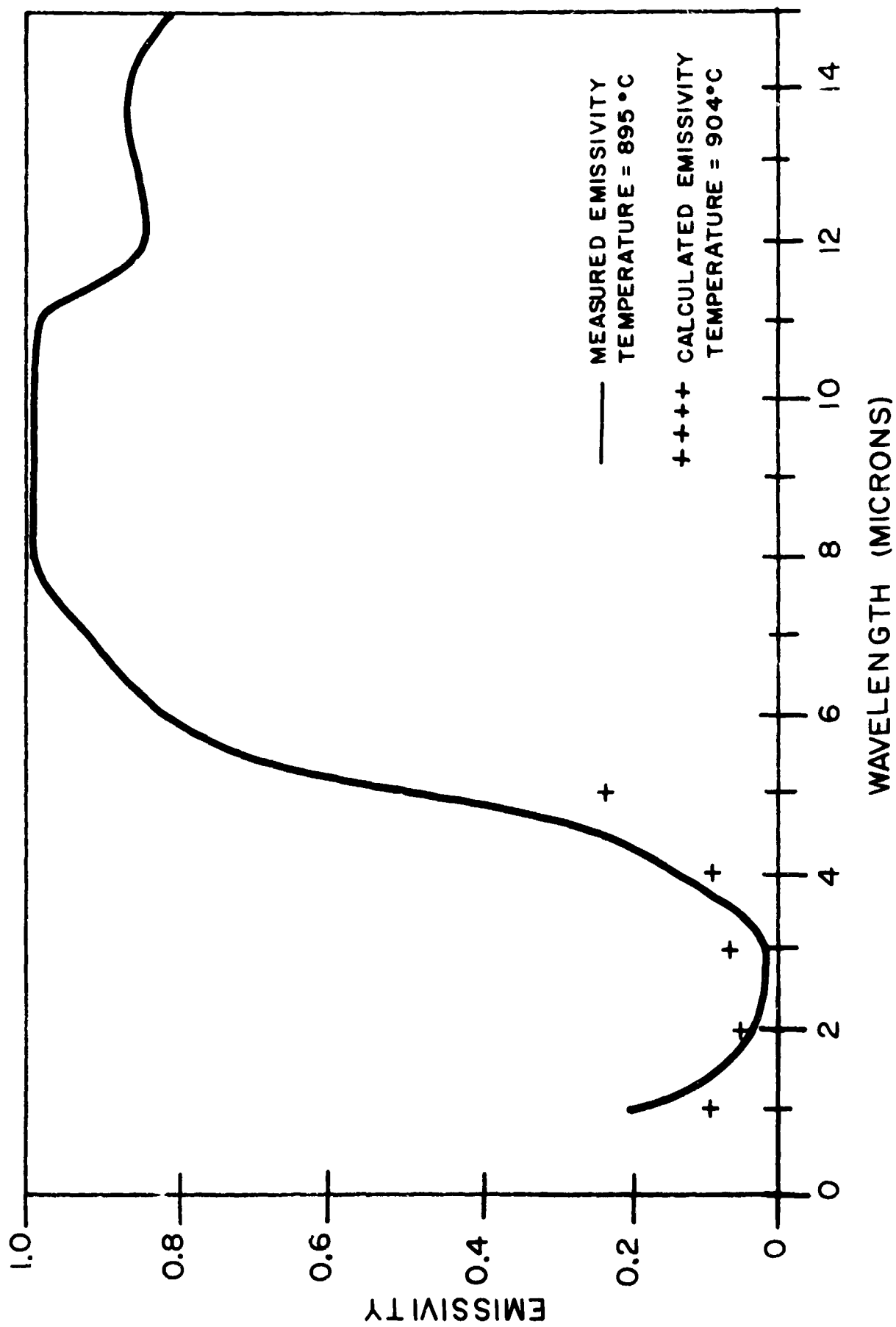


Fig. 7.5 Measured vs. Calculated Emissivity of Al_2O_3 (Al-2) $895^{\circ}C$.

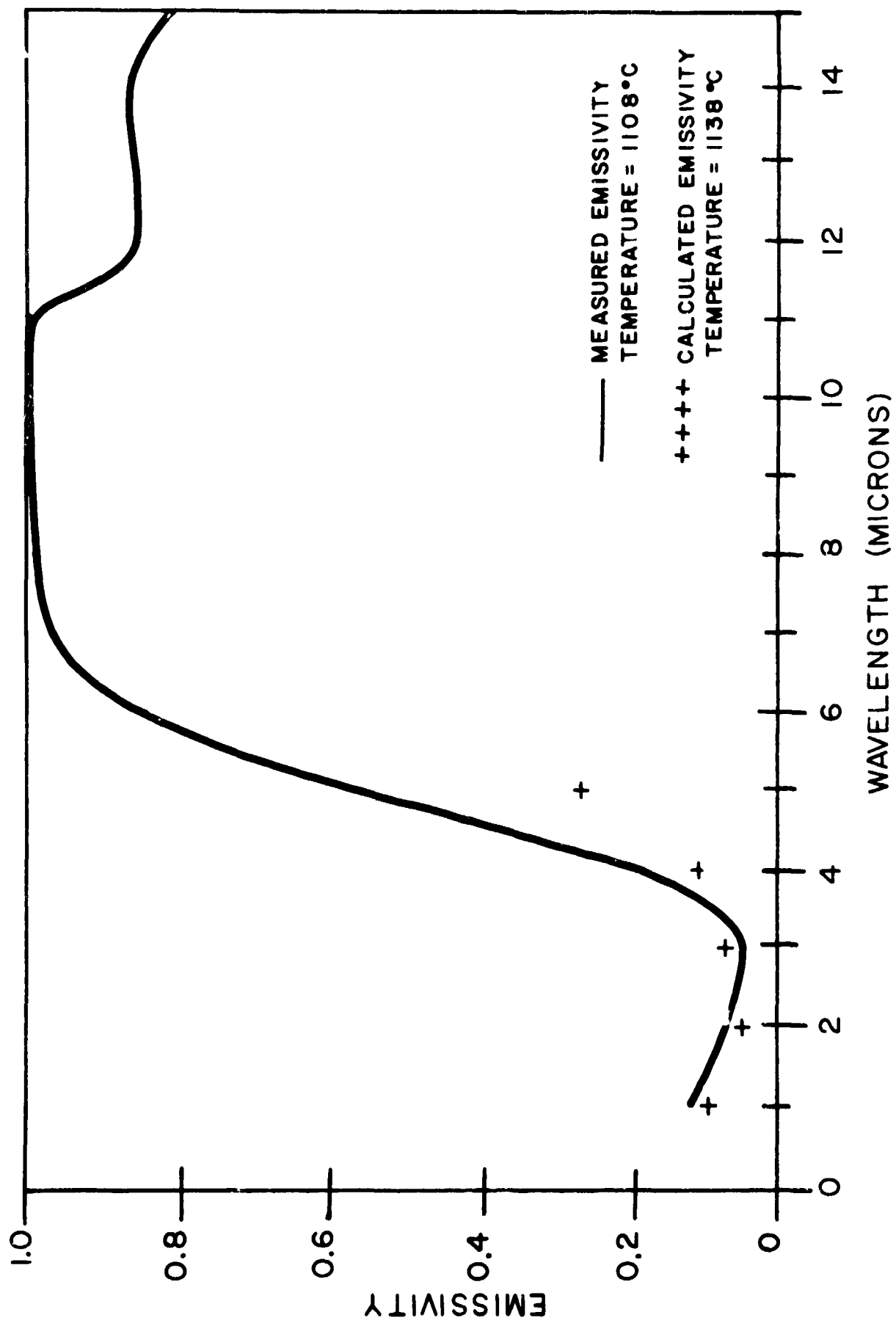


Fig. 7.6 Measured vs. Calculated Emissivity of Al_2O_3 (A₁-2) 1108°C.

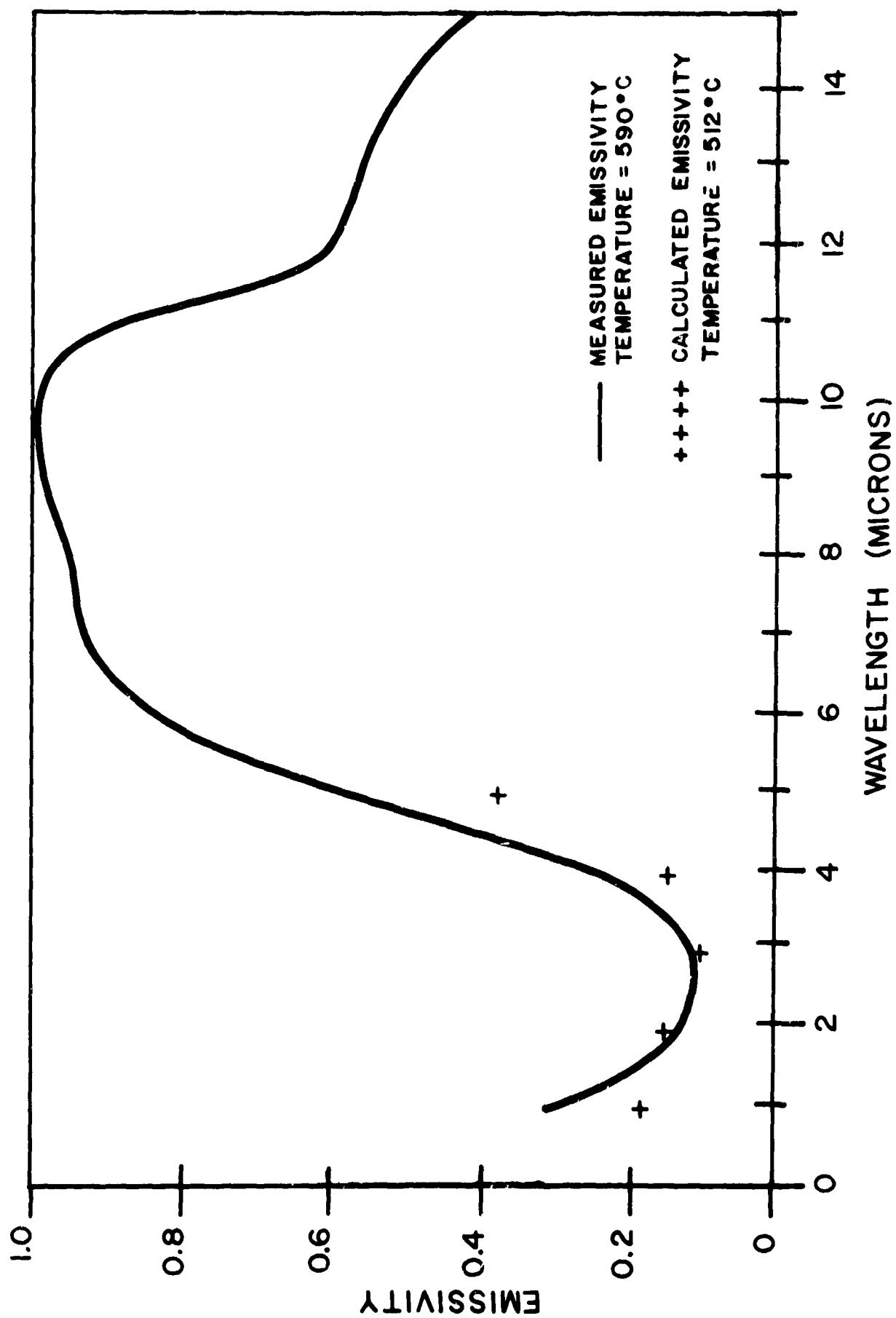


Fig. 7.7 Measured vs. Calculated Emissivity of Al_2O_3 (A ℓ -3) 590°C.

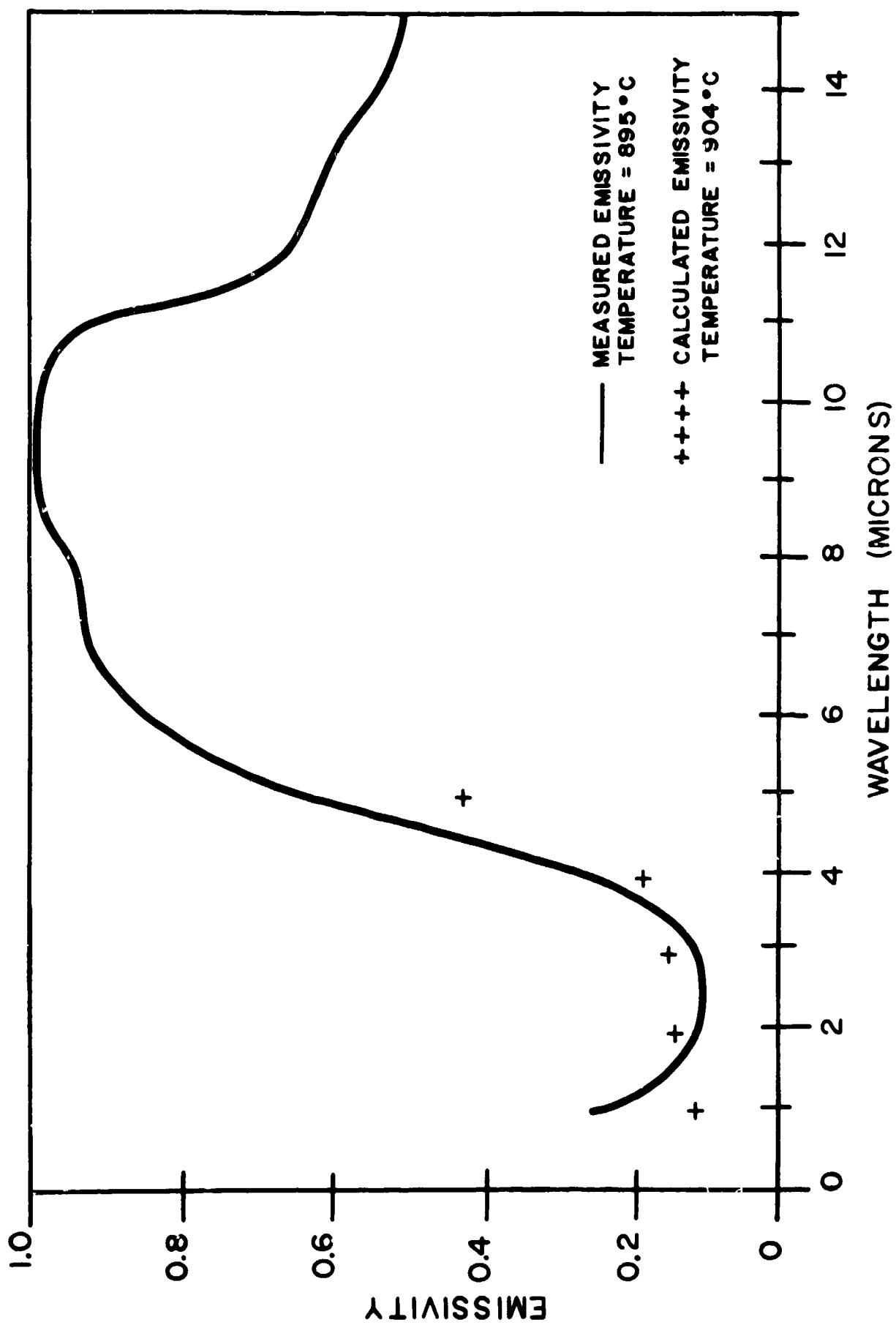


Fig. 7.8 Measured vs. Calculated Emissivity of Al_2O_3 (Al-3) 895°C .

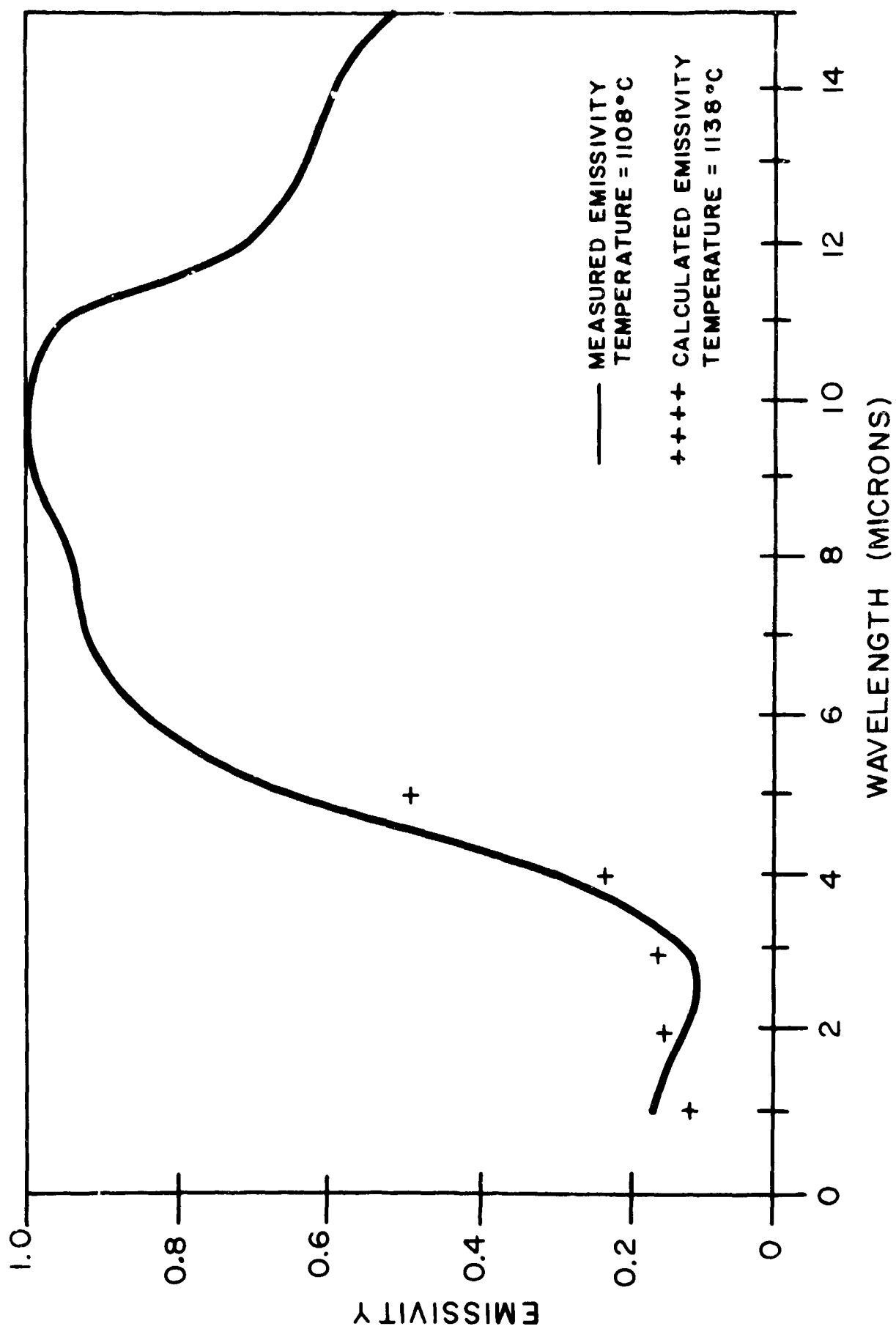


Fig. 7.9 Measured vs. Calculated Emissivity of Al₂O₃ (Al-3) 1108°C.

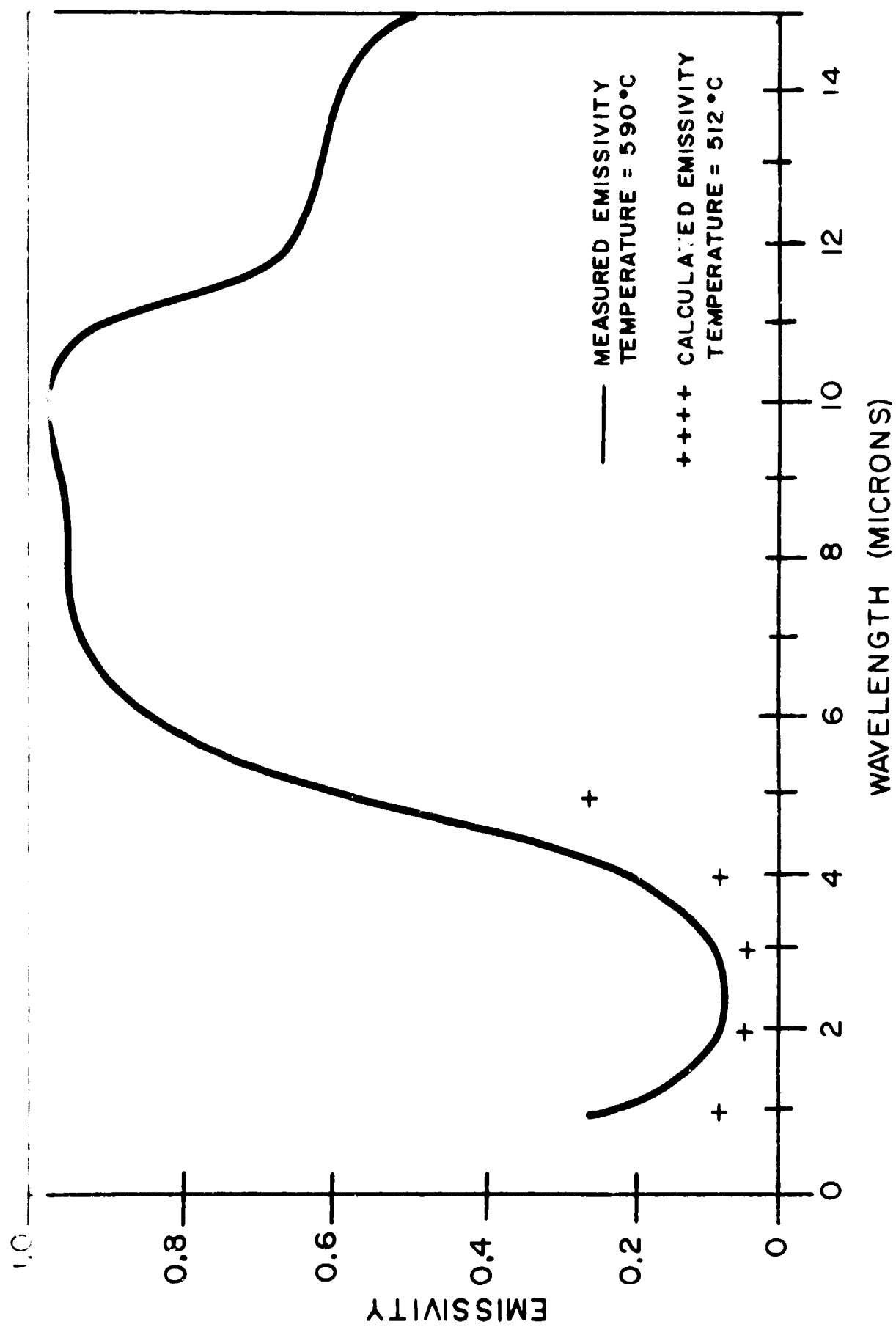


Fig. 7.10 Measured vs. Calculated Emissivity of Al_2O_3 (A/-4) 590°C.

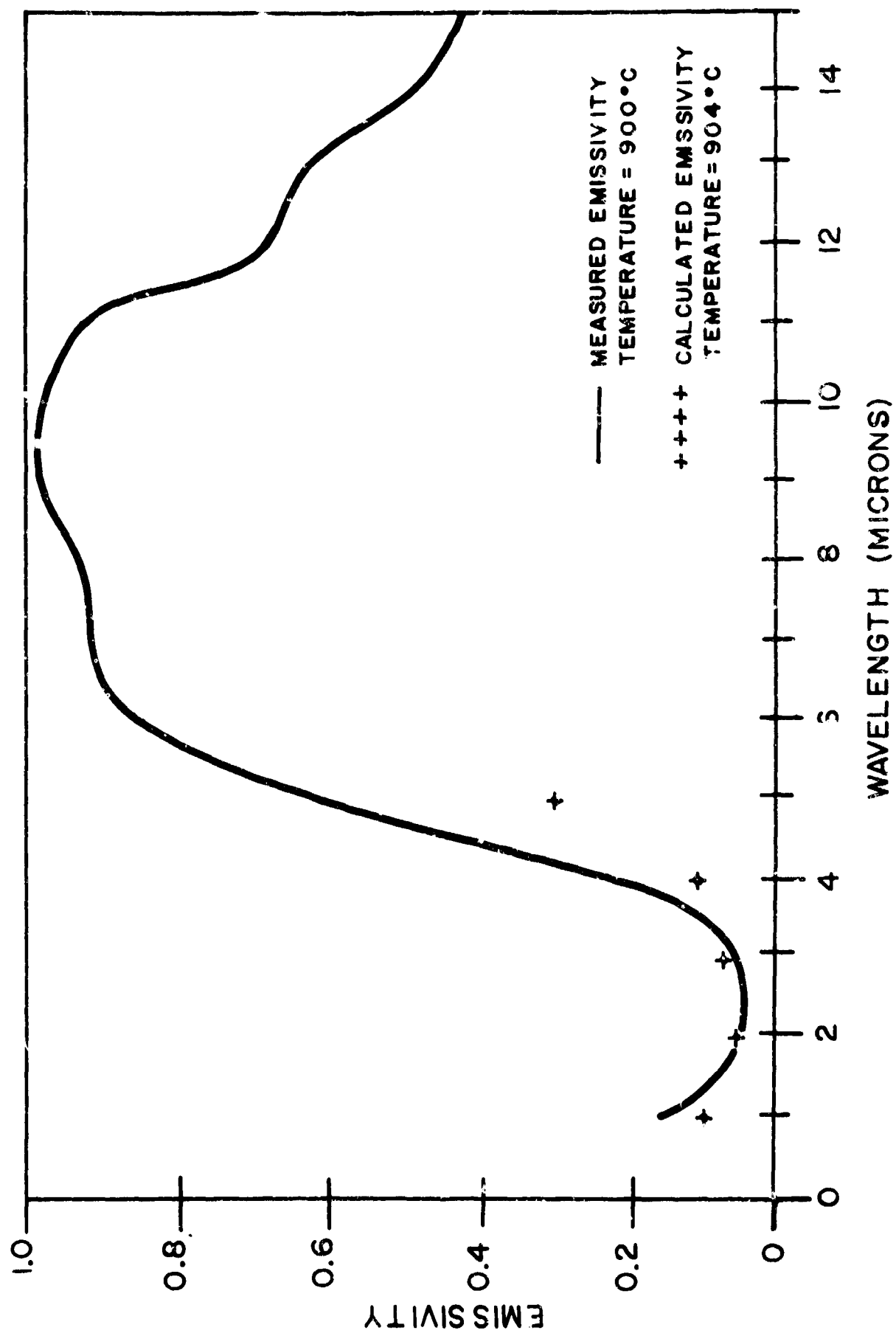


Fig. 7.11 Measured vs. Calculated Emissivity of Al_2O_3 (Al-4) 900°C .

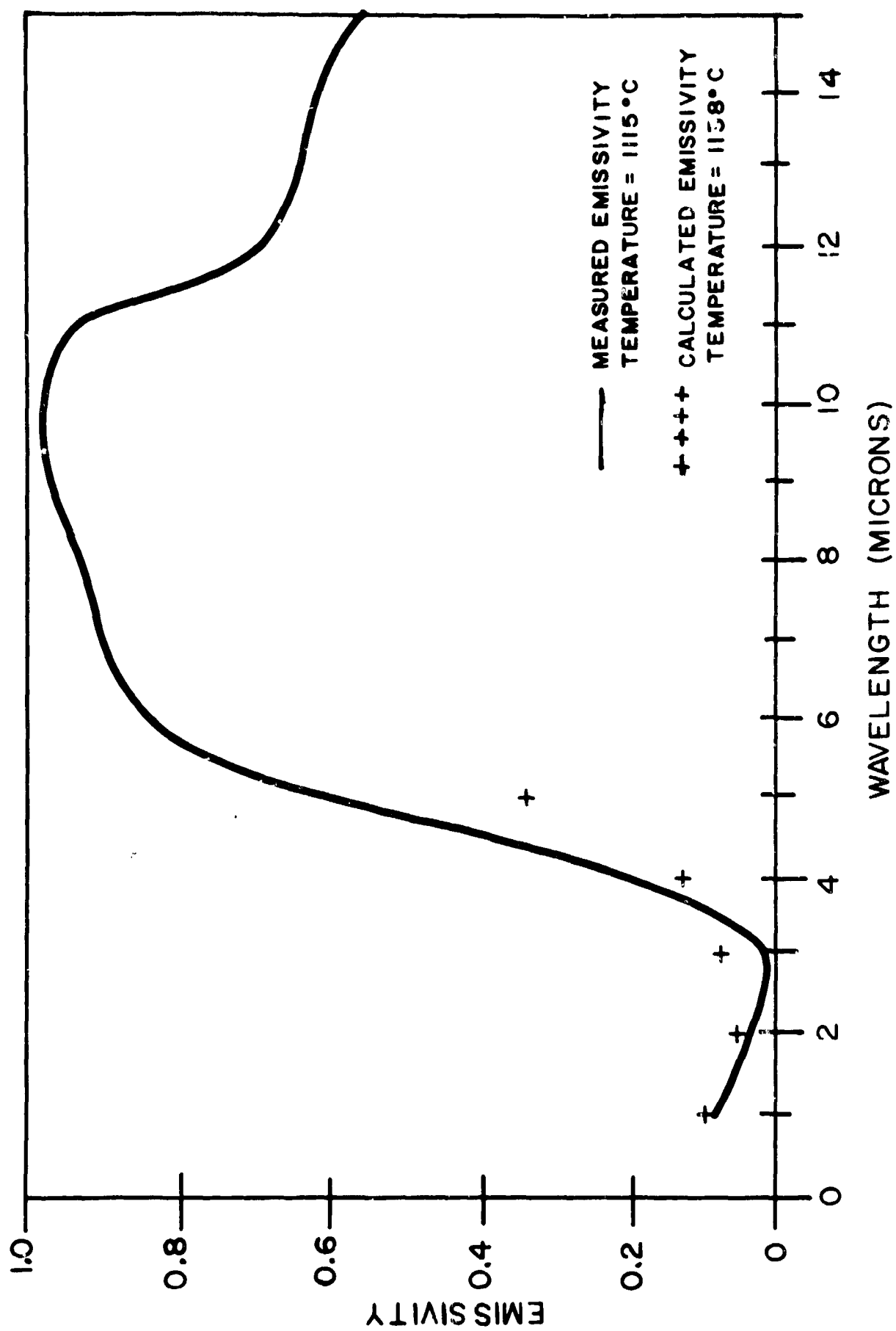


Fig. 7.12 Measured vs. Calculated Emissivity of Al_2O_3 (A2-4) 1115°C.

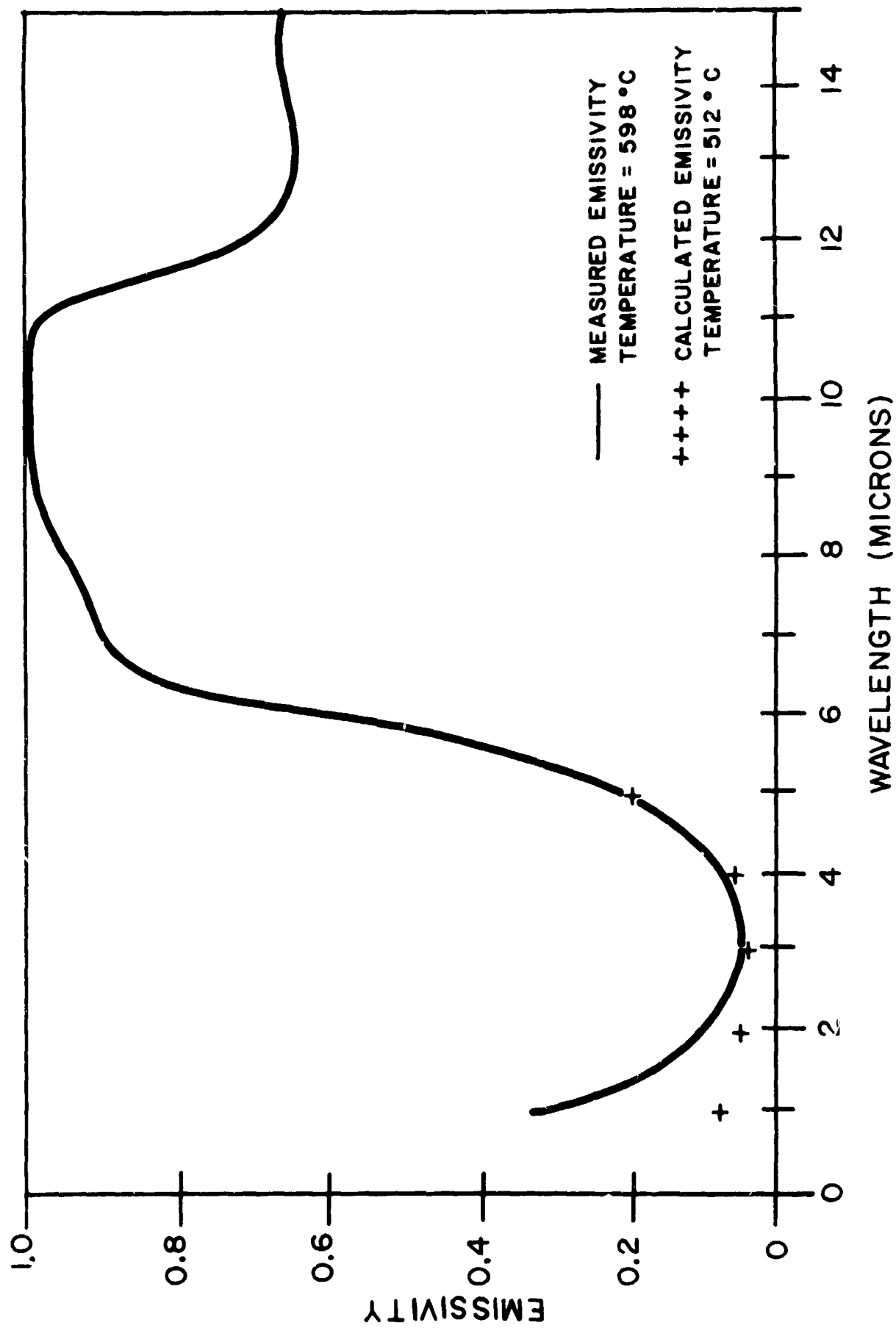


Fig. 7.13 Measured vs. Calculated Emissivity of Al₂O₃ (Al-6) 598 °C.

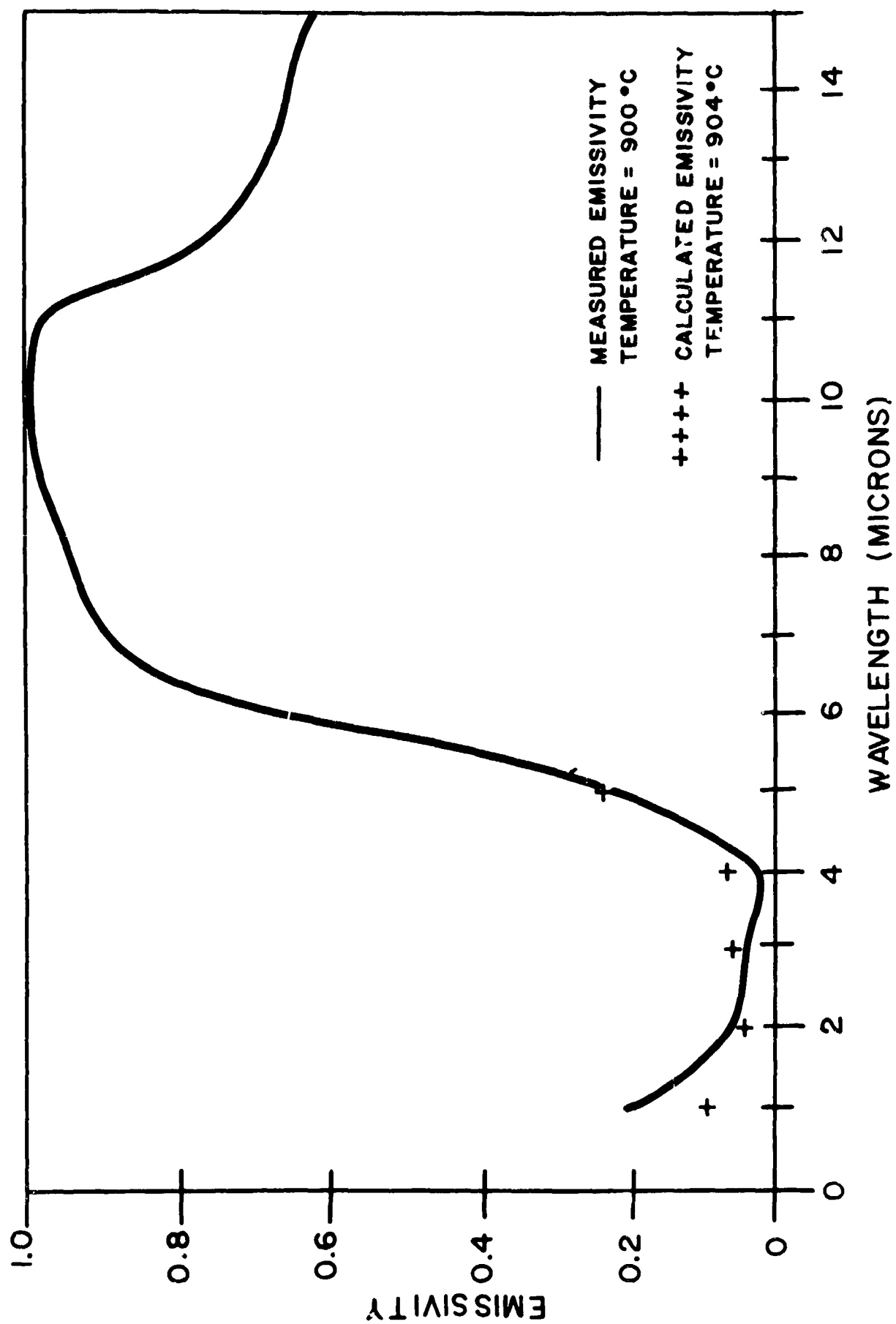


Fig. 7.14 Measured vs. Calculated Emissivity of Al₂O₃ (Al-6) 900°C.

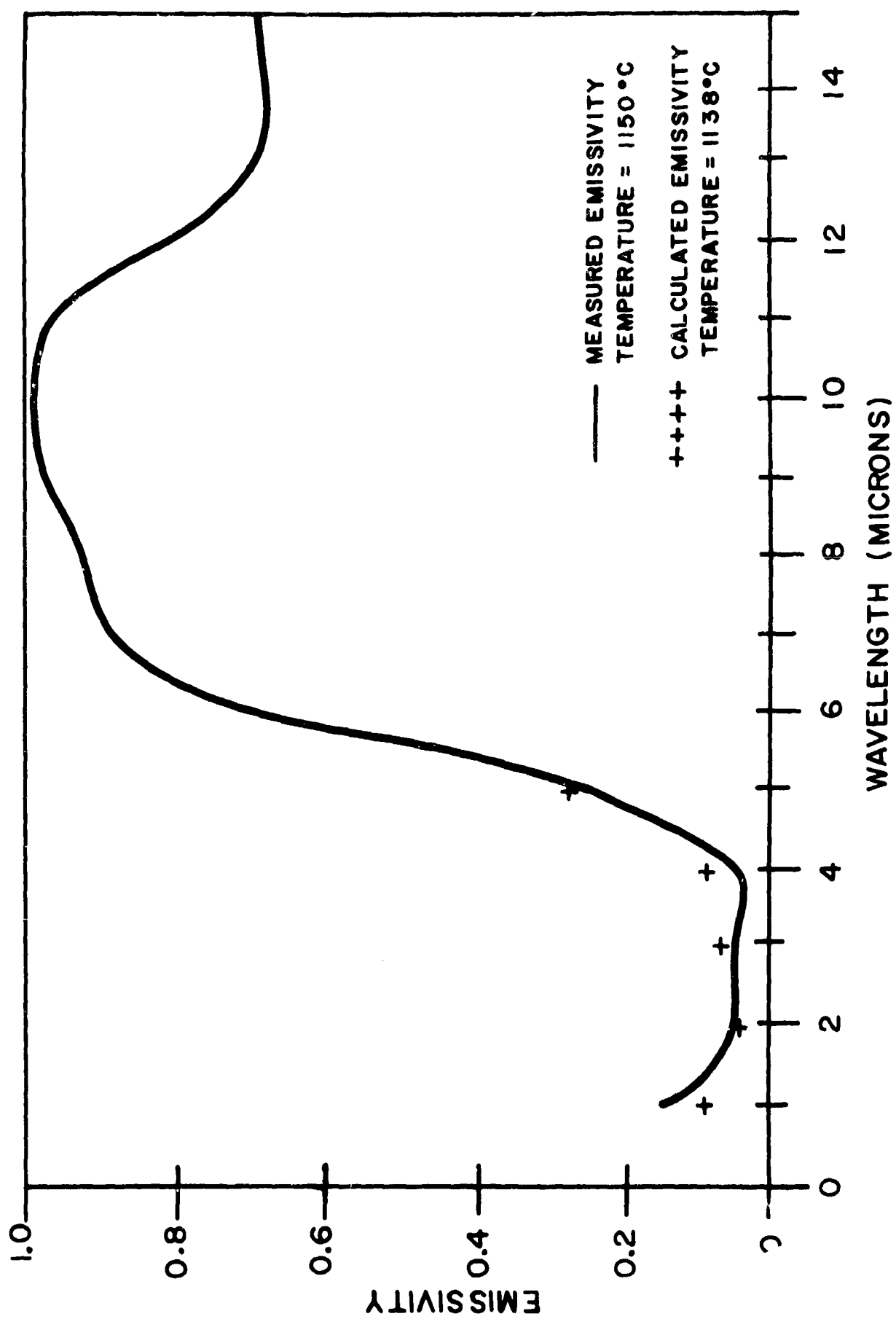


Fig. 7.15 Measured vs. Calculated Emissivity of Al_2O_3 (Al-6) 1150°C.

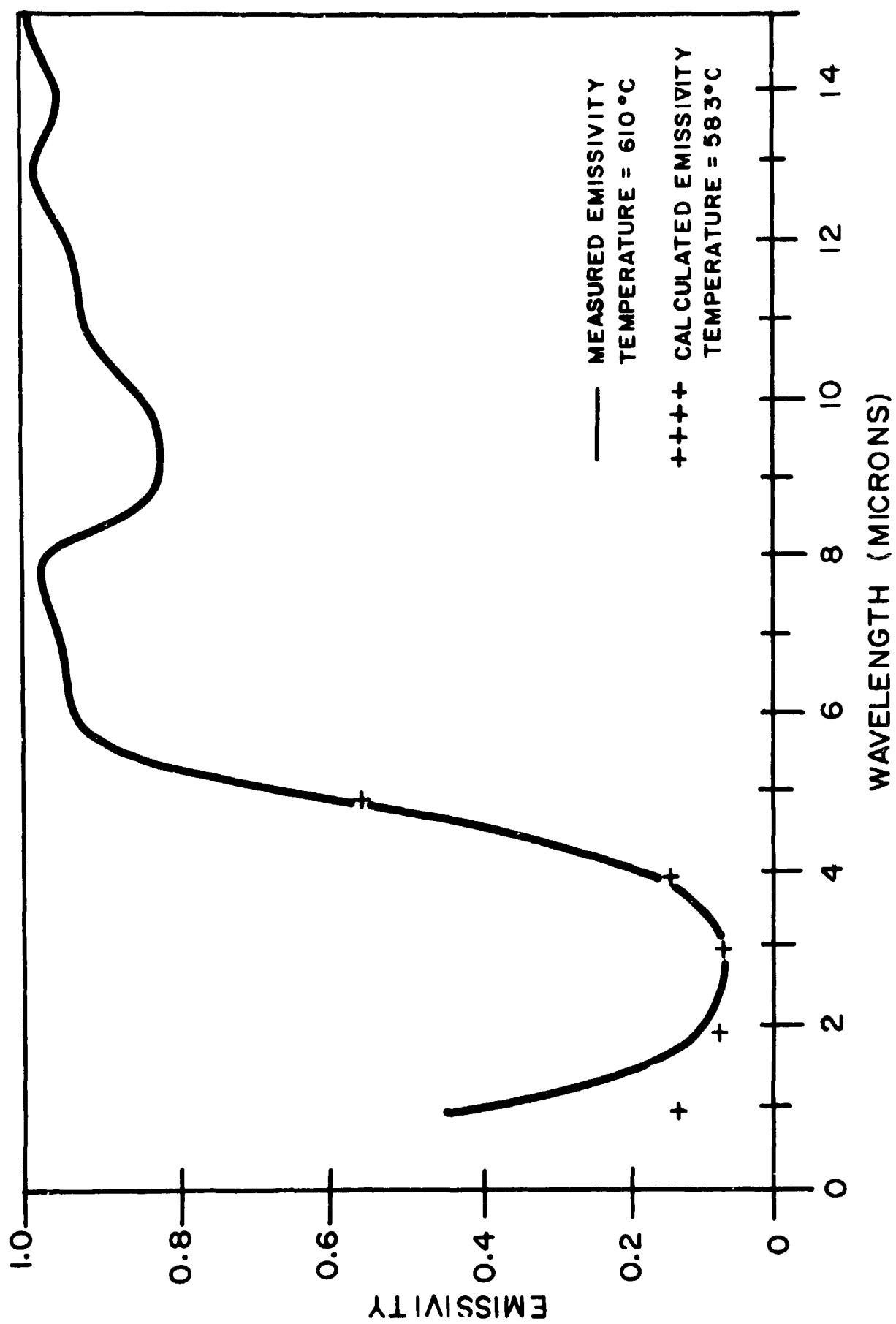


Fig. 7.16 Measured vs. Calculated Emissivity of Silica Glass (FS-3) 610°C.

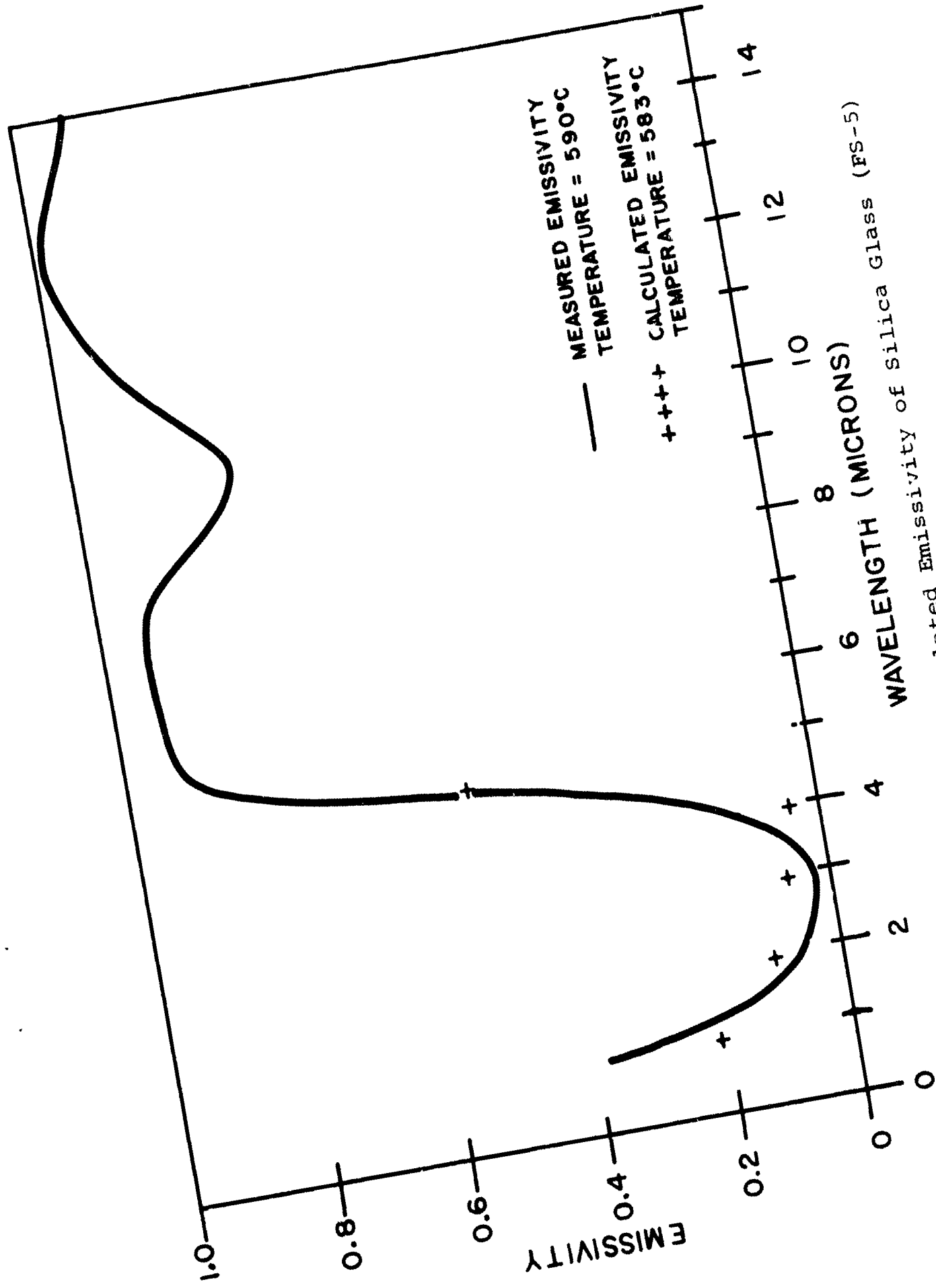


Fig. 7.18 Measured vs. Calculated Emissivity of Silica Glass (FS-5)
590°C.

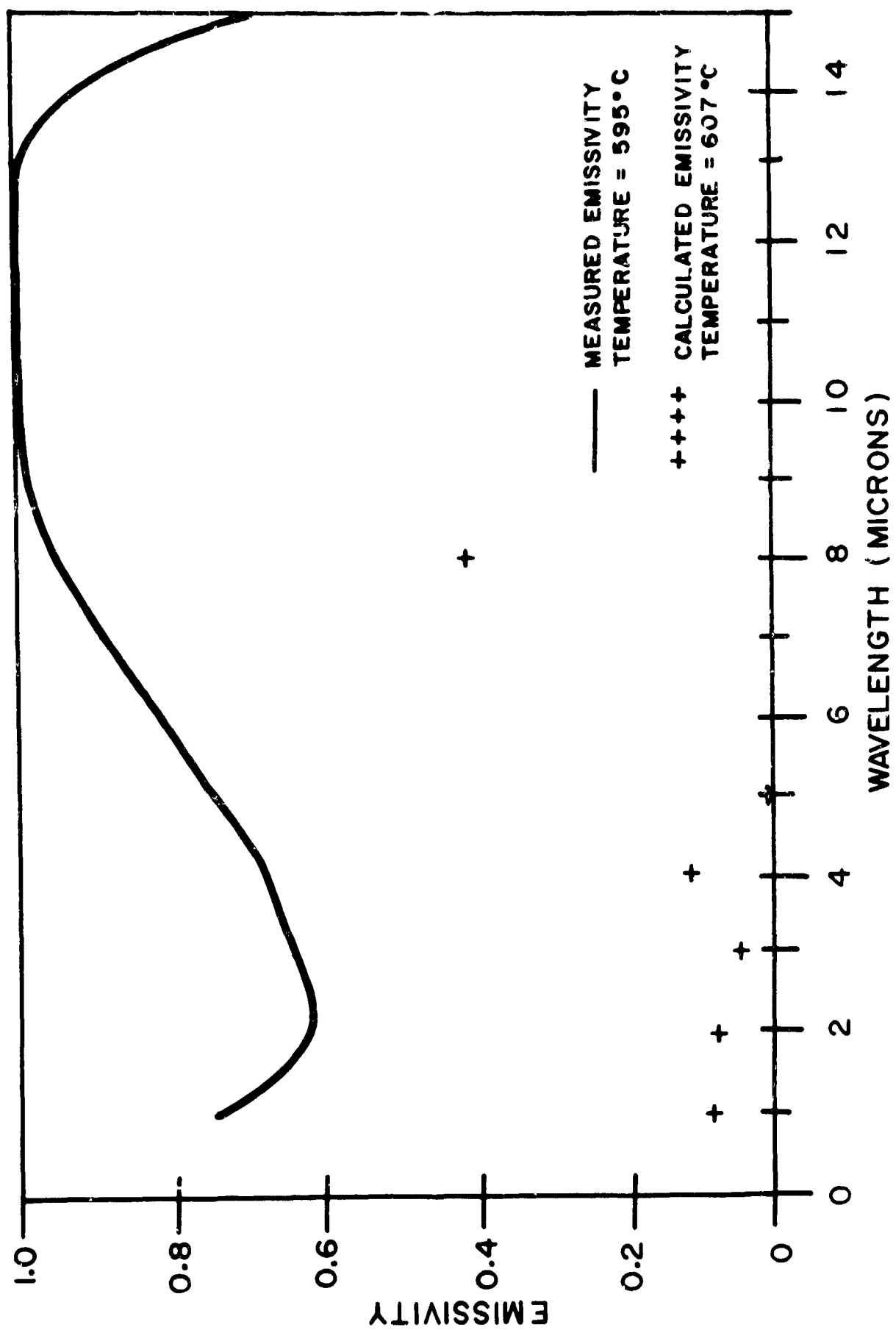


Fig. 7.20 Measured vs. Calculated Emissivity of MgO (Mg-3) 595°C.

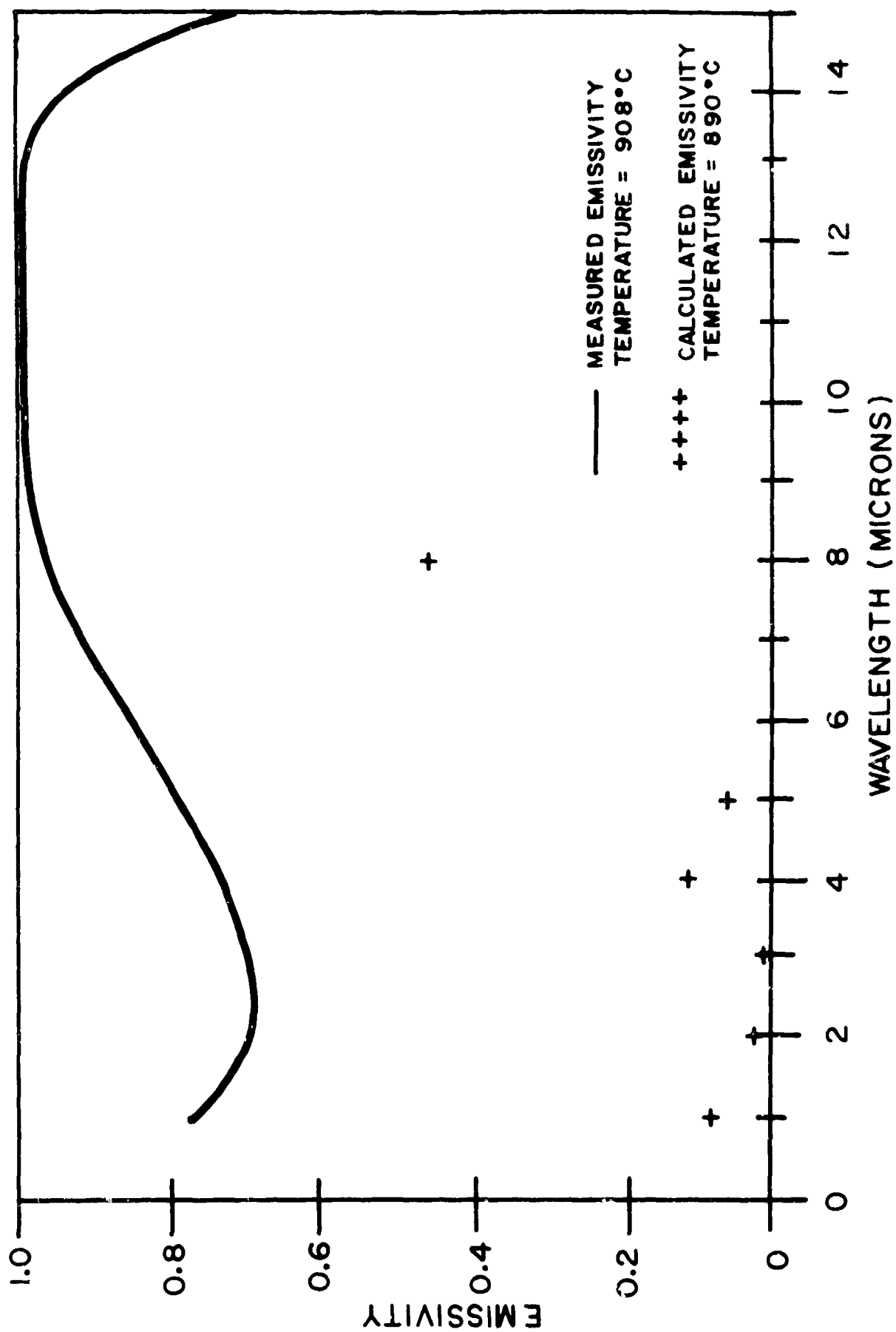


Fig. 7.21 Measured vs. Calculated Emissivity of MgO (Mg-3) 908°C.

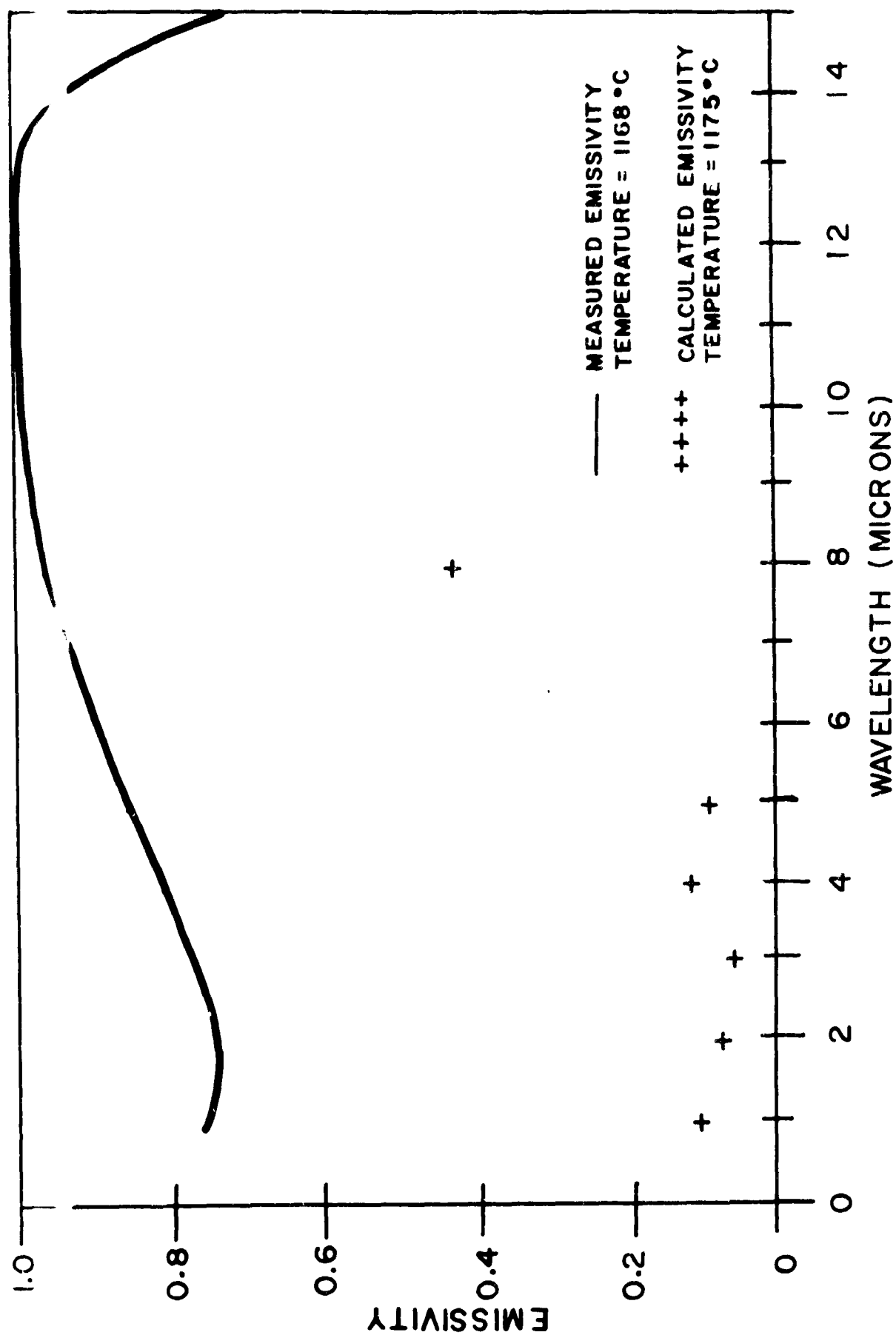


Fig. 7.22 Measured vs. Calculated Emissivity of MgO (Mg-5) 1168°C.

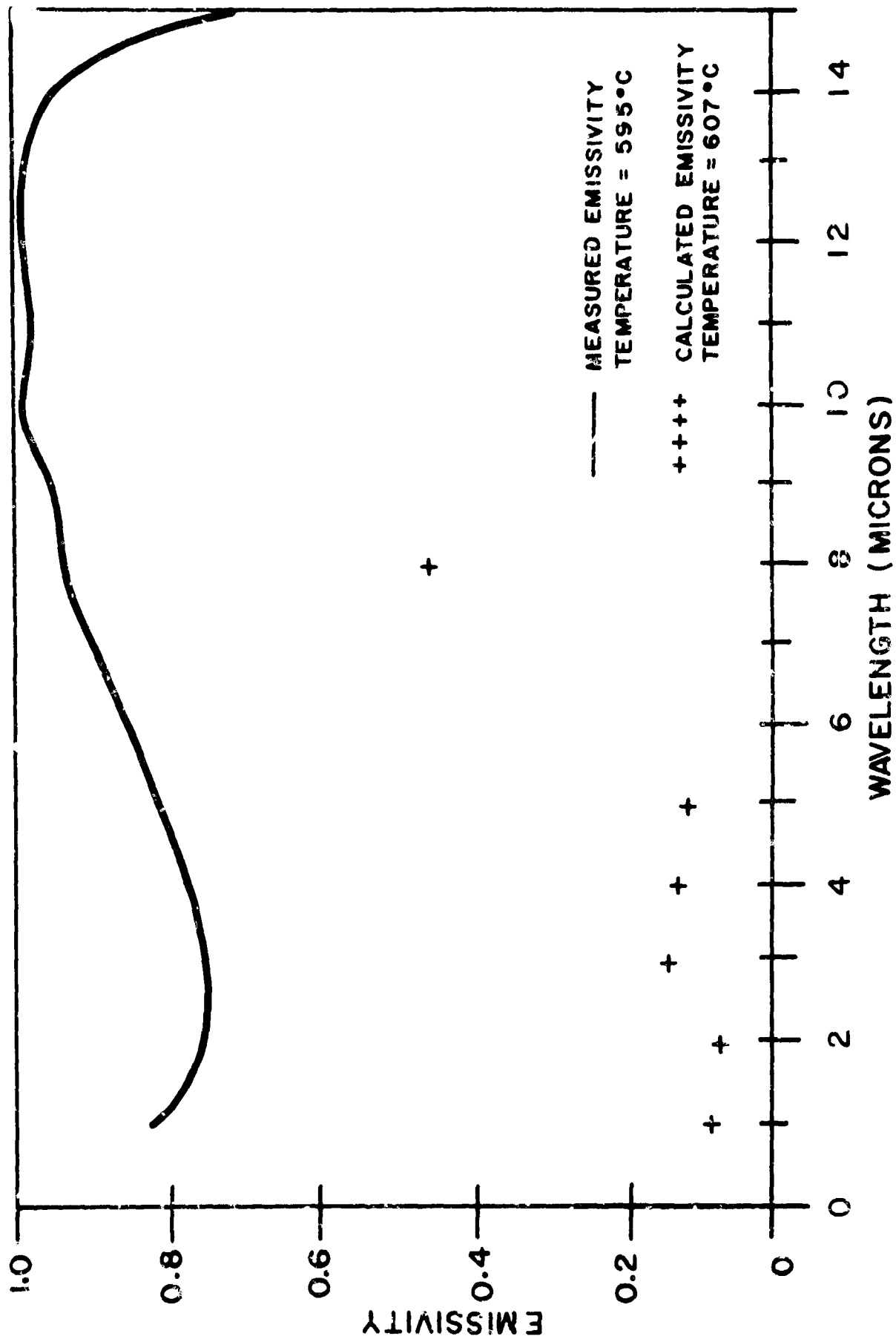
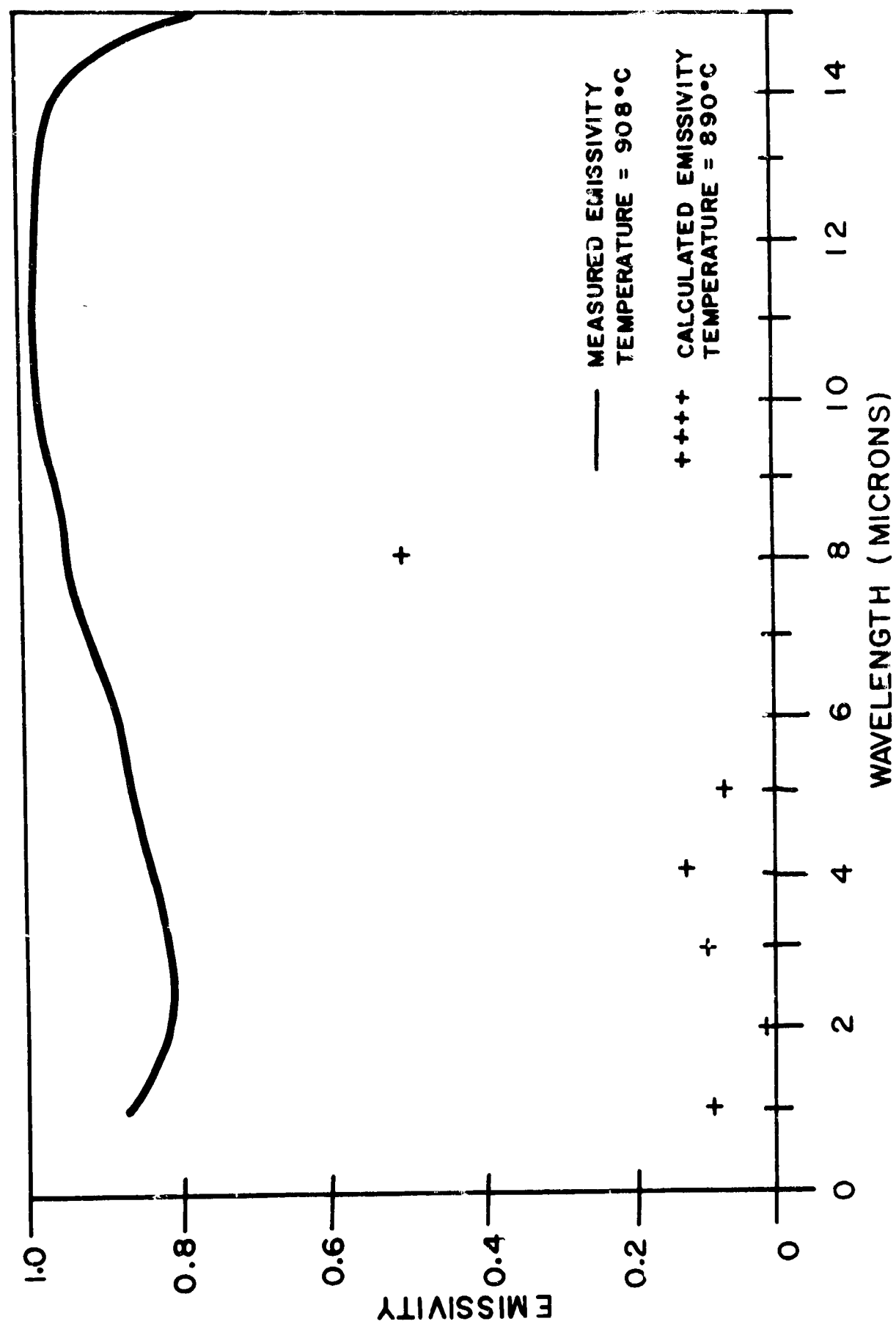


Fig. 7.23 Measured vs. Calculated Emissivity of MgO (Mg-5) 595°C.



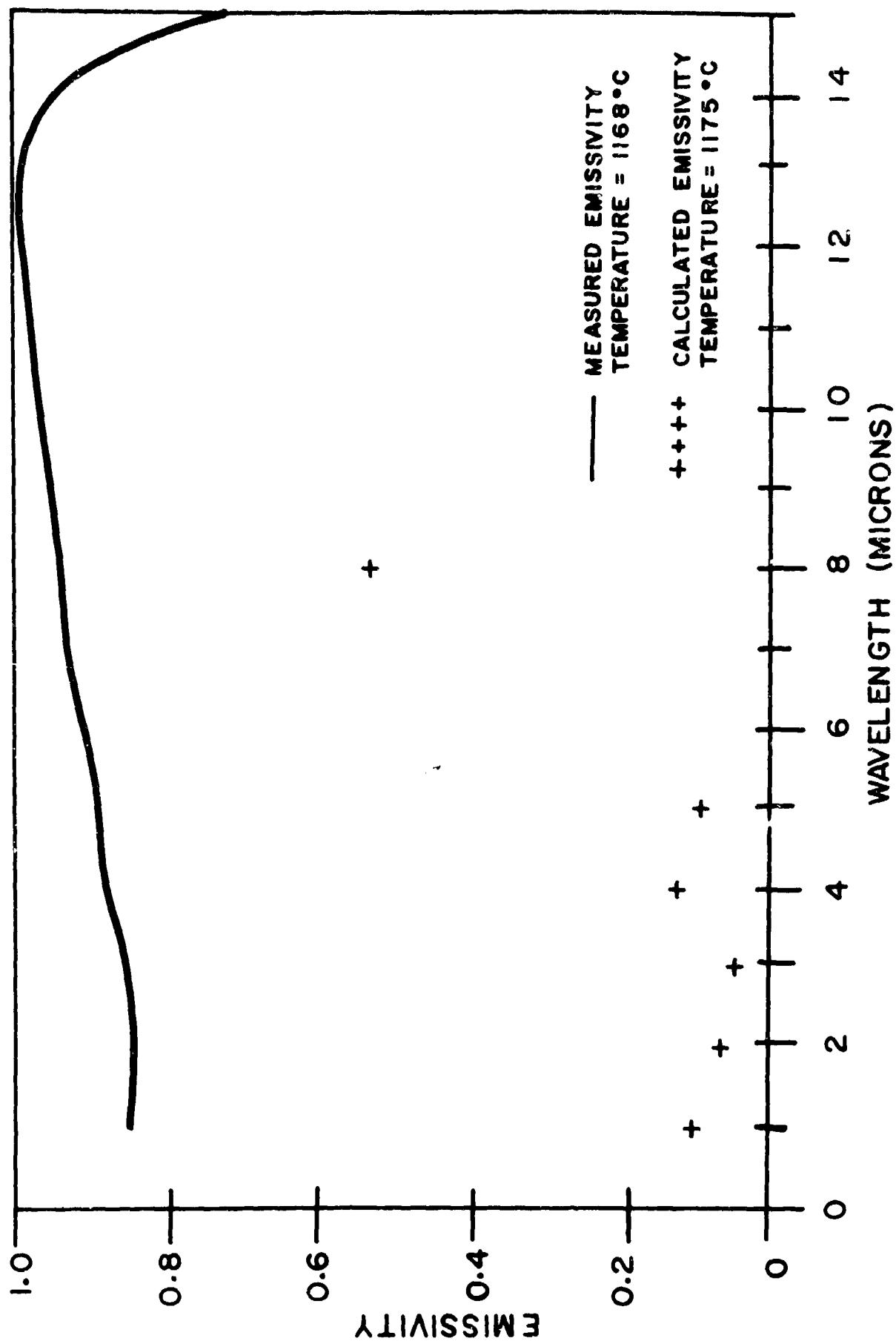


Fig. 7.25 Measured vs. Calculated Emissivity of MgO (Mg-5) 1168°C.

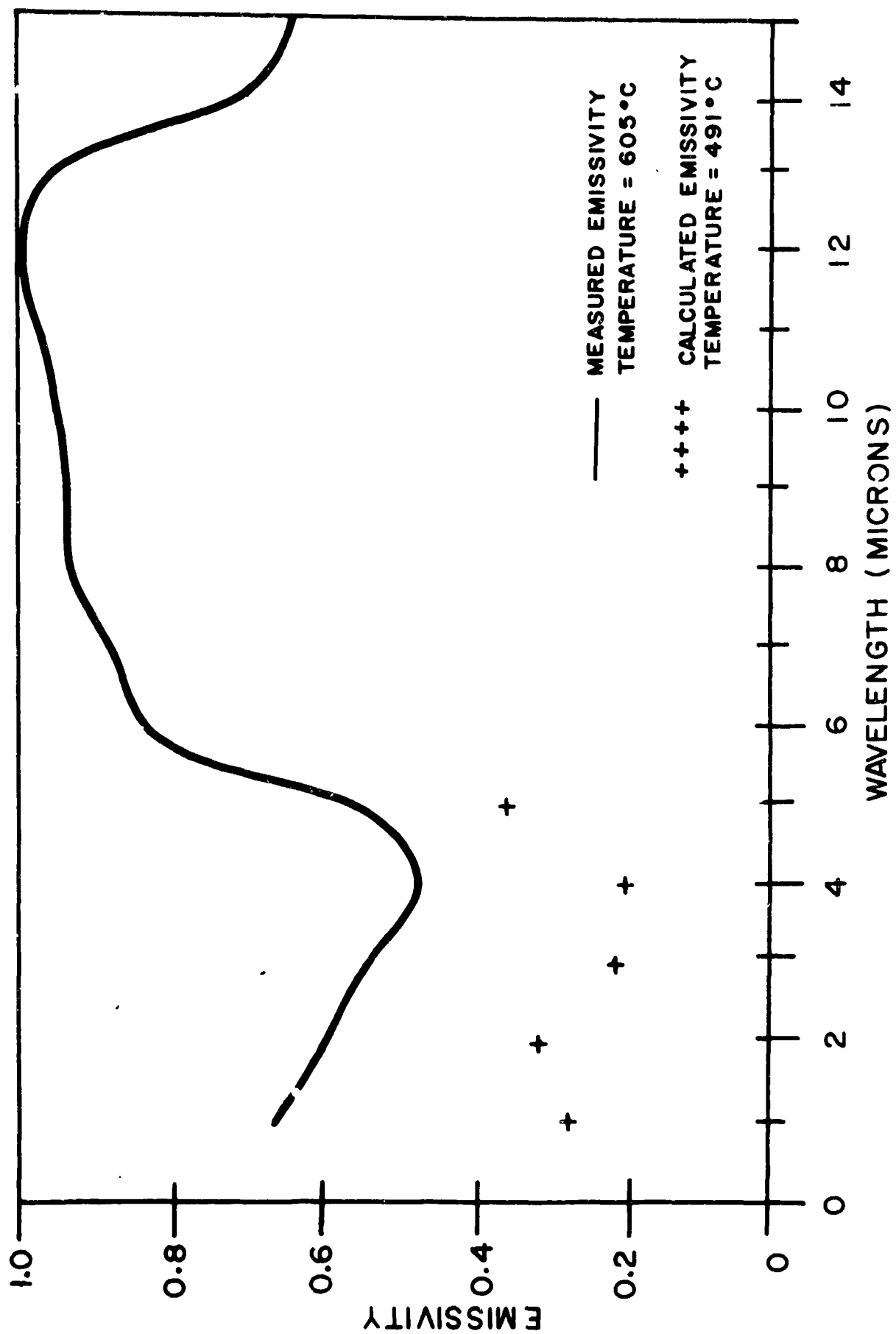


Fig. 7.26 Measured vs. Calculated Emissivity of SrTiO₃ (Sr-1) 605°C.

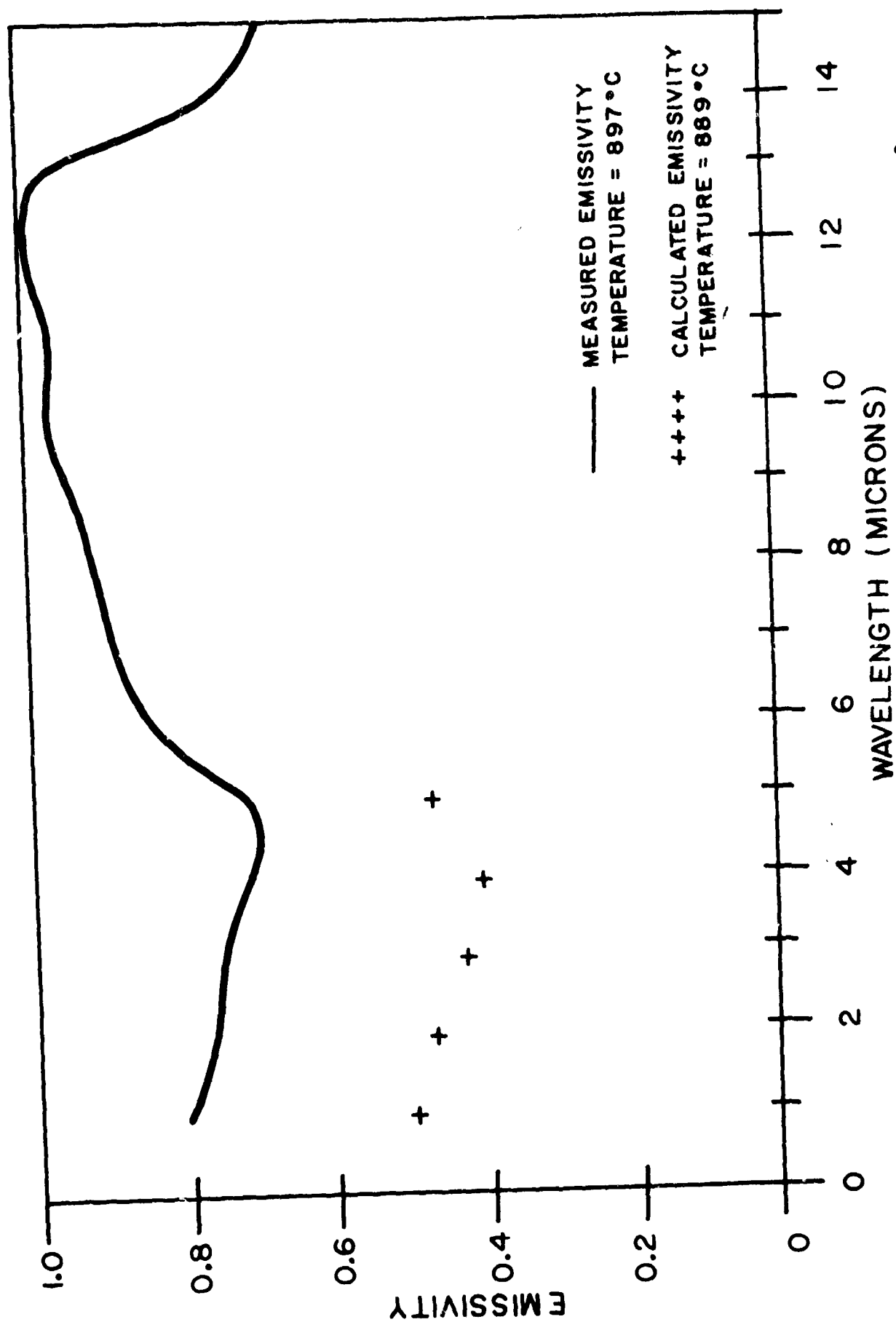


Fig. 7.27 Measured vs. Calculated Emissivity of SrTiO₃ (Sr-1) 897°C.

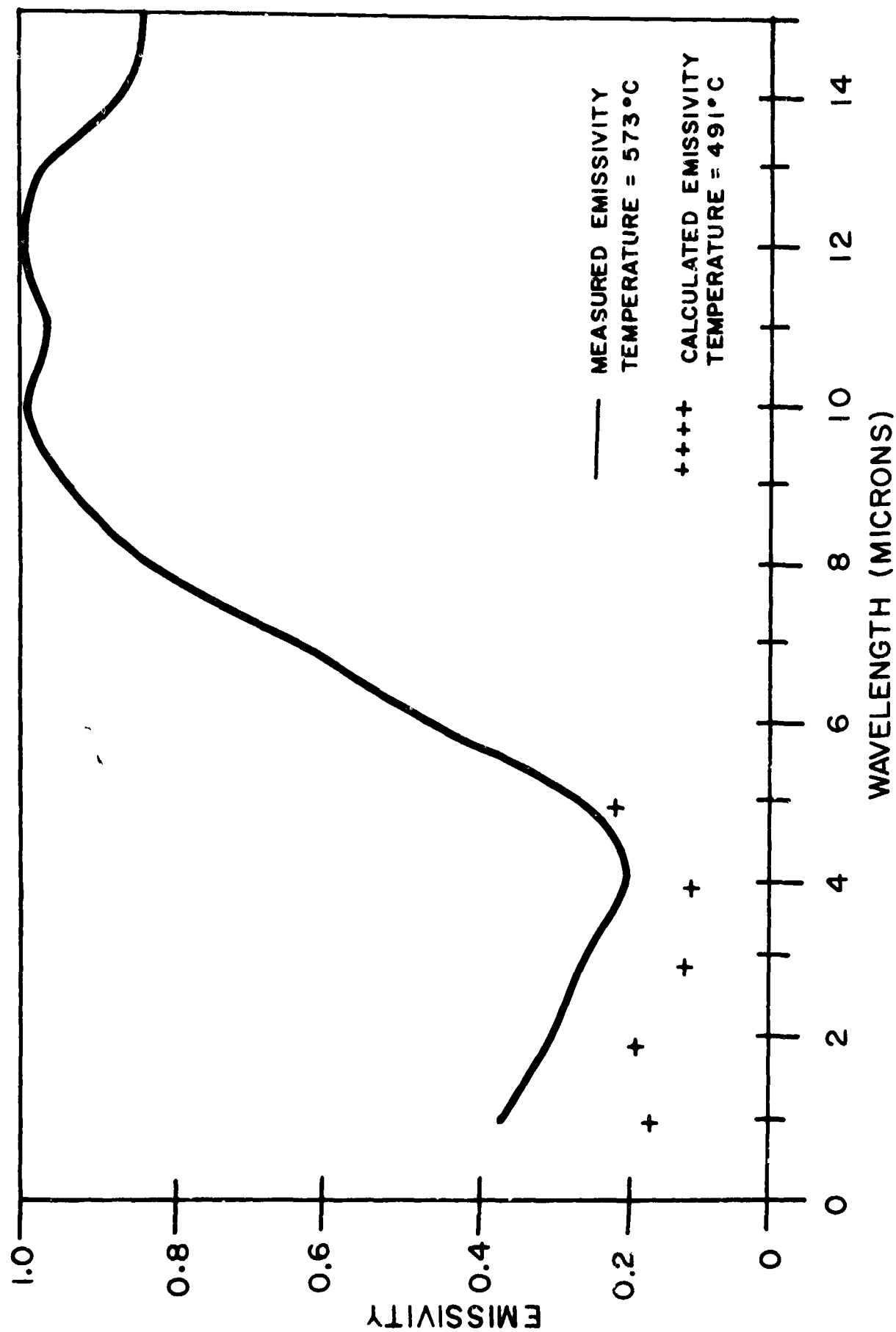


Fig. 7.28 Measured vs. Calculated Emissivity of SrTiO₃ (Sr-2) 573°C.

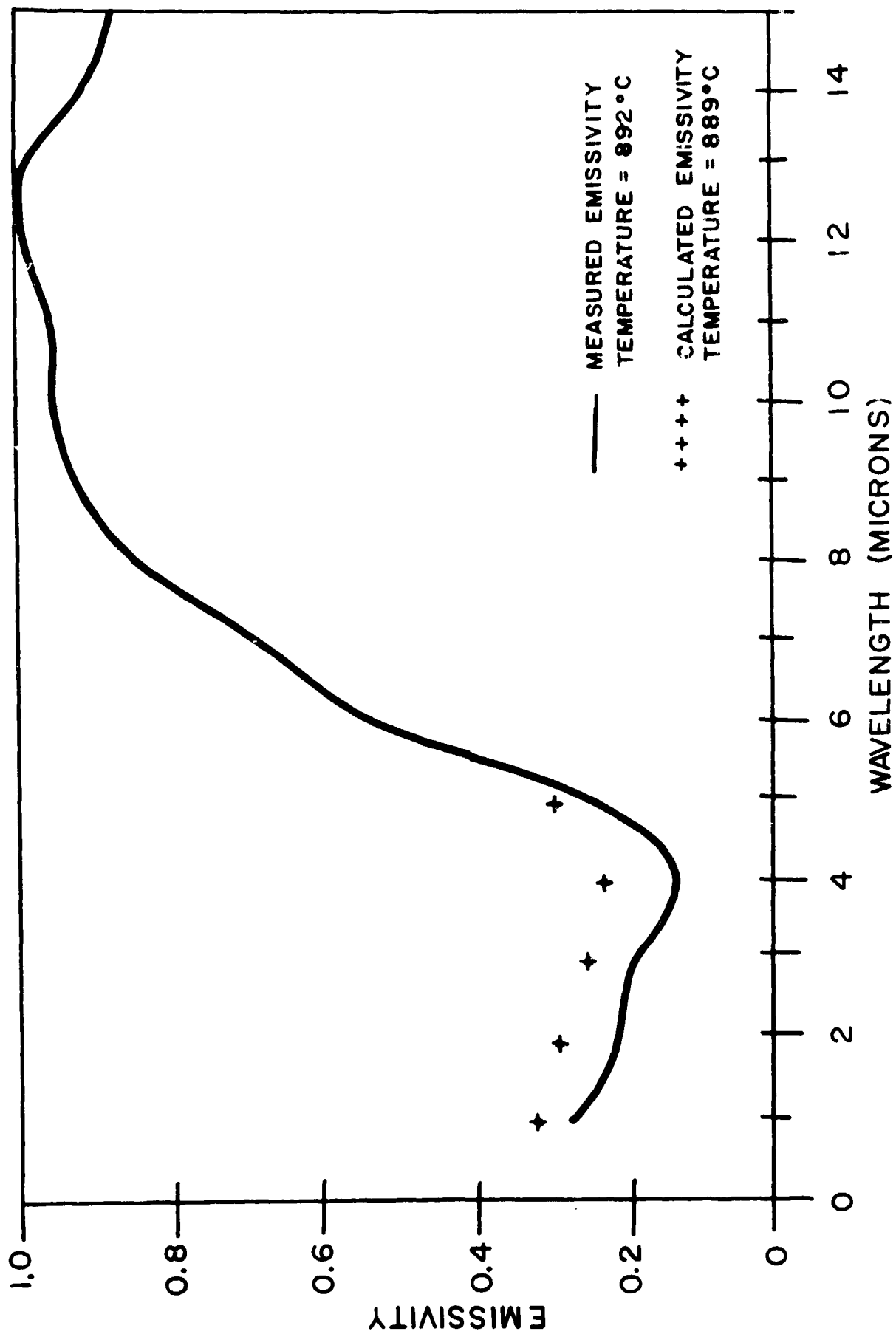


Fig. 7.29 Measured vs. Calculated Emissivity of SrTiO₃ (Sr-2) 892°C.

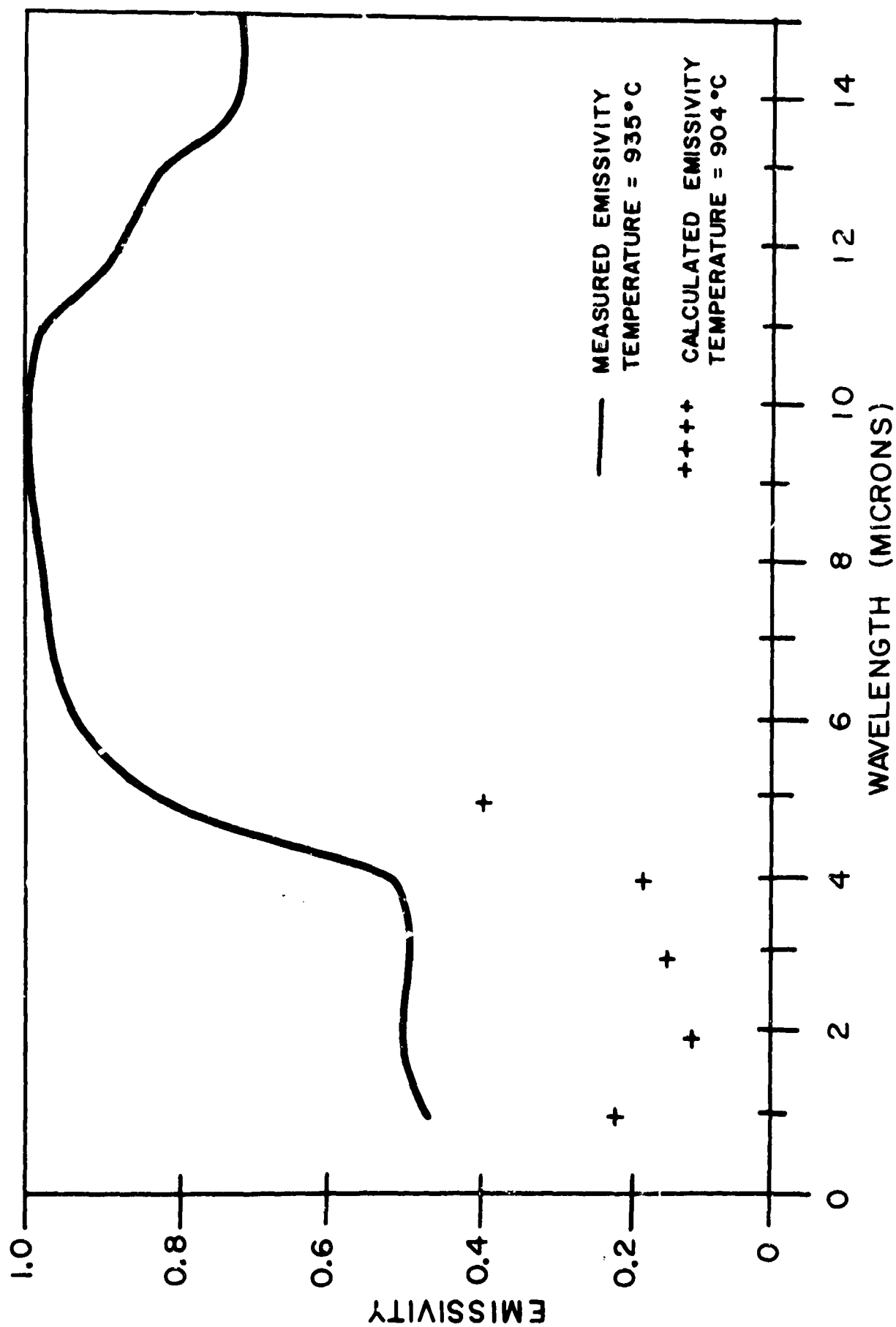


Fig. 7.30 Measured vs. Calculated Emissivity of Commercial Al_2O_3 (AD-85) 935°C.

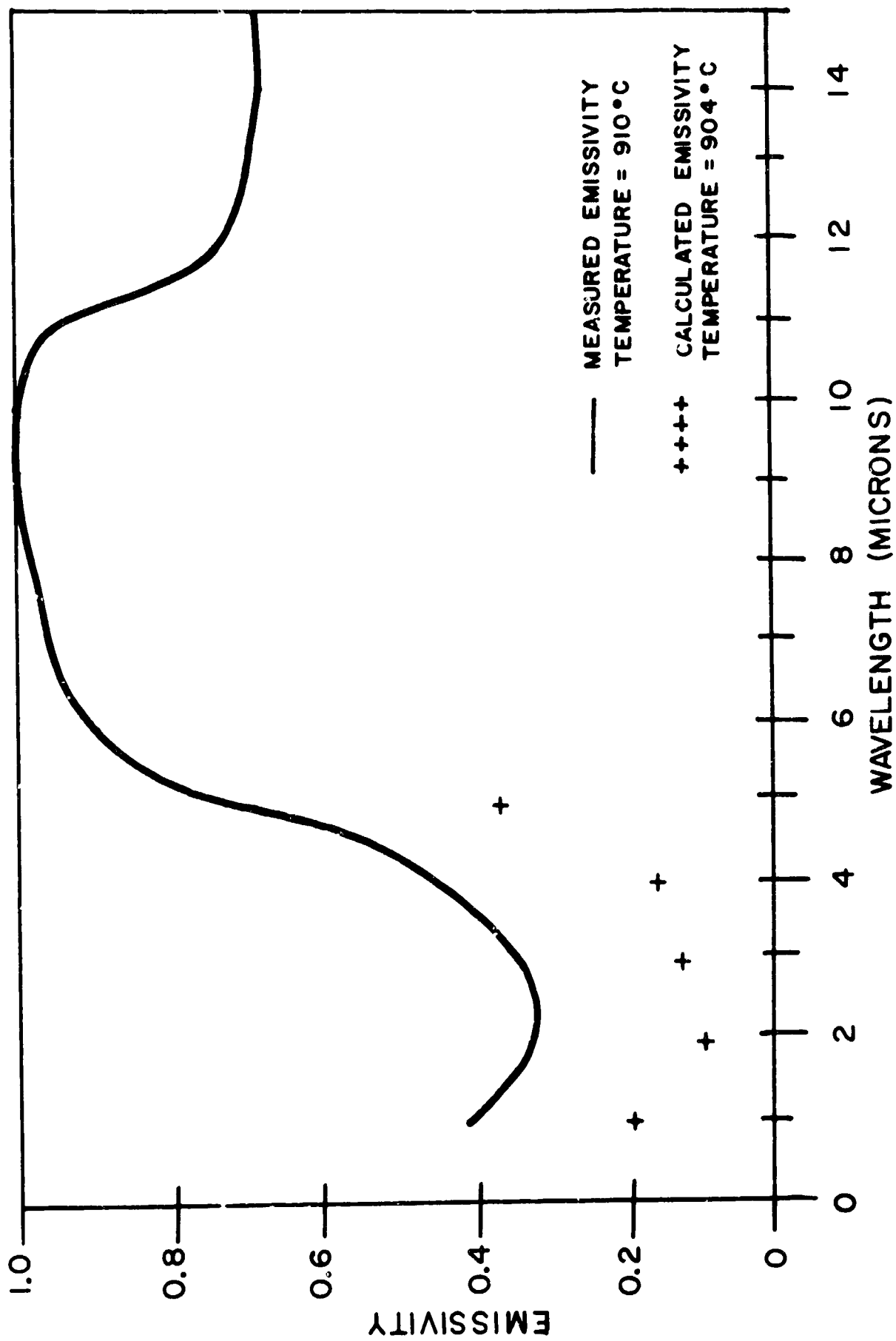


Fig. 7.31 Measured vs. Calculated Emissivity of Commercial Al_2O_3 (AD-96) 910°C .

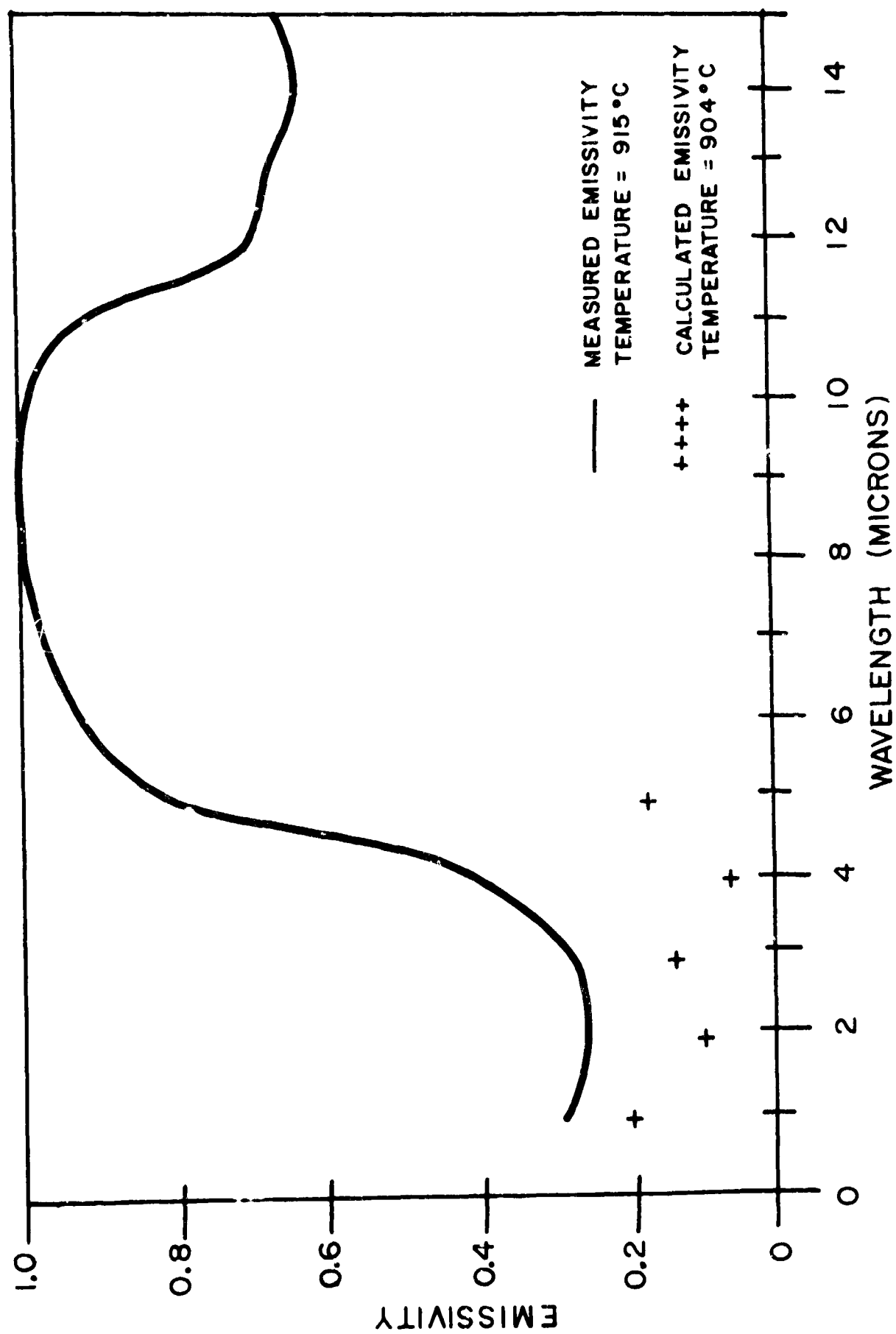


Fig. 7.32 Measured vs. Calculated Emissivity of Commercial Al_2O_3 (AD-99) 915°C.

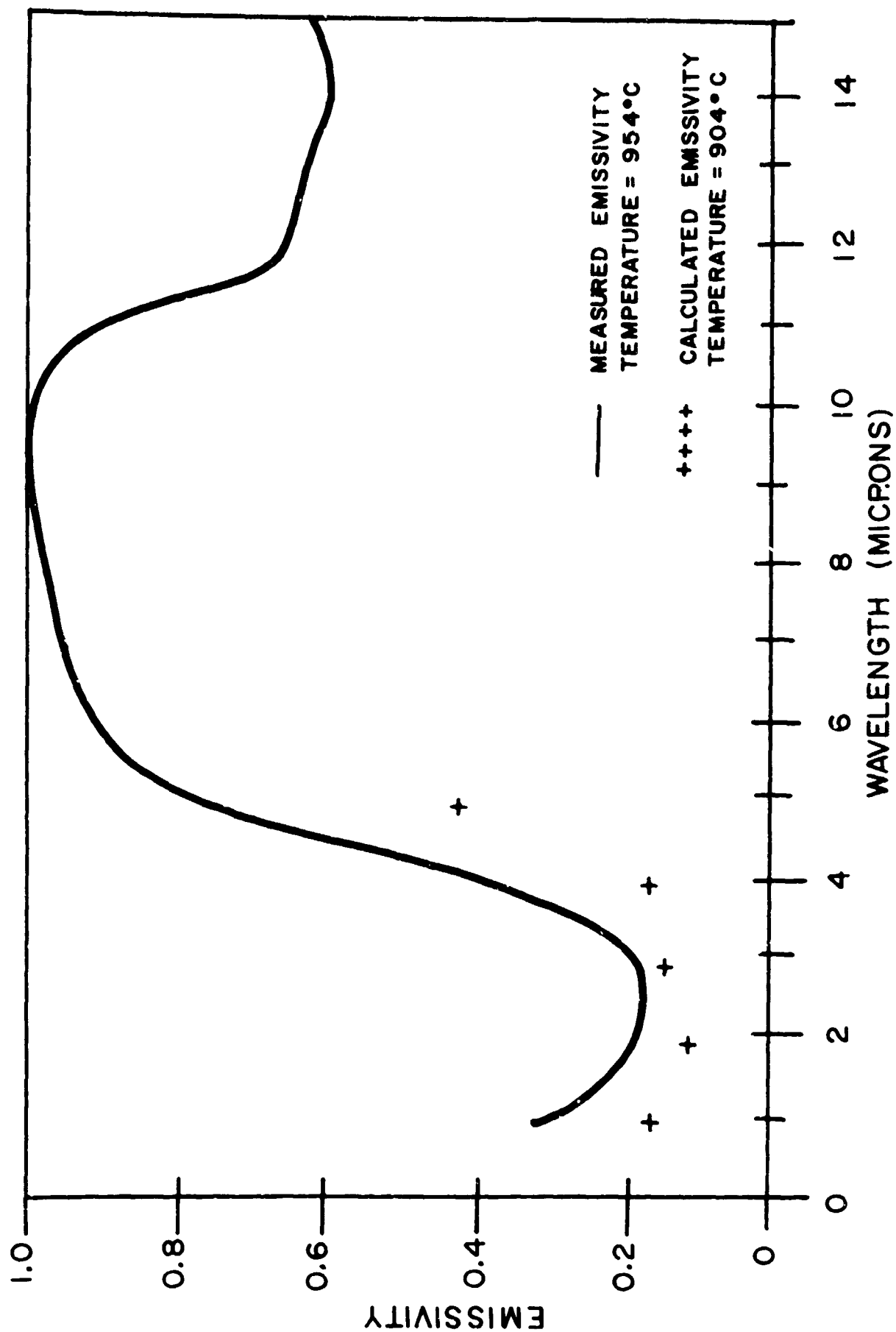


Fig. 7.33 Measured vs. Calculated Emissivity of Commercial Al_2O_3 (AD-995) 954°C .

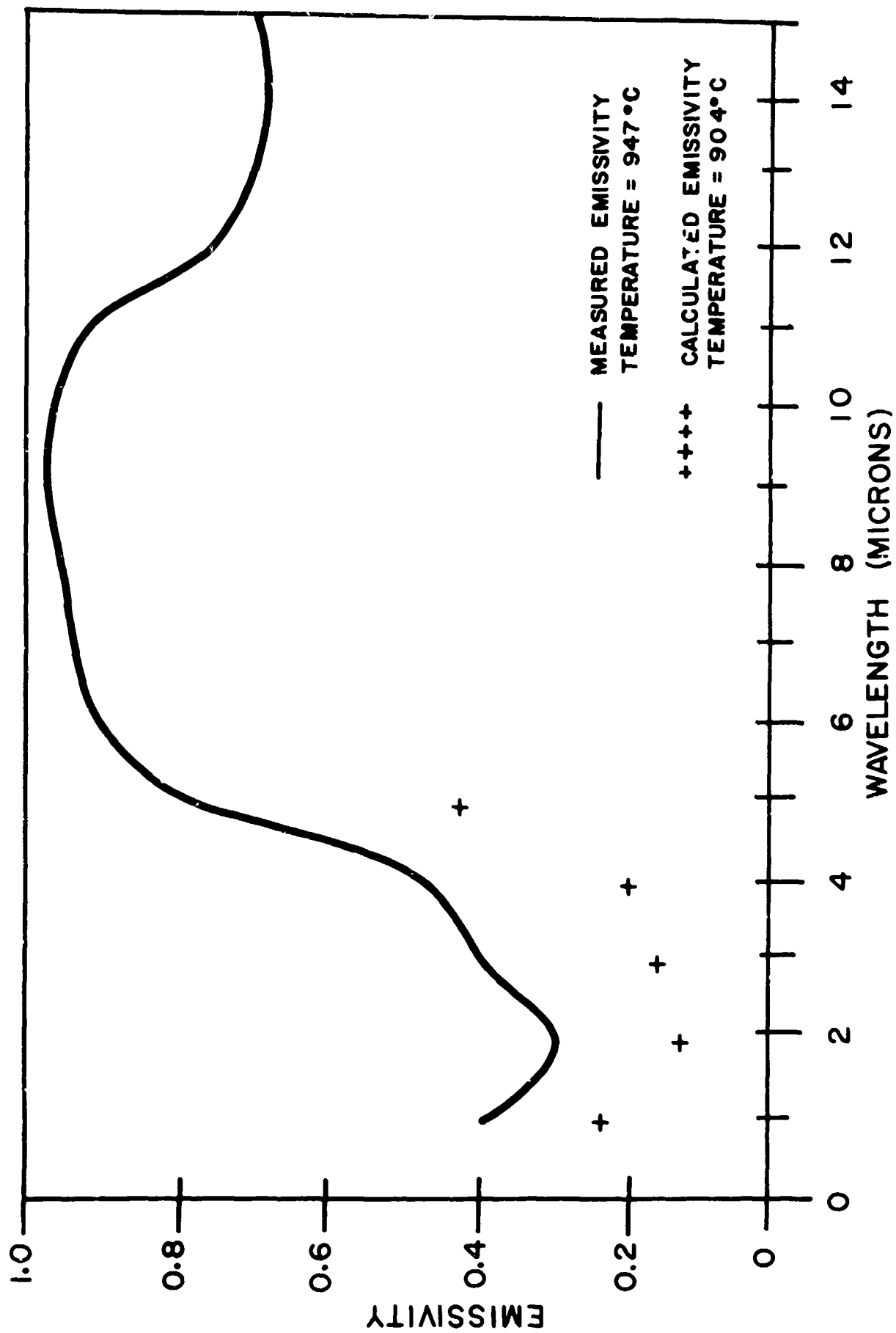


Fig. 7.34 Measured vs. Calculated Emissivity of Commercial Al_2O_3 (AD-94) 947°C .

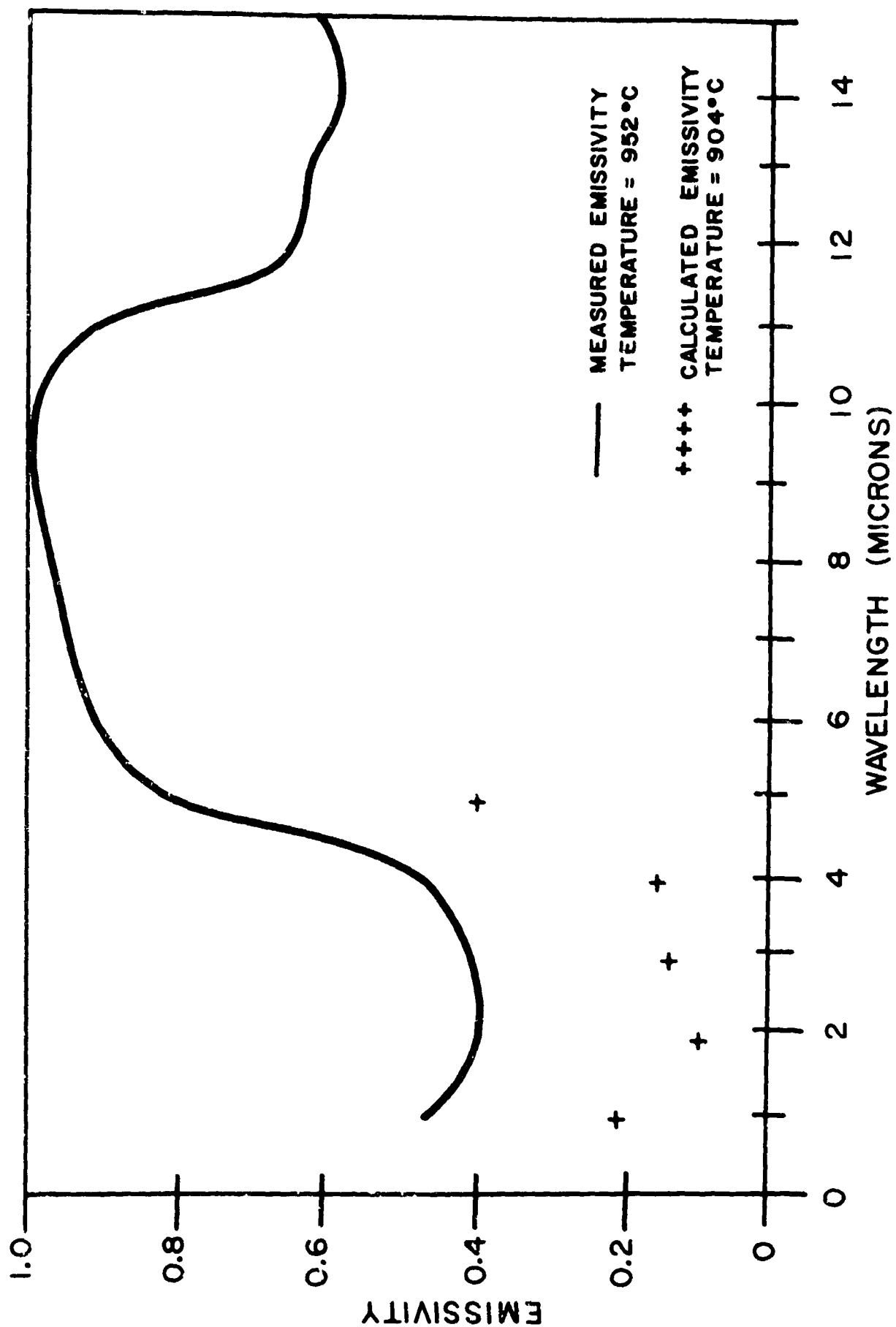


Fig. 7.35 Measured vs. Calculated Emissivity of Commercial Al_2O_3 (AV-30) 952°C .

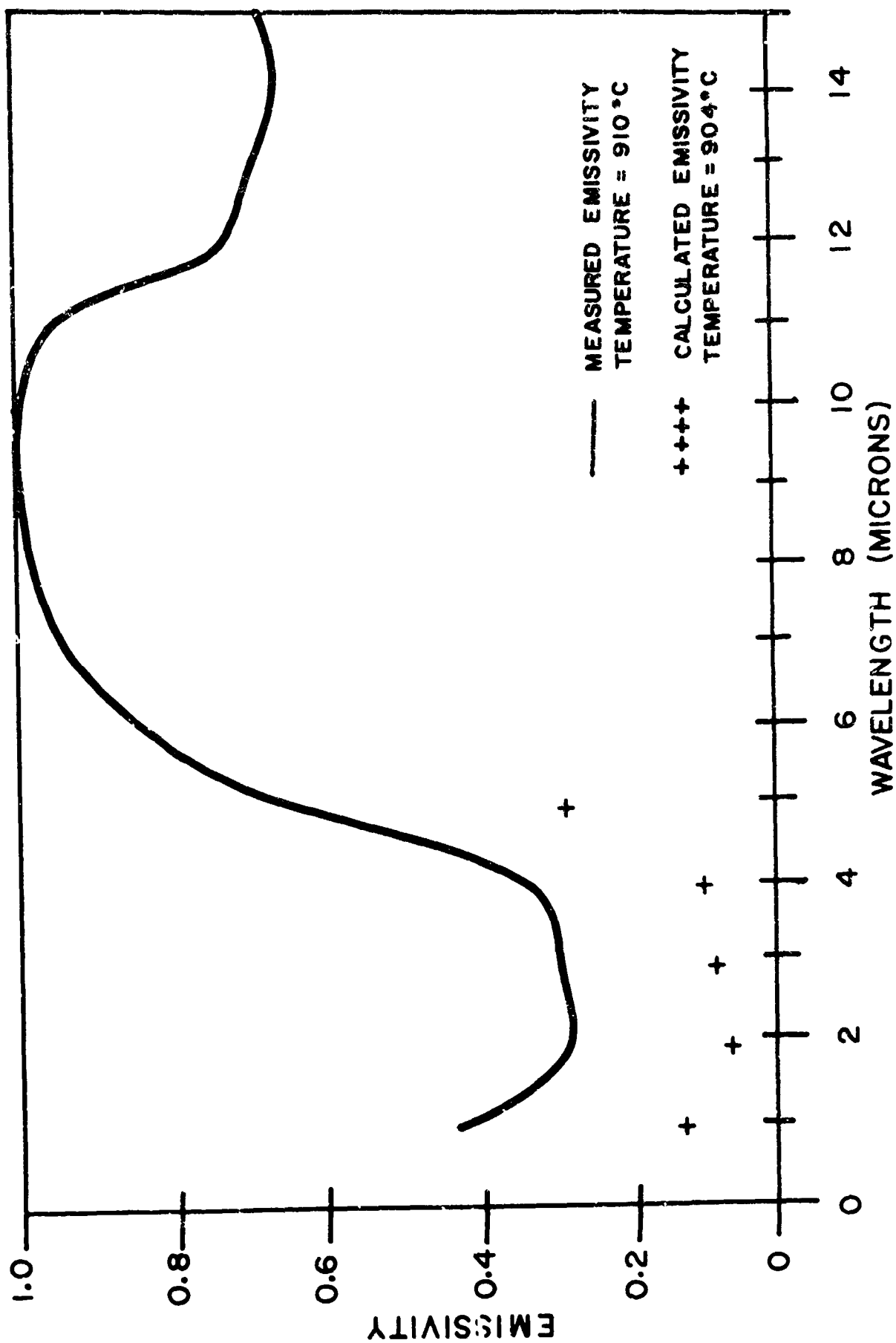


Fig. 7.36 Measured vs. Calculated Emissivity of Commercial Al_2O_3
 (AP-35) 910°C.

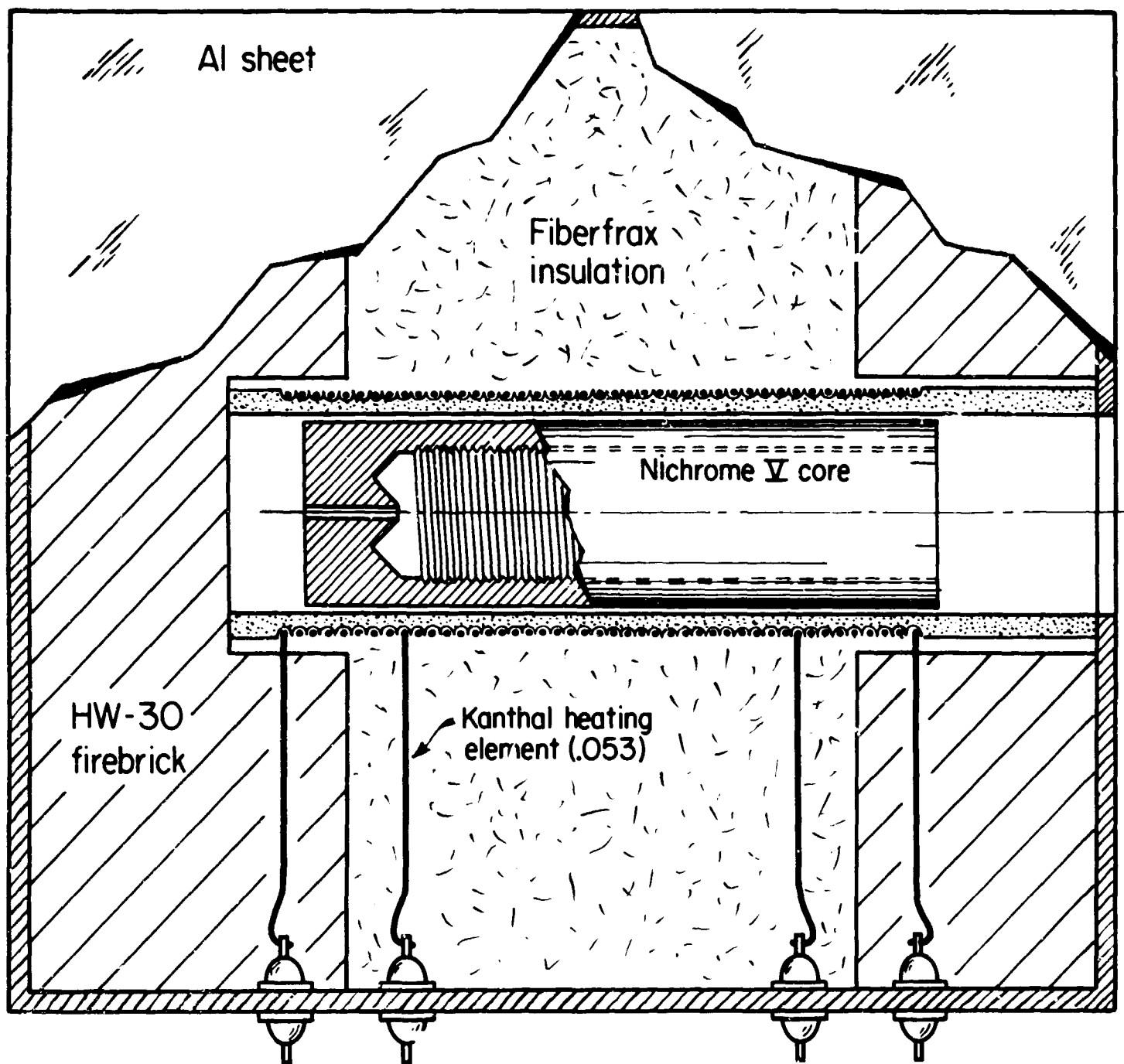


Fig. 7.37 Blackbody Furnace

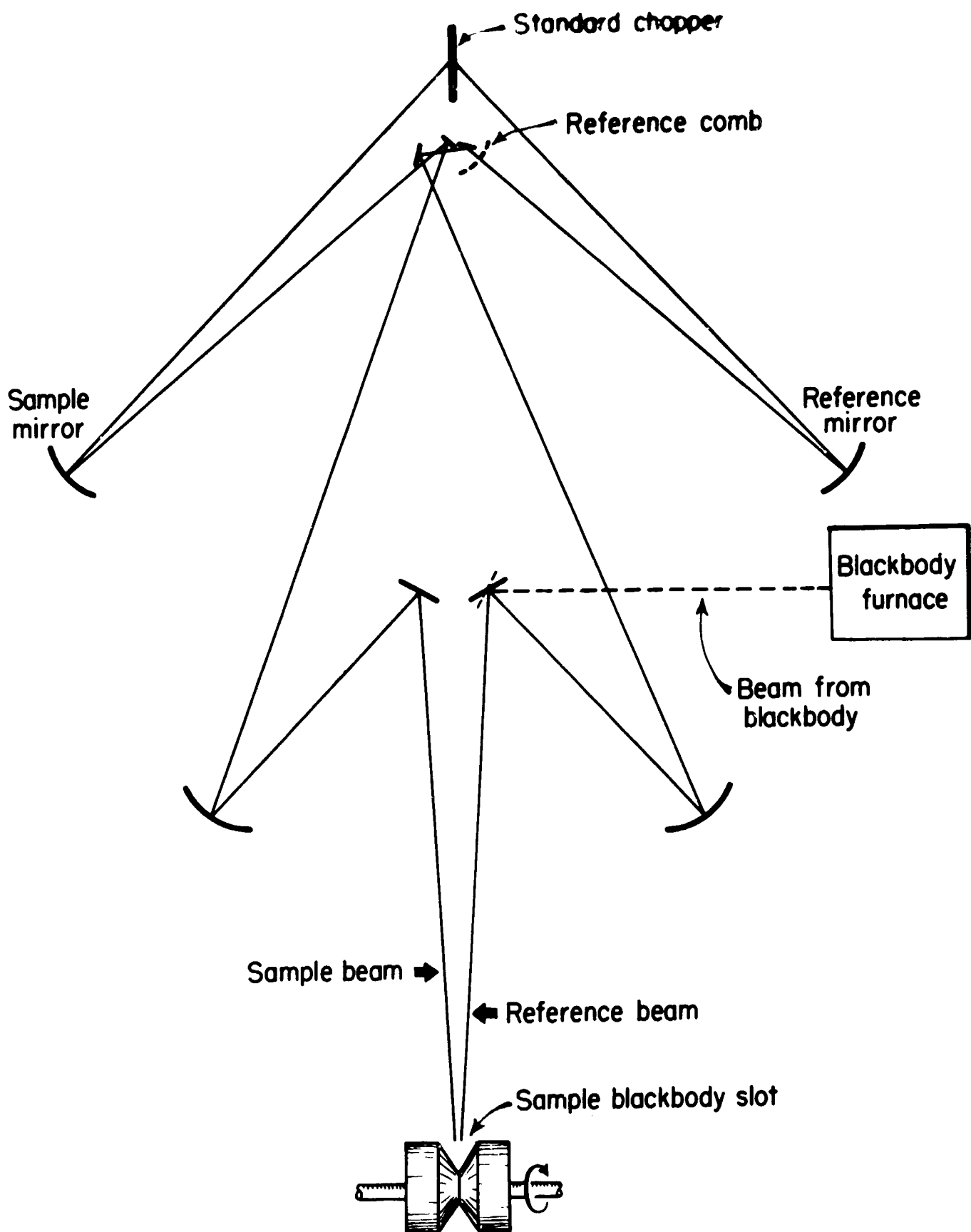


Fig. 7.38 Calibration Optical System

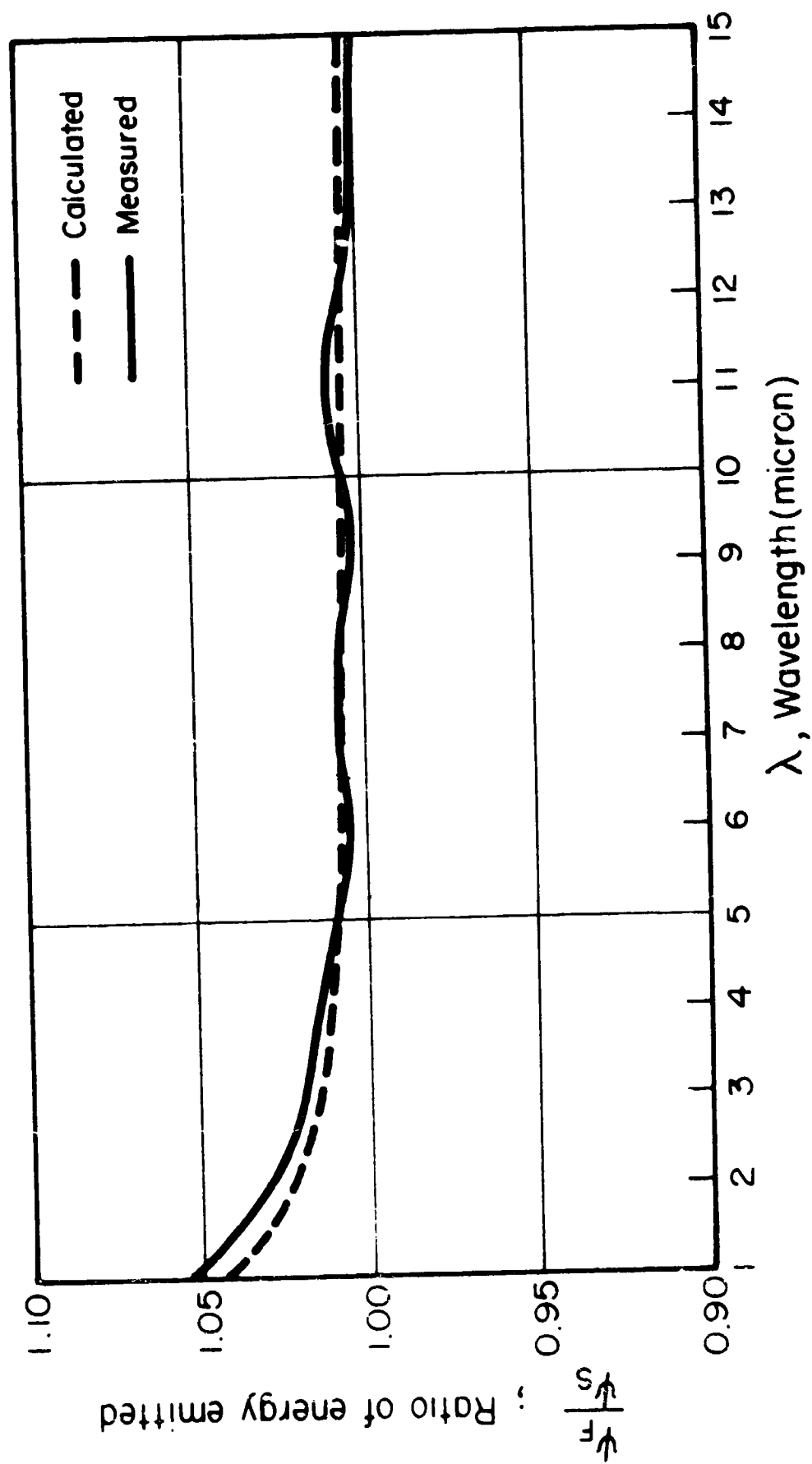


Fig. 7.39 Ratio of Energy Emitted by Blackbody Furnace to that Emitted by Rotating Slot Using Known Temperature Difference.

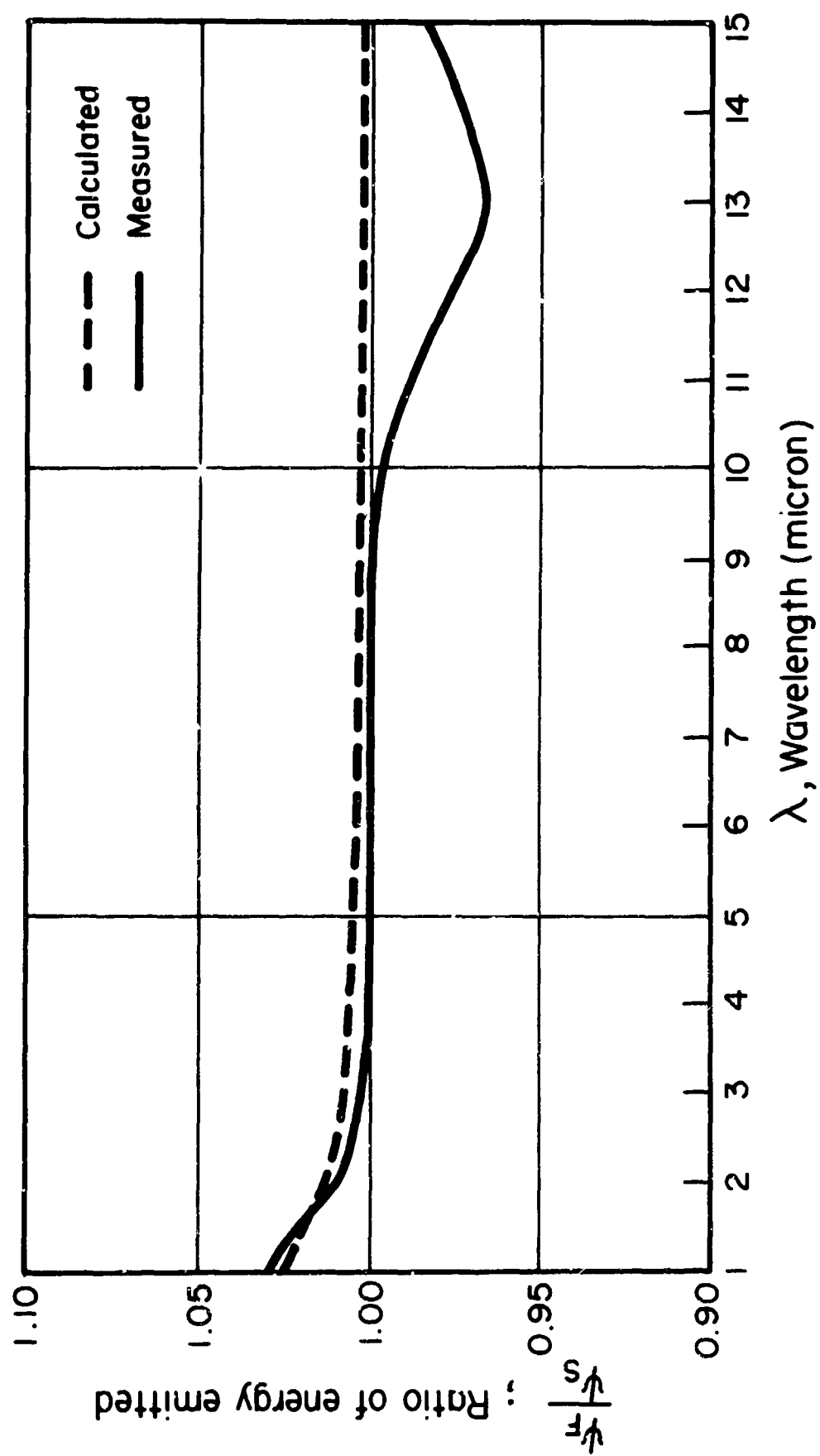


Fig. 7.40 Ratio of Energy Emitted by Blackbody Furnace to that Emitted by Rotating Slot with Slight Misalignment

8.0 COMPARISON OF MEASURED AND CALCULATED EMISSIVITIES

Directly measured values of the normal emissivity are compared with values calculated from our material characterization in Figs. 7.1 - 7.29.

8.1 Aluminum Oxide

Measured and calculated values for specially prepared high purity aluminum oxide are shown in Fig. 7.1 - 7.15. In the 2-4 micron range where absorption is low and the scattering coefficient high the emissivity is low; calculated and measured values generally agree to better than ± 0.05 . In some cases the calculated values are greater than, and in some cases less than, the measured values. Inasmuch as the sum of the precision of measurement and calculation is about ± 0.05 , we regard the agreement as good.

At wavelengths of 1 and 5 microns, where the absorption coefficient is increasing rapidly, the calculated values are in all cases slightly or significantly lower than the measured values. This results from the fact that the purity of the polycrystalline samples is less than the single crystals, and thus the absorption coefficient is less for the single crystals, giving a low value for the calculated emissivity.

In all cases the general shape of the calculated and measured curves are similar.

8.2 Silica Glass

Measured and calculated values for silica glass samples are shown in Fig. 7.16 - 7.19. As with the alumina samples, calculated and measured values are in close agreement in the 2-4 micron range. Calculated values at 1 and 5 microns are lower than measured values, and the general shape

of the emissivity wavelength curve is the same for the calculated and measured values.

3.3 Magnesia

Measured and calculated values for hot-pressed magnesium oxide samples are shown in Figs. 7.20 - 7.25. Here the influence of the absorption coefficient is particularly pronounced. The hot-pressed samples were observed to darken during testing, presumably because of carbon pick-up in the hot pressing operation (done in graphite dies). As a result, the measured emissivity is several times as large as that calculated; that is, the single crystal absorption data are completely unsuitable for the hot-pressed polycrystalline samples.

8.4 Strontium Titanate

Measured and calculated values for sintered strontium titanate are shown in Figs. 7.26 - 7.29. Sample SR-1 was sintered for a long time at high temperatures and was visually observed to darken. As a result, the measured emissivities are substantially greater than those calculated from single crystal data. Sample SR-2 (having higher porosity) was sintered for a short time, darkened less, and the measured and calculated values are in much better agreement.

Because of the tendency for the absorption coefficient of strontium titanate to change as a function of heat treatment, the emissivity will also change as a function of thermal history.

8.5 Commercial Alumina

A comparison between the measured and calculated emissivities for several samples of commercially prepared alumina are shown in Figs. 7.30 - 7.36. For the purest of

these, AD995, agreement between calculated and measured values is reasonably good. For the least pure, AD-85, measured and calculated values differ by a factor of four. This results primarily from the fact that calculated values are based on the absorption coefficient of a single crystal, while actual absorption coefficients of the impure polycrystalline samples increase with the impurity content.

9.0 APPARATUS AND METHOD FOR MEASURING NON-ISOTHERMAL EMISSION

The purpose of the apparatus herein described is to produce a controlled temperature gradient across a disc-shaped ceramic sample whose emissive properties are to be measured. The gradient is produced only in the radial direction, thereby reducing the analysis to that of a one dimensional heat transfer problem. A rotating sample arrangement is used to maintain symmetric temperature conditions.

The apparatus operates inside the furnace which has been used for isothermal emissivity measurement; the latter has been described previously. The furnace heating elements produce either a uniform temperature throughout the sample, or adjust the surface temperature. An internal resistance element is used to produce a positive gradient across the sample while a hollow shaft is used to cool the samples with forced air. The complete apparatus is shown in Figure 9.1.

The samples and the internal heating element are supported on a one-half inch alumina shaft. The alumina shaft is supported and rotated by Inconel shafts with conical points to mate with conical holes at each end of the alumina shaft. The two Inconel shafts are rotated by an electric motor and synchronized by a pair of selsyns. This arrangement assures minimum stress and vibration on the shaft and sample assembly while giving a uniform rate of rotation.

Provision has been made for cooling the interior of the sample by air. A hollow alumina shaft is used in this arrangement with compressed air forced through this shaft. This arrangement has not been tested.

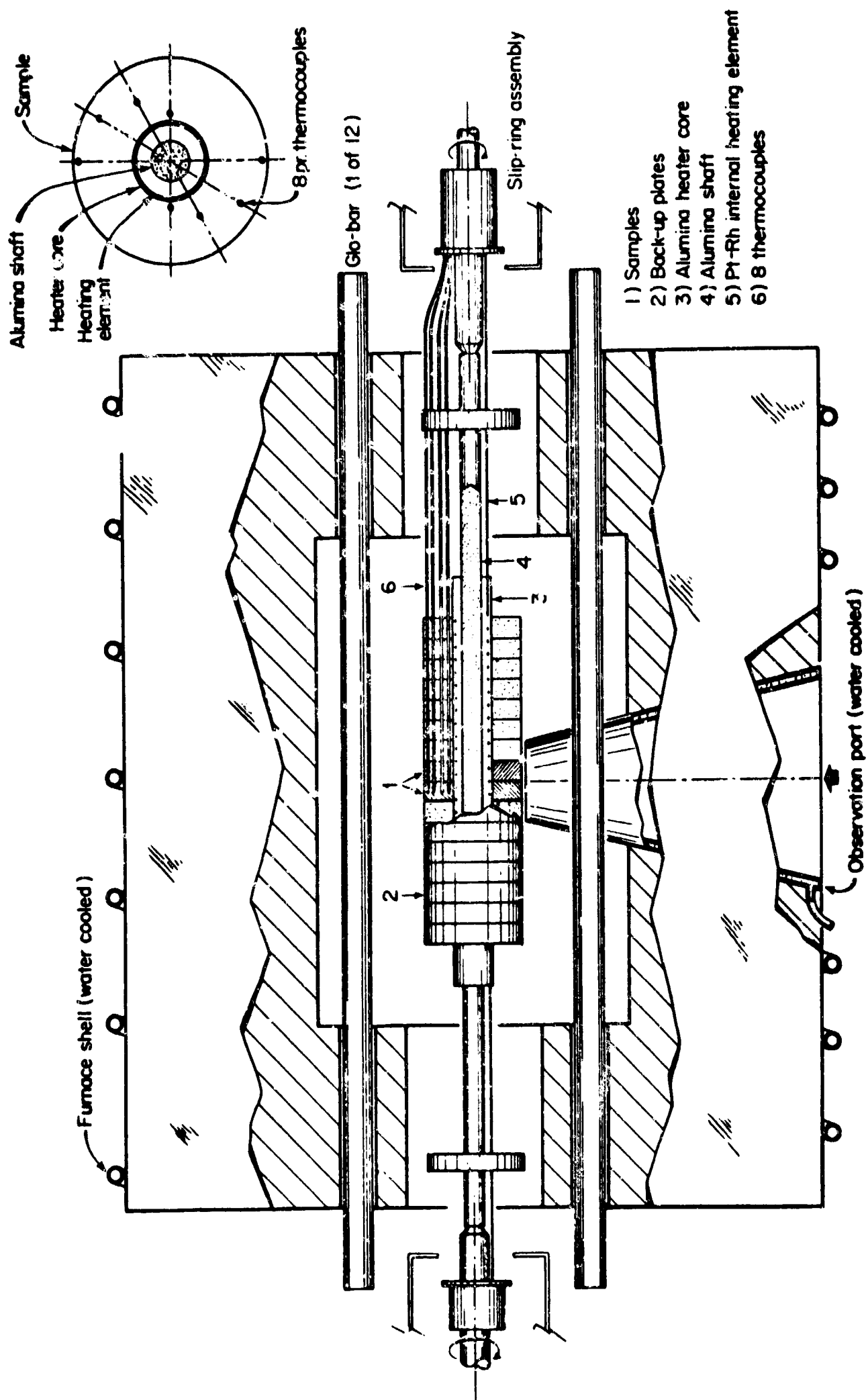


Fig. 9.1 Non-Isothermal Emissivity Apparatus

9.1 Production of Radial Thermal Gradient

In order to minimize the effects of thermal variations, the apparatus was designed to produce a radial temperature gradient in the sample. The gradient is obtained in a sample which has a width of one-half inch and which is placed between ceramic discs of the same dimensions and made of a material with similar thermal properties. The discs are held together by an axial spring load; the resulting thin air gap between adjacent discs reduces axial heat transfer and resultant temperature gradients along the samples and support plates.

The interior heating element is wound for a length of nine inches under the sample and support plates, with the samples located at the center of the winding. This arrangement gives a uniform axial heat zone in the region of the sample and support plate assembly; no axial gradient is possible since there is no variation in thermal properties in the axial direction.

9.2 Internal Heating Element

The internal heating element, producing the non-isothermal condition consists of a Pt-40% Rh alloy resistance element rotating with the samples. This wire element is spirally wound around a one-inch O.D. alumina core. The core is grooved for a ten turns per inch winding and flame sprayed with alumina to cover the resistance wire. The outer surface is ground true to facilitate assembly of the sample and support plates on the heating element. The power for this heater is supplied to the rotating element through two slip-ring assemblies located on the drive shafts at either end of the furnace.

9.3 Measurement of the Temperature Gradient

The radial temperature and temperature gradient in the disc shaped samples are measured by eight thermocouples imbedded in the samples and supported by the backup plates. These thermocouples are arranged in two groups of four to give two sets of measurements for locations 180° apart on the sample. Each set of couples is positioned on a radial spiral covering 90° of sample. This minimizes any effect the couples have on the radial heat transfer or temperature distribution in the samples. Normally two samples will be run adjacently with one set of thermocouples in each.

The thermocouple elements are Chromel-Alumel encased in an Inconel sheath. The thermocouples may be wired to indicate both absolute and relative temperatures. Signals from the thermocouples are received at one end of the furnace by a low noise slip ring assembly mounted on the exterior drive shaft. Measurement is done with a Leeds & Northrup K-3 potentiometer.

9.4 Operation

The same optics used for isothermal emissivity measurements are used in this experiment with one change. As shown in Fig. 7.38, one mirror is rotated to receive the radiation from a blackbody furnace. The latter furnace is maintained at a temperature near the surface temperature of the sample.

9.5 Non-Isothermal Measurements

Fig. 9.2 is a plot of the ratio of the emissivity of an Al_2O_3 body under isothermal conditions (radiating surface at 895°C) to the emissivity of the same body (radiating surface at 898°C) with a positive temperature gradient across

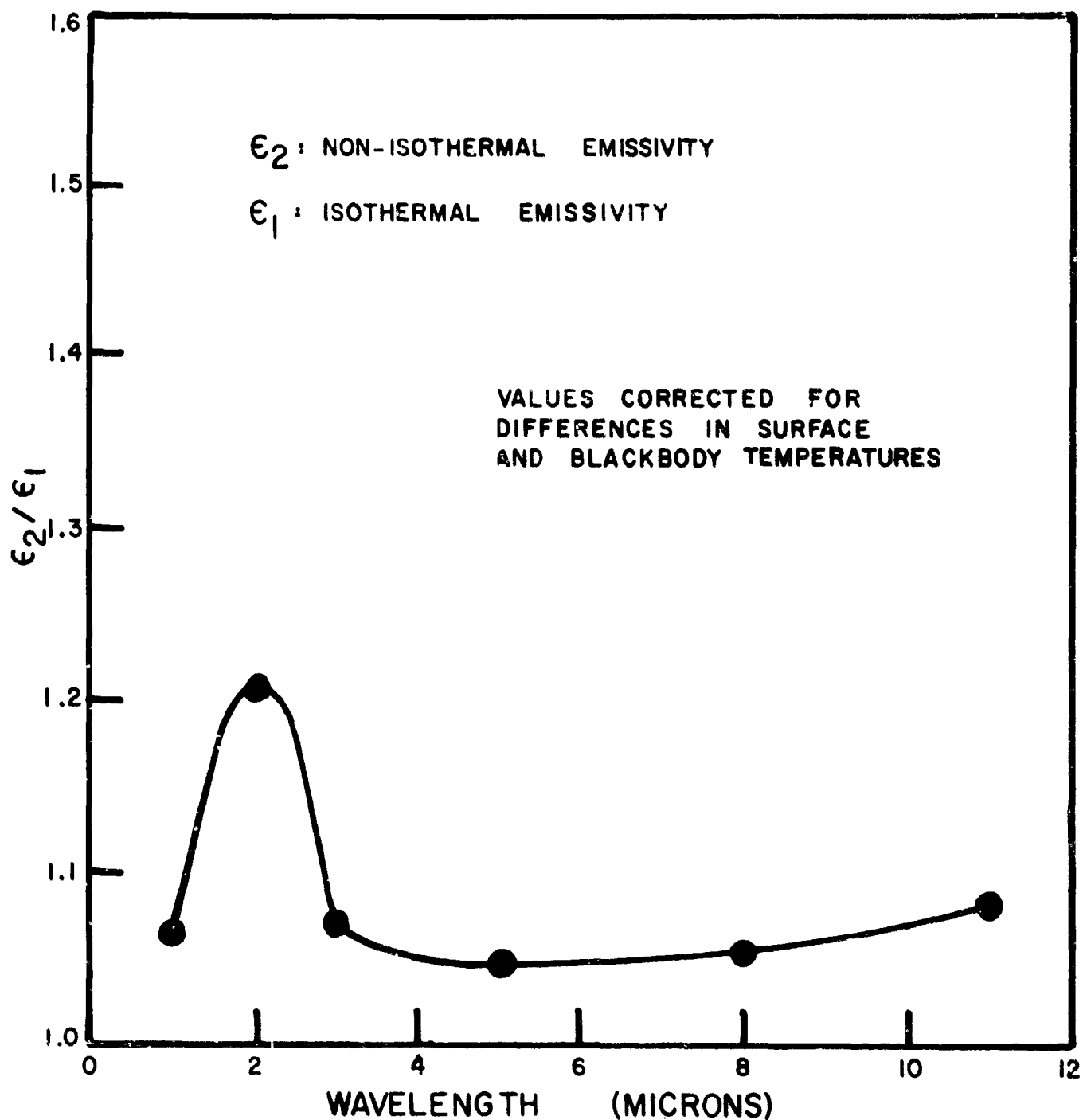


Fig. 9.2 Comparison of Isothermal and Non-Isothermal Emissivity of an Al_2O_3 Body (Western Gold and Platinum Company, Al-3-96%, SiO_2 -4%). Non-Isothermal Radiating Surface at 898°C - Thermal Gradient $60^\circ\text{C}/\text{cm}$. Isothermal Radiating Surface at 895°C .

the sample of 114°C ($60^{\circ}\text{C}/\text{cm}$). In both cases measurement of emissivity was made relative to an external blackbody at approximately the same temperature as the radiating surface. Temperature differences between blackbodies and radiating surfaces were corrected using Wien's law (Eq. 7.5).

10.0 DISCUSSION

Over the wavelength from 0.5-15 microns different processes affect the emissivity of oxide materials and as a result no single analysis is suitable for the entire range of material behavior. At wavelengths shorter than about 6 microns the absorption coefficient is sufficiently low that emissivity is a volume process and is strongly affected by the absorption coefficient and scattering coefficient of the oxide. At wavelengths above about 6 microns the oxides are essentially opaque; as a result, emissivity is a surface characteristic which is affected by the surface reflectivity (depending on the index of refraction) and surface roughness, and in general is similar to metals and other opaque solids as far as the material characteristics which need to be defined. Because the reflectivity is low, the emissivity is high in the range up to about 11 microns. At higher wavelengths, as the reststrahl frequency is approached, the absorption coefficient remains high, but the reflectivity increases and as a result, the emissivity drops off.

Under conditions where oxides are opaque, that is at wavelengths greater than 6 microns or so, the process is not significantly different than for other opaque solids and does not offer significantly new problems. At wavelengths shorter than about 6 microns, the process is quite dissimilar from that in most materials which have been studied previously, and as a result, it is in this wavelength range that we have concentrated our efforts.

In the region where a high absorption coefficient does not overwhelm the volume process, the emissivity depends on the reflectivity of the surface (a function of the index of refraction)

and on the material constant $\beta_0 = \sqrt{a/(a+2s)}$. Thus, in order to estimate the emissivity, it is necessary to calculate the values of the absorption coefficient and scattering coefficient. Values of the absorption coefficient have been determined from transmissivity measurements with single crystals. Values for the scattering coefficient have been calculated on the basis of pore size, relative index of refraction, wavelength and pore concentration. The precision of this calculation (which requires knowledge of the back scattering coefficient as well as total scattering) is not high, but since it enters as a square root relationship in the determination of emissivity, the precision of the final emissivity calculation is better than that for the estimation of the scattering coefficient.

A comparison of the calculated and measured values of emissivity at 2-4 microns shows good agreement for specially prepared high-purity aluminum oxide (within ± 0.05 emissivity units). This result is regarded as satisfactory considering that it is determined entirely from material characteristics such as microstructure and pore concentration and is independent of actual optical property measurements. It indicates the strong influence of porosity on fixing the emissivity - the emissivity decreases linearly with increasing porosity. It also, by comparison with other samples of alumina, particularly impure commercial materials, shows the great influence of small changes in composition and microstructure on the resulting emissivity. At a wavelength of 3 microns impure commercial aluminas have emissivity values as large as 0.5, while the high-purity and small pore size samples specially prepared for this study have values as low as 0.03.

That is, for a material such as "alumina" an order of magnitude difference in the emissivity can result from control of microstructure and composition.

A comparison of the calculated and measured values for MgO and strontium titanate indicates the strong influence of the absorption coefficient on experimental results. The MgO samples tested were darkened, presumably resulting from carbon pick-up during hot pressing in graphite dies, and as a result had values of emissivity at 3 microns as high as 0.8 compared with calculated values of the order of 0.1, which would apply to the pure material without contamination. Thus, in the preparation of low emissivity materials, contamination is of significant importance. For strontium titanate heat treatment affects the absorption coefficient (presumably as a result of changed oxidation states). Thus, measurements of the emissivity of strontium titanate and similar materials are subject to change with changing environment, and one must specify carefully the conditions of preparation and testing in order to report useful material data. This characteristic further limits the utility of tabulated emissivity values for oxide materials independent of detailed sample description.

In general then, in the important 1-5 micron range corresponding to the range of maximum energy emission over temperatures from 1000-2500°C the emissivity of oxide materials can vary, or be varied, over a wide range. For low emissivity, high purity, high porosity, and small pore size is preferred; under such conditions the emissivity can be well below 0.1. For high emissivity, the main requirement is to increase the absorption which can be done by the introduction of impurities or contaminants which give rise to absorption in this wavelength range. For materials such as this, emissivities of

the order of 0.8-0.9 can be achieved. This wide range in values found for oxides and a quantitative evaluation of the means necessary for control of the emissivity is an important consideration in any application of these materials at high temperatures involving heat transfer considerations.

In the measurement of isothermal emissivity we have compared our blackbody slot system (in which the sample itself corresponds to the reference standard) with an external blackbody designed to have an emissivity greater than 0.995. Experimentally the results with an external blackbody and one machined into the sample were indistinguishable. The greater ease in maintaining temperature uniformity when the blackbody slot is actually part of a sample makes it a preferable system for experimental observation.

In the calculation of emissivity, it is necessary to know the back scattering coefficient for diffuse radiation and also the absorption coefficient for diffuse radiation. As a result, we have analyzed the absorption coefficient for diffuse radiation relative to the value measured for plane parallel radiation, and also evaluated the scattering coefficient - particularly for systems in which pores are the main scattering centers and the index of refraction of the pore is smaller than that of the solid matrix material. Under these conditions the back scattering coefficient can be evaluated with sufficient precision to make a useful estimate of the resulting emissivity.

One aspect of the problem has been that we calculate hemispherical emissivity while our measurements have been for normal emissivity. After an analysis of the transfer of radiation through the boundary of the sample, we have

evaluated the ratio of normal and hemispherical emissivity and find that it depends on the relative index of refraction but is not far from unity for most of the oxide materials of interest.

Application of this data to non-isothermal systems involves use of the Hamaker approximation which essentially linearizes the temperature gradient in order to obtain a group of differential equations for which an analytical solution is available. Using numerical techniques, we have compared the Hamaker and exact equations for a series of conditions for temperature up to 3000°C , for scattering coefficients up to 100 cm^{-1} , and for temperature gradients up to 1000°C/cm . For these conditions we find that the Hamaker equation is in satisfactory agreement with the exact equation except when values of the lattice conduction are much greater than for radiant energy transfer. For all practical applications of oxide materials at temperatures above 1000°C , the Hamaker equation gives a satisfactory approximation to the exact equation; in fact, for values of the absorption and scattering coefficient greater than unity it is within 1/10 of one per cent of the exact equation for all the conditions that we have evaluated.

One advantage of the Hamaker equation over the exact solution is that it is not necessary to specify all of the boundary conditions at one surface, and we have extended the Hamaker equation to some additional boundary conditions which are of greater utility than specifying all the boundary conditions at one point in the system.

The application of the Hamaker equation of most interest is to conditions of non-isothermal emissivity. In this case, the effective emissivity depends on temperature gradients

within the body as well as on the surface temperature itself. We have designed and tested an apparatus which allows us to measure the energy emitted from a surface of a sample containing a known temperature gradient in comparison with that of a blackbody standard. Test measurements indicate the energy emitted from aluminum oxide ceramics does strongly depend on the temperature gradient as well as on the surface temperature. With a temperature gradient of $60^{\circ}\text{C}/\text{cm}$ the effective emissivity for the same surface temperature is experimentally found to increase about 22% at 1000°C . In subsequent work we plan to carry out additional experimental measurements and compare these directly with calculations based on sample characteristics. As for the case of isothermal emissivity it is essential to have a detailed sample characterization to make useful analyses and predictions.

11.0 REFERENCES

1. J. W. Ryde, "Scattering of Light by Turbid Media: I,"
Proc. Roy. Soc., Ser. A131, 451-465 (1931).
2. H. C. Hamaker, "Radiation and Heat Conduction in Light
Scattering Materials," Philips Res. Reports Vol. 2
(1947).
3. R. C. Folweiler, A.S.D. Tech. Documentary Report No.
ASD-TDR-62-719.
4. Ryde and Cooper, "Scattering of Light by Turbid Media: II,"
Proc. Roy. Soc., Ser. A131 (1931).
5. S. Chandrasekhar, RADIATIVE TRANSFER, Oxford, O.U.P. (1950).
6. H. C. van de Hulst, Astrophys. J., 107, 220 (1948).
7. H. C. van de Hulst, LIGHT SCATTERING BY SMALL PARTICLES,
John Wiley & Sons, New York (1957).
8. R. H. Boll, R. D. Gumprecht and C. M. Sliepcevich,
J. Opt. Soc. Amer., 44, 18 (1954).
9. D. W. Lee and W. D. Kingery, Jour. Amer. Ceram Soc., 43,
594 (1960).
10. Walsh, D.S.I.R. Illumination Research Tech. Papers 2, 10,
(1926).
11. W. N. Harrison, et al., "Standardization of Thermal
Emittance Measurements," WADC TR 59-510, Part IV,
Dec. 1962.

APPENDIX I

VALUES FOR INDICES OF REFRACTION USED IN EMISSIVITY CALCULATIONS*

$$n_{\lambda} \text{ at } \lambda \text{ (u)} =$$

MATERIAL	0.5 μ	1	2	3	4	5	8	11
Al ₂ O ₃	1.78	1.75	1.74	1.72	1.65	1.60	(1.33)	
SrTiO ₃	2.48	2.31	2.27	2.23	2.18	2.11	(1.85)	
9606	1.45	1.45	1.43	1.41	(1.35)	(1.30)		
9608	1.45	1.45	1.43	1.41	(1.35)	(1.30)		
MgO	1.75	1.72	1.70	1.68	1.65	1.55	(1.45)	
CaF ₂	1.43	1.42	1.41	1.41	1.40	1.39	1.35	1.28
SiO ₂	1.45	1.45	1.43	1.41	(1.35)	(1.30)		

Parentheses indicate extrapolated values.

* from Wolfe and Ballard, Proc. Inst. Radio Engineers 47, 1540 (1959)

APPENDIX II

SAMPLE CALCULATION OF EMISSIVITY

II.1 Calculation of α and a for Al-6 (3μ) at 904°C

The calculation of emissivity for Al-6 (3μ) at 904°C is typical of the method used for obtaining all values of calculated emissivity. From the microstructure of Al-6 in Fig. 5.5 values of P (pore volume fraction) and r (average pore radius) are obtained.

The absorption coefficient for single crystal Al_2O_3 was calculated from the ratio of energy transmitted through an optically polished section 0.313 cm thick to that incident upon it and corrected for the surface reflectance at the polished surface from the following relationship:

$$\frac{I}{I_0} = (1 - \rho)^2 e^{-\alpha t} \quad (\text{II.1})$$

where:

I = transmitted energy

I_0 = incident energy

α = absorption coefficient

t = thickness of section in cm.

The value of surface reflection is calculated from the index of refraction:

$$\rho = \frac{(1 - n_\lambda)^2}{(1 + n_\lambda)^2} \quad (\text{II.2})$$

The value of the absorption coefficient α may then be determined by solving Eq. (II.1)

$$\alpha = - \frac{\ln \left[\frac{I}{I_0} \times \frac{1}{(1 - \rho)^2} \right]}{t} \quad (\text{II.3})$$

For Al_2O_3 at (3μ) and 904°C

$$\frac{I}{I_o} = .81$$

$$\frac{1}{(1-\rho)^2} = 1.155 \text{ (at } \lambda = 3 \mu, n = 1.72)$$

$$t = .313 \text{ cm.}$$

When II.3 is evaluated for the stated conditions

$$\alpha = .215 \text{ cm}^{-1}$$

Equation 2.16 states:

$$a = 2 \alpha \quad (2.16)$$

Where a is the absorption coefficient for a polycrystalline material with pores as scattering centers, therefore:

$$a = .430 \text{ cm}^{-1}$$

II.2 Calculation of s for Al_2O_3 (3μ) at 904°C

The scattering factor s is defined by the expression:

$$s = \frac{3}{4} K \frac{P}{r} \quad (2.44)$$

P = pore volume fraction

r = average pore radius

K = scattering factor from Fig. 2.3

$$p = \frac{4\pi r |m-1|}{\lambda m} \quad (\text{II.4})$$

where:

r = average pore radius (1.68μ)

$$m = \frac{1}{n_\lambda}$$

For Al-6 (3μ) at 904°C , $P = 0.23$ and $K = 1.70$

From 2.44 then

$$s = 1.751 \times 10^3 \text{ cm}^{-1}$$

II.3 Evaluation of β_0 from values of a and s for Al-6 (3μ) at 904°C

$$\beta_0 = + \sqrt{\frac{a}{a + 2s}} \quad (\text{II.5})$$

where:

a is the absorption coefficient for polycrystalline materials with pores as scattering centers. ($.430 \text{ cm}^{-1}$)

s is the scattering coefficient ($1.751 \times 10^3 \text{ cm}^{-1}$)

β is a material constant

$$\beta_0 = + \sqrt{\frac{4.30 \times 10^{-1} \text{ cm}^{-1}}{4.30 \times 10^{-1} \text{ cm}^{-1} + 3.502 \times 10^3 \text{ cm}^{-1}}}$$

$$\beta_0 = + \sqrt{1.23 \times 10^{-4}}$$

$$\beta_0 = 1.11 \times 10^{-2}$$

II.4 Calculations of the reflectivity, ρ and the emissivity, ϵ from values of β_0 , ρ_0 and ρ_i

Values of ρ_0 and ρ_i are found in Table 2.1 for a range of refractive indices. Values between were interpolated.

The value of ϵ is derived from equation 2.1.

$$\rho = \frac{(1-\rho_i)^2 - \beta_0^2 (1 - \rho_i - 2\rho_0) (1 + \rho_i) + 2\beta_0 (\rho_0 + \rho_i) (1 - \rho_i)}{(1 - \rho_i)^2 + \beta_0^2 (1 + \rho_i)^2 + 2\beta_0 (1 - \rho_i)^2}$$

where:

β_0 is a material constant

ρ_0 is the reflectivity of diffuse energy incident on the sample

ρ_i is the reflectivity of diffuse energy emerging from the sample.

The following terms are evaluated numerically:

$$\begin{aligned} \rho_0 &= .122^4 & (1 - \rho_i)^2 &= .506 \\ \rho_i &= .703 & \rho &= .938 \\ \beta_0 &= 1.11 \times 10^{-2} & 2\beta_0 &= 2.22 \times 10^{-2} \\ (1 - \rho_i) &= .297 & \beta_0^2 &= 1.23 \times 10^{-4} \\ (1 - \rho_i)^2 &= 0.0882 & (\rho_0 + \rho_i) &= .825 \\ & & (1 - \rho_i - 2\rho_0) &= .053 \end{aligned}$$

Substituting in 2.1, we find:

$$\begin{aligned} \rho &= 0.938 \text{ and} \\ (1 - \rho) &= \epsilon \\ \epsilon &= .062 \end{aligned}$$